Solar combisystem with Thermo-Differential Valve
Experimental and Numerical Research

van Duijnhoven, M.A.

Award date:
2018

Technische Universiteit
Eindhoven
University of Technology

Solar combisystem with Thermo-Differential Valve

Experimental and Numerical Research

Master Thesis

M.A. van Duijnhoven
Eindhoven University of Technology
15 August 2018

Solar combisystem with Thermo-Differential Valve

Experimental and Numerical Research

Master Thesis

Author	M.A. van Duijnhoven 0715511 m.a.v.duijnhoven@student.tue.nl
Educational Institution	Eindhoven University of Technology
Master Program	Sustainable Energy Technology
Department	Mechanical Engineering
Research Group	Energy Technology
Thesis Supervisor	Dr. Ir. C.C.M. Rindt
Company	Conico Valves bv
External Supervisor	Ir. N. van Ruth

Academic Year	2017 / 2018
Report Date	15 August 2018

Technische Universiteit
Eindhoven
University of Technology

Declaration concerning the TU/e Code of Scientific Conduct for the Master's thesis

I have read the TU/e Code of Scientific Conduct[i].

I hereby declare that my Master's thesis has been carried out in accordance with the rules of the TU/e Code of Scientific Conduct

Date

15-8-2018

Name

M.A. van Duijnhoven

ID-number

071551

Signature

Submit the signed declaration to the student administration of your department.

[i] See: http://www.tue.nl/en/university/about-the-university/integrity/scientific-integrity/
The Netherlands Code of Conduct for Academic Practice of the VSNU can be found here also.
More information about scientific integrity is published on the websites of TU/e and VSNU

Acknowledgements

This report is the result of the master thesis " Solar Combisystem with Thermo-Differential Valve: Experimental and Numerical Research". The master thesis is part of the master program Sustainable Energy Technology (SET) at Eindhoven University of Technology. The goal of this thesis was to experimentally determine the influence of a start stop and continuous operation on the thermal efficiency of an evacuated tube solar collector, and to investigate whether the simulation software TRNYS18 was able to simulate the CV-system.

Due to my personal interest in renewable energy sources, I started the master program SET. As this thesis has a connection to developing and improving a renewable energy source, it suits both my interests and my education. Moreover, this thesis allowed me to increase my numerical competences, which was improved by using TRNSYS18, and to follow my passion for conducting experimental research.

During my graduation I was supervised by Dr. Ir. C.C.M. Rindt, who I like to thank for the supervision during the master thesis and for helping me to improve my numerical competence. I also would like to thank Ir. N. van Ruth from the company Conico Valves bv, not only for developing this research topic but also for the advice during the analysis of the experimental data. Furthermore, I would like to thank the help provided by M.J. Huijzer to finetune the measuring equipment and how to operate the solar simulator, and especially thank J.M. Hullu for the help with creating the improved experimental setup and mental support. Finally, I would like to thank L. Heuff for evaluating the report and M. Eland for also evaluating the report and support during the thesis.

Beek en Donk, 15 August 2018

Myron van Duijnhoven

Abstract

In 2010, the European Union developed renewable energy targets for the year 2020 because of global warming and the deficiency of fossil fuel. One of these targets states that the contribution of renewable energy sources should be at least 20 percent on the total EU energy consumption. One of the methods used in Germany to increase this contribution, is using solar radiation to generate useful heat by means of a solar combisystem. However, implementing a solar combisystem in Germany is challenging due to cold periods, such as the winter period, through which the fluid inside the solar collector might freeze thereby damaging the system. The main solutions that are being implemented in Germany to prevent his problem have high investment costs and/or are susceptible for failures. For this reason, the company Conico Valves bv developed a solar combisystem that uses a novel and patented valve called the Thermo-Differential Valve (TDV). This valve allows the solar combisystem to operate with a continuous flow in cases where other solar combisystems use a start stop operation (periodically allowing the pump to circulate); however, it was unknown whether there is a difference between these two operations modes. Additionally, because research on the thermal performance of the CV-system will be conducted by engineers of ITW using the simulation software TRNSYS, research had to be conducted whether the CV-system could be simulated with this software. Both of these problems were analyzed in this master thesis by conducting an experimental research on the thermal performance of an ETSC and a numerical research on simulating the CV-system in TRNSYS18.

The first part of the experimental research consisted of improving the setup created by [Balkom, 2015], which was designed for measuring the thermal performance of PVT-panels, because there were several issues in the setup; for example, too low volume flowrates and an inconsistent pump. A literature research was conducted to obtain the design requirements for improving the setup, which was used to create a new thermal circuit in the test setup. This thermal circuit consists of a cooling cycle, which absorbs the solar heat that is generated in the solar collector due to radiation of a solar simulator, and a solar collector loop, which generates a constant volume flow, incorporates the measuring equipment and integrates the design requirements. Measurements were used to analyze the temperatures and volume flowrate in the setup, in order to verify that experiments could be performed according to the NEN-EN-ISO 9806 norm for solar thermal testing.

During the second part of the experimental research, a theoretical model of an evacuated tube solar collector (ETSC) was developed for investigating the parameters that could influence the thermal performance, in which it was found that mainly the volume flowrate has a high influence. Before the two operations modes could be investigated, experiments were executed on the thermal performance of the inlet temperature using a constant solar radiation and volume flowrate. The results from this study were used to acquire the linear and quadratic heat loss coefficient of the ETSC that can be used to determine the optical efficiency; the optical efficiency is used to compare the performance of an ETSC under influence of different parameters. While using these coefficients, the optical efficiencies during different volume flowrates and start stop operation were determined using experimental data and it was concluded that it seems to be more beneficial to use a continuous operation mode than a start stop operation. Though, as the mean temperature over the ETSC changes during the start stop operation, the loss coefficients might change, which influences the optical efficiency of the ETSC.

For the numerical research, the CV-system was decomposed into its components: the ETSC, piping, a pump, the TDV, and a thermal storage tank. The approriate TRNSYS components were found for each of these components, as TRNSYS uses individual component models, such as pumps and solar collectors, for simulating the dynamic behavior of a system. However, the TDV is a novel concept, thus there was no model available in TRNSYS, as a result four simple TRNSYS models were used to simulate the TDV. During the analysis it was concluded that both the ETSC and piping simulation models were not able to accurately simulate a start stop operation, however, they could simulate the continuous operation. Unfortunately, as an extensive research was conducted on finding an appropriate simulation model in the standard library and TESS library of TRNSYS, it means that either a new component has to be created or research is needed to find a more suitable model (outside these libraries).

These system components were further used in the numerical research, despite of their inaccuracies, to investigate if TRNSYS is capable of recreating similar temperature profiles that were found in a measurement performed by Conico Valves bv. Additionally, several parameters were unknown in the measurement, such as solar radiation and solar path. Therefore, it was impossible to recreate the measurement data in TRNSYS and instead the shape of the temperature profiles were used to analyze both the continuous and start stop operation in TRNSYS. From this research it was concluded that in both cases TRNSYS was able to accurately simulate the shape of the temperature profiles in the CV-system. Though, it was found that the accuracy of the simulation is highly dependent on the design parameters, for instance the location and length of the piping, and the simulation parameters, such as simulation time step and node configurations.

Table of Content

Nomenclature

Abbreviations	Full Meaning
CV	Conico Valves
DAQ	Data Aquisition
DHW	Domestic Hot Water
ETSC	Evacuated Tube Solar Collector
EU	European Union
IAM	Incidence Angle Modifier
LCOH	Levelized Cost of Heating
PVT	Photovoltaic Thermal
RE	Renewable Energy
TDV	Thermo-Differential Valve

Symbol	Description	Unit
A	Surface	m^2
a_1	Linear loss coefficient	$W\ m^{-2}\ K^{-1}$
a_2	Quadratic loss coefficient	$W\ m^{-2}\ K^{-2}$
B	Magnetic field	T
C	Capacitance of the collector	$kJ\ K^{-1}$
c_p	Thermal heat capacity	$J\ kg^{-1}\ K^{-1}$
D	Diameter	m
E	Energy	J
e	Roughness	µm
F’	Collector fin efficiency	-
f	Friction factor	-
h	Convective heat transfer coefficient	$W\ m^{-2}\ K^{-1}$
I	Irradiation	$W\ m^{-2}$
IAM	Incidence angle modifier	-
k	Conductive heat transfer coefficient	$W\ m^{-1}\ K^{-1}$
L	Length	m
M	Mass	kg
$\dot{m}$	Mass flowrate	$kg\ hr^{-1}$
p	Pressure	bar

Symbol	Description	Unit
Q	Heat	W
R	Thermal resistance	$K\ W^{-1}$
r	Radius	m
S	Solar radiation absorbed by the collector	W
T	Temperature	°C or K
t	Time	s
UA	Overall energy loss rate	$W\ K^{-1}$
U	Voltage	V
V	Volume	m^3
$\dot{v}$	Volume flowrate	$L\ min^{-1}$
v	Velocity	$m\ s^{-1}$
Z	Total error	-
z	Random error	-
α	Absorption coefficient / thermal diffusivity	- / $m^2\ s^{-1}$
ΔT_{LM}	Logarithmic mean temperature difference	-
γ	Control signal	-
η	Efficiency	-
η_0	Optical efficiency	-
κ	Correction factor	-
μ	Systematic error / dynamic viscosity	- / $kg\ m^{-1}s^{-1}$
ρ	Reflection coefficient / Density	- / $kg\ m^{-3}$
σ	Standard deviation	-
τ	Transmission coefficient	-
Fo	Fourier Number	-
Nu	Nusselt number	-
Pr	Prandtl number	-
Re	Reynolds number	-

Index	Description
a	Ambient / environment
abs	Absorber
avg	Average
bot	Bottom
bp	Bypass
C	Cold
cal	Calibrator
col	Collector
comb	Combined
con	Conduction
cond	Condenser
conv	Convection
edg	Edge
eva	Evaporator
fl	Fluid
g	Glass
H	Hot
ins	Insulation
i	Inner / inlet
ins	Insulation
man	Manifold
o	Outer / outlet
p	Pipe
st	Storage tank
sto	Stored
stag	Stagnation
TC	Thermocouple
tot	Total
vf	Volume flow

1| Introduction

Global warming and the increase in scarcity of fossil fuels have led to the development of renewable energy (RE) targets for the year 2020 by the European Union (EU) in 2010 [European Commission, 2017]. One of these targets states that at least 20 percent of the EU energy consumption must originate from RE sources, such as wind energy and solar energy. An increase in RE production results in a decrease in dependence on fossil fuels, creating a sustainable society. Each EU country has established its own national goal to achieve the target defined by the EU; for example, Germany defined a goal of 18 percent. To reach this goal, Germany is focusing on a strategy to increase the implementation and development of RE production technologies. Its contribution of RE sources in the total energy consumption increased from 2 percent in 1990 to 10 percent in 2009, showing that this is an effective strategy [Becker & Theis, 2016].

Germany is using solar irradiation to generate useful heat as a technology to increase its RE production. This heat can be used for space heating, domestic hot water (DHW), or both by means of a solar combisystem. Implementation of a solar combisystem in Germany is challenging, due to the fact that there is a limited amount of solar irradiation. During cold periods, such as the winter period, the ambient temperature occasionally drops below freezing point and the collector could be covered with snow. These scenarios can cause the fluid inside the solar collector to freeze, thereby damaging the system. There are two solutions being implemented in Germany to prevent this problem.

The first solution is using a different fluid that does not freeze under these circumstances. In this scenario the fluid in the solar collector differs from the fluid in the storage tank, which is used for space heating and DHW. Therefore, a heat exchanger is needed to transfer the heat generated in the solar collector to the storage tank; this solution is called an indirect solar combisystem. A drawback of this system is that the investment cost increases as does the number of components. Additionally, the overall efficiency drops in comparison with using water, which means that the price per kW generated heat increases.

The second solution uses a complex pump control strategy that prevents freezing of the fluid. This solution requires extra components to determine the system behavior; for instance, temperature sensors to observe temperature development throughout the system. Nevertheless, this strategy is not only difficult to implement, it also will increase the investment cost significantly. This type of solution uses the same fluid in the solar collector and the storage tank; hence it is called a direct solar combisystem.

Both solutions increase the investment cost of the solar combisystem and therefore the International Energy Agency has created a task called Task54. The goal of this task is to reduce the investment cost of an installed solar thermal system for end-users [IEA, 2015]. Consequently, the company Conico Valves (CV) developed a solar combisystem that uses a novel and patented valve [Conico Valves bv, 2017]; this system is called the CV system. The valve in this system is based on a unique self-actuating principle that uses the temperature difference between the storage tank and solar collector for determining the desired direction of the fluid; this valve is also called the Thermo-Differential Valve (TDV). The CV system uses two temperature sensors, which are integrated in the pumping station, thus increasing the reliability and decreases the cost significantly (less components required) in comparison to the solutions discussed in this paragraph.

1.1 Literature Review

This literature review briefly discusses three different topics: the reference model from TASK54 and overviews of the TDV as well as the CV-system with their working principle.

Reference Model

TASK54 developed a reference (indirect) solar combisystem that is situated in Würzburg Germany; Figure 1.1 presents the layout of the solar combisystem [Bachmann,2017]. This system uses six flat plate solar collectors in parallel that are connected with a heat exchanger to a storage tank with a volume of 800 L. The solar collector flow loop uses a pump with an electric consumption of 48.4 – 57.4 kWh. Furthermore, a gas condensing boiler is used for auxiliary heating if solar energy is insufficient for meeting the energy consumption of the inhabitants. This solar combisystem was modelled using the simulation software TRNSYS, by engineers from ITW University of Stuttgart, for determining the (reduced) fuel consumption and the required electric energy. To determine the levelized cost of heating (LCOH), this data was combined with the information regarding the investment cost, installation cost, as well as fuel and electricity costs. The LCOH is the net cost divided by the expected generated energy over the products lifetime, and is used for comparing energy cost coming from different systems or sources, such as fossil fuels.

Thermo-Differential Valve

Figure 1.2 shows a schematic overview of the TDV and its working principle. This valve consists of an actuator, which is a hollow tube that has a float on one side and a small container on the opposite side. The float is located inside the

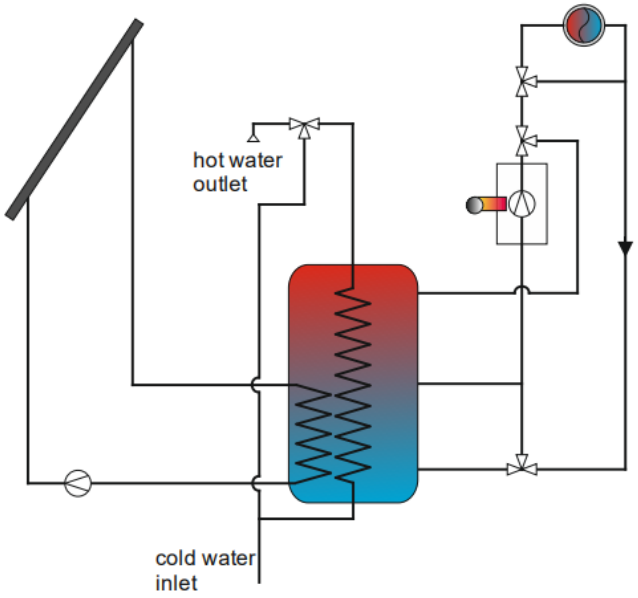

Figure 1.1 — Layout of the reference solar combisystem used in the calculation of TASK54 [Bachmann,2017]

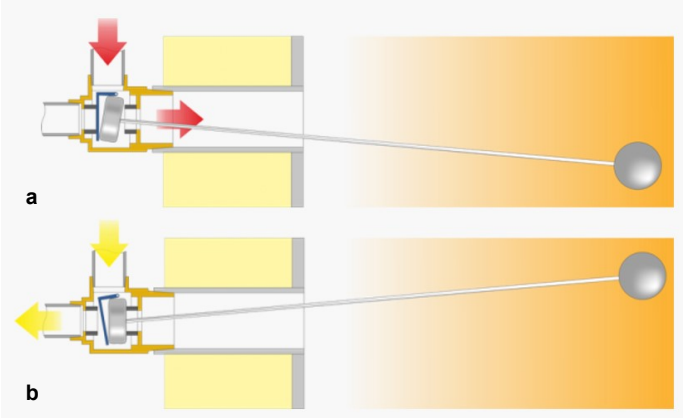

Figure 1.2 — The position of the TDV at different temperature differences. In situation a, the temperature in the storage tank is lower than the output of the solar collector (open), while situation b, shows the opposite (bypass) [Conico Valves bv, 2017]

storage tank, while the small container is located in the valve housing. A working fluid is available in the actuator that either moves towards the float or to the small container depending on the temperature difference between the storage tank and collector output. This movement occurs at a very small temperature difference in a rapid pace (less than a second). The TDV is in open position when the temperature in the storage tank is lower than the solar collector output, Figure 1.2a. Under this circumstance the working fluid flows in the float and as a result the float sinks, allowing water from the collector output to flow into the storage tank. The TDV is in bypass position, Figure 1.2b, when the temperature in the storage tank is higher than the solar collector output. In this case the float is filled with vapor and rises up, thereby closing the storage tank inlet.

Conico Valves system

The CV-system is a direct solar combisystem that uses the TDV for autonomous control of storing heat; a schematic overview of this system is presented in Figure 1.3. This system consists of an evacuated tube solar collector (ETSC), insulated copper piping, a solar circulation pump with controller, a thermal storage tank, auxiliary heating component, and two temperature sensors (one at the $ETSC_{in}$ and one at the $ETSC_{out}$); these sensors are incorporated in the pumping station. The CV-system also uses a thermosiphon valve that creates, in combination with the TDV, a water-based system with a reliable frost protection mechanism, which does not require power. Therefore, this system is suitable for colder climates such as in central and northern EU. Also, it increases the reliability and decreases the costs because of the two temperature sensors in the pumping station, in comparison to the two other solar combisystems that are discussed in the introduction. However, the thermosiphon valve was not implemented in the system used in the numerical research of this thesis, as the implementation of thermosiphon flow effects in TRNSYS is extremely complex and might not even be possible.

The CV-system operates with two different control strategies: (i) start stop operation and (ii) continuous operation. The pump has to circulate periodically at the startup of the CV-system, referred to a start stop operation, for measuring the temperature inside the ETSC, as the temperature sensors are incorporated in the pumping station. Because of the TDV, the ETSC output will bypass the storage tank as long as no heat can be added to the storage tank. This start stop operation is used, for instance after each night, to determine whether there is a sufficient irradiation level for the CV-system to operate continuously, which is similar to conventional solar combisystems; this operation is referred to as continuous operation. If the temperature in the ETSC drops below a pre-set value under continuous operation, for example due to insufficient irradiation, the pump starts to circulate periodically again. When the temperature decreases even further (near freezing temperature) despite using a start stop operation, the thermosiphon valve opens to allow hot fluid to flow from the storage tank to the solar collector loop. This thermosiphon valve is designed to minimize the heat loss for frost protection, which means that only in utter need heat is extracted from the storage tank.

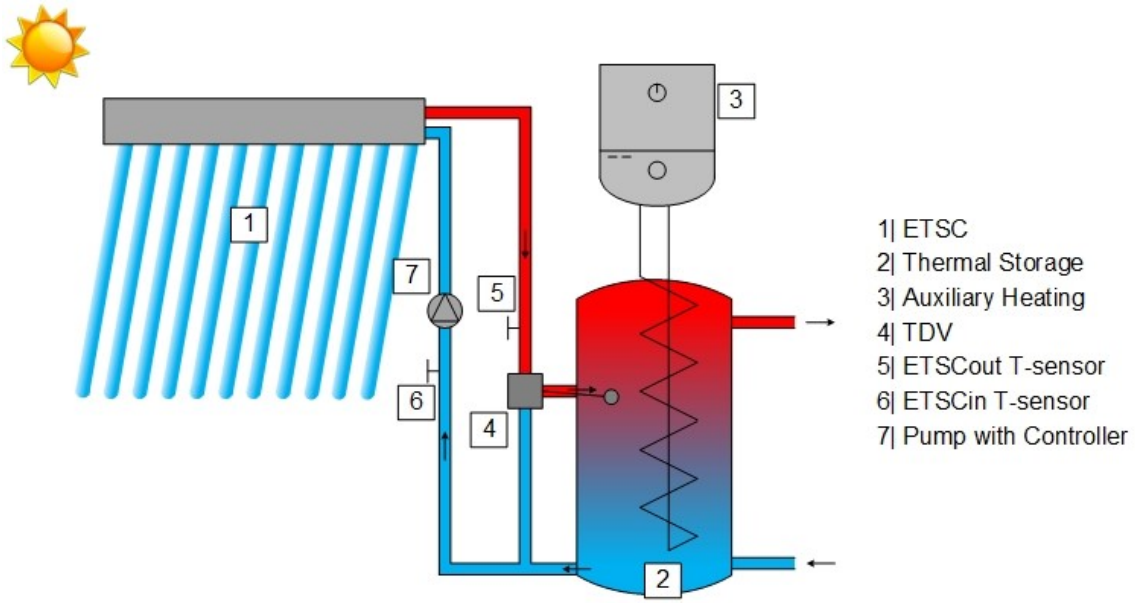

Figure 1.3 — Layout of the CV-system showing the location of the main components. One of these components is the TDV designed by Conico Valves bv.

1.2 Aim of the Study

This report focusses on two key research topics that are related to the CV-system, namely on (i) the thermal performance of an ETSC, and (ii) simulation of the CV-system in TRNSYS. Therefore, this thesis was divided into an experimental research and a numerical research.

Experimental Research

Because of the implementation of the TDV in the CV-system, which allows for bypassing the storage tank, this system could be entirely operating with a continuous flow rate. However, it is unknown whether there is a difference between thermal performance of an ETSC using a stagnant flow (for start stop operation) and a continuous flow rate, and which of these flows is more beneficial. This is of interest when there is a low level of irradiation available, particularly during the morning and evening.

An experimental research was conducted only on the ETSC that is used in the CV-system. Also, the use of a theoretical model of an ETSC was restricted to determining the parameters that could influence the thermal performance; this model was not used for a comparison with the experimental data. As a result, the following main research question was formulated:

What is the influence of a continuous mass flow rate, at different mass flow rates, and a start stop mechanism on the thermal performance of the ETSC used in the CV-system?

Numerical Research

As mentioned in Paragraph 1.1, TRNSYS was used as simulation software for determining the LCOH of the reference system by engineers of ITW. These engineers will eventually also evaluate the LCOH of the CV-system. For this reason, research had to be conducted whether this software is suitable to simulate the CV-system. This system is dependent on highly dynamic behavior due to the TDV, as a result, it was unknown whether TRNSYS is capable of accurately simulating a realistic TDV behavior. This behavior directly influences the stored heat in the CV-system and with it the overall thermal performance. Consequently, another main research question was formulated:

Is the simulation software TRNSYS18 capable of accurately simulating the CV-system?

The numerical research was limited to using the standard library and extended TESS library of TRNSYS. The working principle of this simulation program is explained in chapter 4. Furthermore, this report does not include the development of an optimized control strategy for the CV-system, but instead describes an analysis of the CV-system in TRNSYS. Additionally, this report does not discuss a yearly simulation of the CV-system, so it does not discusses a comparison between the CV-system and the reference model from TASK54. Yet, this reference system was used for determining the simulation parameters.

1.3 Research Method

Each of the research topics was conducted with its own method, which is described in this paragraph.

Experimental Research

The first step in this research was to create an experimental setup that is suitable for determining the thermal performance of the ETSC. Even though this was not the main focus of this study, it was necessary for acquiring useful data. This experimental setup was designed using the solar thermal testing norm NEN-EN-ISO 9806 as a guideline and designed to easily fit different (types of) solar collectors. Furthermore, a verification of this setup was needed to check the accuracy of the measurement devices and overall performance, such as volume flow stability.

Before the research plan was constructed, a theoretical model of an ETSC was investigated. The results from this study were to clarify which parameters can influence the thermal performance of an ETSC. Moreover, a literature study was conducted on acquiring a method for comparing experimental data related to the thermal performance of an ETSC.

The main research question was divided into three sub-research questions that were based on the theoretical model. These sub-research questions were individually tested for minimizing the number of required experiments. Also, these questions had to be conducted in a specific order as the results of research question one were needed in the second and third sub-research questions.

Numerical Research

The first part of the numerical research was to conduct research on each individual component in the CV-system. Firstly, a simulation type was gathered from the TRNSYS library and extended TESS library for each component; for example, the pump and ETSC. These components were investigated whether they could be used for realistically simulating the CV -system. Furthermore, a simulation component for the TDV was developed as this is a novel concept, which therefore was not available in TRNSYS.

Secondly, the CV-system was simulated for continuous operation and start stop operation. During the numerical research, the influence of the number of nodes and simulation time step on the thermal performance were investigated in order to find the optimum combination. Both these parameters influences the simulation calculation time, thus for a yearly simulation the optimum combination will result in the least calculation time needed to accurately simulate the CV-system.

1.4 Outline of Thesis

As there were two different research topics conducted during the master thesis, this report is divided into two sections: experimental research (part 1) and numerical research (part 2). Firstly described in part 1 is the experimental research designed by [Balkom, 2015] and the design requirements for the improved experimental setup, chapter 2. This chapter also describes the new thermal layout of the improved experimental setup and the validation of this setup. Secondly, chapter 3 discusses the theoretical model of an ETSC, the results found in the experimental research, and a sensitivity analysis.

The second part of this report describes the system layout and the simulation models used in TRNSYS, chapter 4. Furthermore, this chapter discusses the analysis performed on these components in order to find their accuracy compared to realistic operation. Chapter 5 discusses the two cases that were analyzed and their results: continuous operation and start stop operation.

Chapter 6 concludes on both the research topics and presents recommendations for further research.

Part 1 — Experimental Research

2| Design of Experimental Setup

The first research that was conducted during this thesis was to investigate the thermal performance of a solar collector that is used in the CV system. In previous studies at Eindhoven University of Technology, the performance of photovoltaic thermal (PVT) panels was investigated using an experimental setup described in [Balkom, 2015]. This setup used a solar simulator from the company Eternal Sun, which light having a spectrum similar to the solar spectrum. Because the solar simulator is independent on weather conditions, a controlled study on the performance of PVT panels can be conducted. Furthermore, PVT panels have a thermal and electric performance; therefore, the experimental setup was divided into two systems: a thermal circuit and an electric circuit. The entire setup was designed according to NEN-EN ISO 9806 norm for solar thermal testing.

For this thesis, only the thermal performance of a solar collector was of interest, thus only the thermal circuit. The original thermal system had a closed loop configuration of components, though due to the thermostatic bath it was an open circuit. This thermostatic bath circulates, extracts heat from the fluid and is therefore used for regulating the PVT-panel inlet temperature. Furthermore, a needle valve is used for controlling the volume flowrate of the fluid, which is measured using a volume flowmeter. Unfortunately, there are several issues with this setup regarding research possibilities on the performance of solar collectors.

The main issue of this setup is that it was designed for volume flowrates related to PVT-panels, which are in the range between 15 and 120 L hr^{-1}. On the contrary, the ETSC's that are used in the CV system, have a flow range between 120 and 360 L hr^{-1}. Hence the needle valve and flowmeter of this setup could not be used. Another issue is that the pump in the thermostatic bath generates fluid pulses instead of a continuous flow, resulting in an inconsistent volume flow through the system and thus through the collector. Furthermore, the tubes, which have a minimum inner diameter of 4 mm, are too small for acquiring higher velocities. Therefore, this experimental setup could not be used for measuring the thermal performance of the ETSC's. As a result, a new experimental setup was designed and build during this thesis.

This chapter describes the design process for this new experimental setup that can be used for ETSC's as well as PVT -panels. Paragraph 2.1 describes the design parameters for both these collector types and the NEN-EN-ISO 9806 norm for solar thermal testing. An overview of the new experimental setup is shown in paragraph 2.2, while several individual components are described in paragraph 2.3. Finally, paragraph 2.4 discusses the calibration and verification process of the setup.

2.1 Design Requirements

The old experimental setup was based on design requirements set by NEN-EN-ISO 9806 norm for solar thermal testing [NEN-EN-ISO, 2013] and various demands of the PVT panel manufacturers [Balkom, 2015]. These requirements are still applicable for the design of the improved experimental setup. However, the list of requirements was extended with requirements for solar collectors, which are used in this thesis [Ruth, 2017], and for PVT panels [Rijvers, 2018]. The design requirements are divided into three categories, namely temperature, flow, and miscellaneous. The design requirements for the light source are not discussed, as the same solar simulator was used as described in [Balkom, 2015].

2.1.1 Temperature

NEN-EN-ISO 9806 specifies three different temperature measurements: inlet temperature of the collector, outlet temperature of the collector, and the ambient temperature. Each of these measurements have their own accuracy and placement requirements, which influences the design of the components used in the experimental setup.

The inlet and outlet temperatures of the collector measurements require a temperature sensor with a standard uncertainty of 0.1 K. Also, a resolution of ±0.02 K is required for obtaining data to confirm that the temperature does not drift over time, thus a datalogger with at least a 12-bit digital system is needed. The difference between the collector inlet and outlet temperature should be measured within a standard uncertainty of 0.05 K. These temperature sensors should be placed within 200 mm of the inlet and outlet of the collector and the pipework upstream and downstream of the sensor must be insulated. Mixing of the fluid is required for temperature measurements and can be ensured by using a bend in the pipe works, an orifice or a fluid mixing device. Furthermore, the collector inlet temperature must be kept stable within the range of ±1 K.

The accuracy of the ambient temperature measurement must have a standard uncertainty within 0.5 K. The temperature sensor must be placed near the surface of the collector and shielded from direct radiation for minimizing radiation exchange. Finally, according to [Balkom, 2015] the temperature range in built environment is between 10 °C (cold tap water) and 60 °C (hot tap water). This temperature range also spans the requirements for this thesis and the PVT panels.

2.1.2 Flow

The flowrate is also an important parameter in determining the thermal performance of a solar collector and PVT panel, so it is crucial to have a continuous flowrate. According to NEN-ISO EN 9806 the flowrate should be kept fixed within 2 % of the set flowrate during a time cycle for steady state conditions and within 1 % for quasi-dynamic conditions. Also, the flowrate may not differ more than 10 % between two experiment cycles that uses the same set flowrate. Table 2.1 shows the flowrates used in three different research topics. As can be seen, the improved experimental setup should be able to acquire a volume flowrate between 0.25 and 6 L min^{-1}. Furthermore, the pump should have sufficient capacity to overcome pressure drops that occur in the system.

Table 2.1 — Volume flow range used in three different research topics.

Research Topic	Volume Flow Range [L min^{-1}]
M.W. van Balkom	0.25 - 2.00
P.M. Rijvers	0.33 - 2.00
ETSC	2.00 - 6.00

In the experimental setup from [Balkom, 2015], a volume flow meter was used and was proven to be an effective tool for determining the mass flow. An important notice is that [Balkom, 2015] assumed a constant density over the temperature range between 10 to 60 °C. Therefore, the same method was used in the improved setup. According to NEN-ISO EN 9806, the volume flowrate needs to be measured within an accuracy of ±1 % of the measured value, so a digital logging device is needed for accurate time measurements of the volume flowrate.

2.1.3 Miscellaneous

Besides requirements on temperature and flowrate, there are also requirements for several other components in the thermal system, such as the pipes. NEN-ISO EN 9806 states that the pipes should be kept as short as possible, especially around the inlet and outlet of the collector, to decrease the influence of the environment on the temperature. Also, an insulation value of maximum 0.2 W K^{-1} should be used for the pipes for preventing heat loss to the environment. Additionally, the pipes must be shielded from solar radiation.

Pressure measurements are used to determine whether there is a pressure drop over the collector, what the pressure level is during experiments, and if there is a leakage. These pressure measurements should have an accuracy of less than 5 % of the measured value or ±10 Pa. Incorporation of a short piece of transparent tube makes it possible to observe whether the fluid is contaminated or air bubbles are present in the fluid. To avoid particles to enter the system, a filter with a nominal size of 200 µm should be placed. Lastly, a tap connection should be made for filling the entire system with tap water.

2.2 Experimental Setup

The improved experimental setup is divided into four different categories, namely the solar simulator, solar collector, thermal circuit and electrical circuit. As mentioned in paragraph 2.1, the same solar simulator was used as described in [Balkom, 2015] and is therefore not discussed in this thesis. Also, no changes were made to the electrical circuit, as this thesis only focusses on the thermal performance of ETSC. The setup was properly designed, as different solar collectors or PVT panels can easily be connected to the thermal circuit. As a result, each user is able to integrate a solar collector or PVT panel with their own temperature sensors.

Figure 2.1 shows an overview of the thermal circuit of the improved experimental setup and the location of the solar collector/PVT panel, whereas Figure 2.2 shows actual footage of the thermal circuit. As can be seen, the thermal circuit consists of two different cycles: a cooling cycle and a solar collector cycle that are connected with a bypass. The cooling cycle has the purpose of absorbing heat that is generated in the solar collector due to radiation of the solar simulator. The solar collector cycle has several functions, namely generating a constant volume flowrate, obtaining volume flowrate and temperature data, and integrating the design requirements discussed in paragraph 2.1. The bypass is used in case a new solar collector or PVT panel is connected to the thermal circuit, then the solar collector cycle can be filled with water through the cooling cycle (thermostatic bath).

2.2.1 Thermal Circuit: Cooling Cycle

The cooling cycle consists of a thermostatic bath, thermostatic valve, connection to one side of the bypass, and a counter flow plate heat exchanger. The same thermostatic bath as in [Balkom, 2015] was used, namely the Unichiller 015-H-MPC of manufacturer Huber; Appendix A.1 discusses the design choice of this thermostatic bath. This bath is used for controlling the volume flowrate and temperature in the cooling cycle; because of this bath, this cycle is an open circuit. The internal pump of this bath is sufficient as the volume flowrate in the cooling cycle does not require a precise continuous flow; there are no boundaries for deviation in volume flowrate. Warm water flows from the plate heat exchanger into this bath and is cooled to a set temperature.

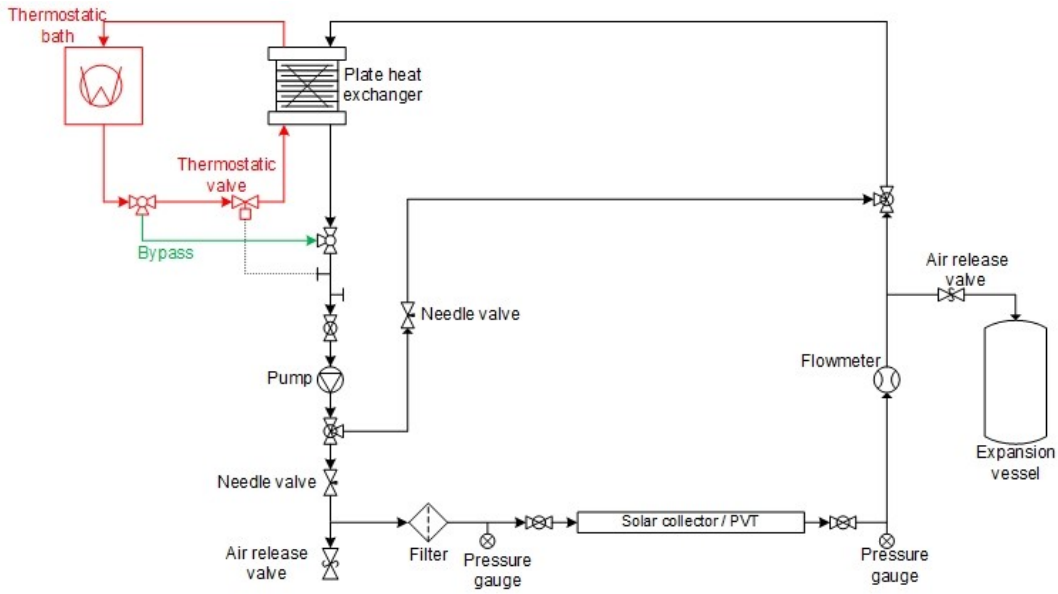

Figure 2.1 — Schematic overview of the thermal circuit used in the improved experimental setup. The cycle containing the thermostatic bath and thermostatic valve is called the cooling cycle (red), and the cycle containing the pump, filter, solar collector and flowmeter is called the solar collector cycle (black). The by-pass is indicated in green.

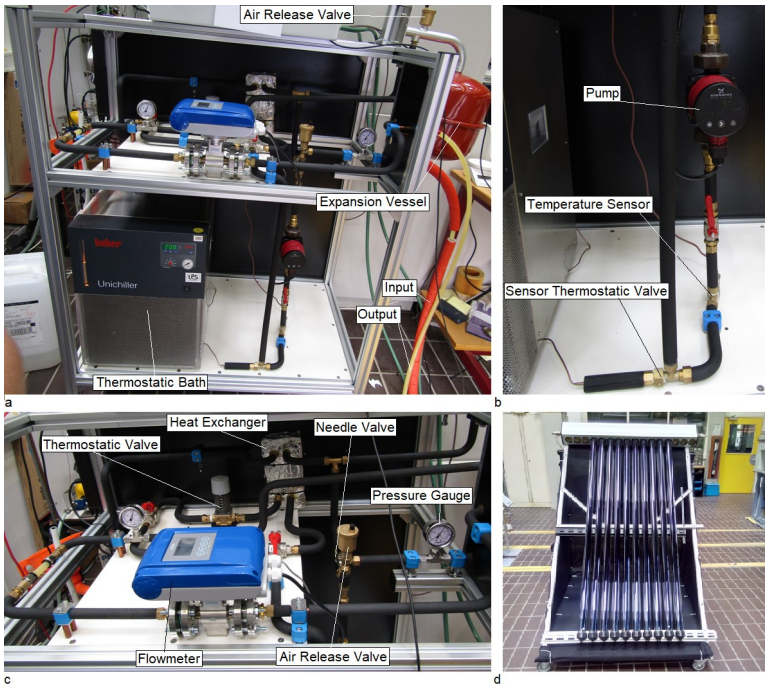

Figure 2.2 — Footage of the thermal circuit (a, b and c) and solar collector (d)

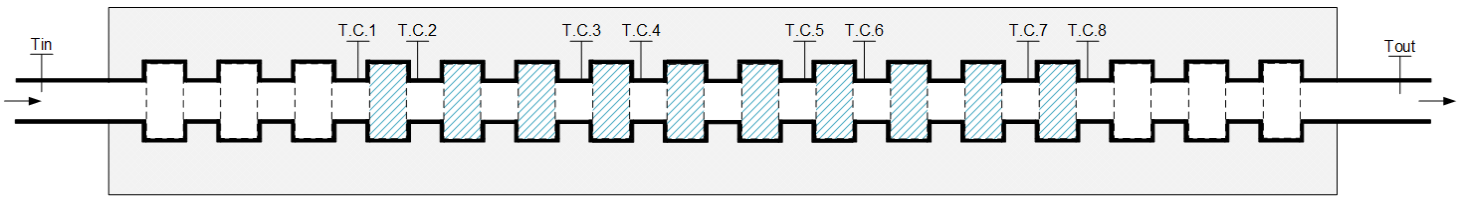

Figure 2.3 — Schematic overview of the thermocouples placed in the manifold of the ETSC. A thermocouple is placed on either side of the ETSC and 8 thermocouples inside the manifold at locations where there is a vacuum tube placed (shaded areas)

A thermostatic valve is placed after this bath that is connected to a temperature sensor, which is placed in the solar collector cycle, to acquire the desired temperature in the solar collector inlet. A thermostatic valve is used for mechanical flow regulation based on a desired temperature setting. Therefore, this valve automatically controls the volume flowrate in the cooling cycle for acquiring the desired solar collector inlet temperature. The AVTA 15 with absorption charge, from manufacturer Danfoss, was used as thermostatic valve, Appendix A.1.

Finally, this cycle is connected to a counter flow plate heat exchanger for optimum absorption of heat. A stainless steel brazed plate heat exchanger B3-12-10, from manufacturer Hrale, was used in the improved experimental setup. This heat exchanger consists of 10 plates, has a maximum power of 22 kW, and has a maximum volume flowrate capacity of 67 L min^{-1}. Appendix A.1 discusses the design parameters and procedure for this heat exchanger.

2.2.2 Thermal Circuit: Solar Collector Cycle

In the solar collector cycle, a continuous volume flowrate is required with a maximum deviation of 2%, as described in paragraph 2.1. This flowrate is acquired using a centrifugal pump (Alpha 2 25-40 auto adapt circulation pump from manufacturer Grundfos, Appendix A.1) that is controlled by two needle valves. One of these valves is installed in a bypass that connects the inlet of the solar collector with the outlet of the solar collector. The needle valve in the bypass allows adjustment of the volume flowrate without increasing the pressure in the improved experimental setup. This valve cannot be used on its own for acquiring low volume flowrates as the volume flowrate output of the pump is too high. Consequently, another needle valve is installed in the piping towards the inlet of the solar collector. The combination of these valves assures that low volume flows can be reached without increasing the pressure in the improved experimental setup.

As the design requirements state, a filter is installed before the solar collector inlet and two pressure gauges are incorporated into the improved experimental setup, as required by the design requirements. These pressure gauges are placed before and after the solar collector for determining the pressure loss in the setup. Furthermore, two push-in couplings are used to easily (dis-) connect a solar collector or PVT-panel. Additionally, a magnetic volume flowmeter (Optiflux4000 from manufacturer Krohne), which is connected to a signal converter (IFC100 from manufacturer Krohne), is installed after the solar collector output, Appendix A.1. Installing the flowmeter at this location makes it possible to detect leakages in the solar collector, piping and connectors. Because this cycle is a closed loop, an expansion vessel with an air release valve is placed after the solar collector output for absorbing any excess water vapor caused by thermal expansion. Because the pump is installed vertically with a pipe bend above, air can be trapped in the pump and cause failures, thus a secondary air release valve is used to prevent air trapping. Finally, a temperature sensor, which is connected to a digital logging device (DAQ NI-9211), is placed after the temperature sensor of the thermostatic valve.

2.2.3 Solar Collector

As mentioned, each user is able to connect its own solar collector to the thermal circuit. In this thesis an ETSC (EtaSunPro HLK30 from manufacturer TWL) was used from which the location of the temperature sensors can be seen in Figure 2.4. Two T-type thermocouples were used for acquiring the inlet and outlet temperature of the ETSC, to determine the temperature difference and average temperature over the solar collector. These sensors were positioned in a pipe bend at 10 cm from the actual inlet and outlet of the solar collector as required from NEN-EN-ISO 9806. The temperatures inside the solar collector were measured using eight T-type thermocouples, which were positioned at the outer tube wall of the manifold. Furthermore, the ambient temperature was measured using a K-type thermocouple and a pyranometer was used for measuring the intensity of the solar simulator.

2.3 Verification

Verification of the experimental setup is essential to determine the accuracy of the measurements as well as to verify if the measurements operate according to the NEN-EN-ISO 9806 norm. In the improved experimental setup there were three different topics that needed verification before the setup could be used for measurements: (i) calibration of the temperature sensors, (ii) analysis of input temperature, and (iii) volume flow control. This section describes the procedures and results found during the verification.

2.3.1 Temperature Sensor Calibration

A thermocouple consists of two wires of different metals that are connected to a data acquisition (DAQ) device, the reference junction, and fused together at the other end in order to create a measurement junction, the hot junction. When the temperature changes at the hot junction, the metals will start to deform and with it its resistance. This change in resistance results in a change in microvolt that, due to the difference compared to the reference junction, can be associated to a temperature; this is referred to as the Seebeck effect.

In the improved experimental setup both T-type and K-type thermocouples are used, which not only differ in material properties but also differ in measuring accuracy, temperature range, and application. Another difference between the

T-type and K-type thermocouple used in this setup is that the T-type thermocouples are housed in a metallic tube (thermocouple probe), which allows the thermocouple to be used in fluids, while the K-type is not. This paragraph describes the calibration method and results of the thermocouples used in the improved experimental research.

Method

The calibration of a measuring device can be distinguished into a *systematic error* and a *random error*. Both these errors were determined for each thermocouple using a similar procedure used in [Balkom, 2015], which is shown in Figure 2.4. All the thermocouples used in the setup were connected to an NI-9211 thermocouple module for DAQ at their reference junction, while the hot junction were submerged for 5 cm in a thermal bath; a thermal bath was used for acquiring three different constant temperatures. A calibrated T-type thermocouple was connected to a Memocal 2000 thermocouple calibrator and also submerged with the other thermocouples. The distance between the hot junction of each thermocouple was minimized, by binding the thermocouples together using a cable binder, and as a result the temperature inhomogeneity was minimized. The data was logged using the software Labview Signal Express; each thermocouple used a number of *N* datapoints to determine both errors.

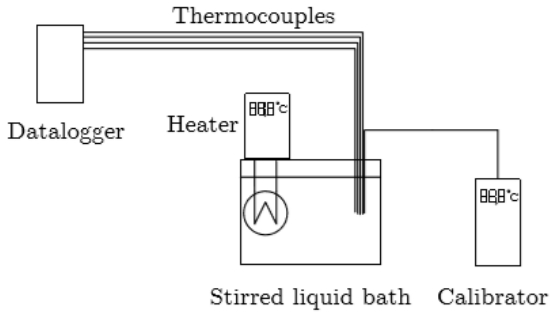

Figure 2.4 — Schematic Overview of the thermocouple calibration setup, also used in [Balkom, 2015]

Systematic error

A systematic error is defined as a consistent, repeatable error that always occurs during a measurement (in other words the mean offset between measurement value and actual value). In case of the thermocouple calibration, the systematic error (μ) is the average temperature difference between the calibrator (T_{cal}) and the thermocouple (T_{TC}) over a number of *N* datapoints and was determined by equation 2.1. The systematic error of each thermocouple is shown in Table 2.3.

$$\mu = \frac{1}{N}\sum_{j=1}^{N}\left(T_{cal,j} - T_{TC,j}\right) \qquad 2.1$$

Random error

A random error is defined as an unpredictable error that is not consisted by repeating measurements (the number of doubt). The random error is based on the standard deviation (σ) of the thermocouple. Equation 2.2 presents the relation between the standard deviation and a number of N datapoints for this thermocouple calibration.

$$\sigma = \sqrt{\frac{1}{N-1}\sum_{j=1}^{N}(\mu - T_{cal,j} + T_{TC,j})^2} \qquad 2.2$$

The results found from equation 2.2 gives a level of confidence of 68% and in order to increase this level to 95% ($\sigma_{95\%}$), the results have to be multiplied with a factor of 2. Additionally, an estimation of the random error decreases when more datapoints are averaged. Consequently, dividing $\sigma_{95\%}$ with the number of N datapoints, results in the random error (z) of the thermocouple (equation 2.3); the random error of each thermocouple is presented in Table 2.3.

$$z = \frac{\sigma_{95\%}}{\sqrt{N}} \qquad 2.3$$

Combined Error

The combined error of a measurement consists of the random error of each measuring device as well as errors from different components in the calibration setup, such as the uncertainty of the calibrator unit. The relation between the combined uncertainty error (z_{comb}) and a number of *m* individual uncertainty errors (z_i) is presented in equation 2.4.

$$z_{comb} = \sqrt{{z_1}^2 + {z_2}^2 + \cdots + {z_m}^2} \qquad 2.4$$

In some measurements two variables are correlated to one another, for example measuring the temperature difference (ΔT) over the ETSC requires two temperature sensors. In this case, a covariance term is needed to compensate for using two temperature sensors (sensor 1 and sensor 2), equation 2.5; *x* stands for the temperature difference between the calibrator and the thermocouple. The overall combined uncertainty error for this example is presented in equation 2.6 and accounts for both the temperature difference of the ETSC as well as the mean temperature (T_M) over the ETSC.

$$z_{1,2} = \frac{1}{N-1}\sum_{i=1}^{N}\left(x_{1,i} - \mu_1\right)\left(x_{2,i} - \mu_2\right) \qquad 2.5$$

$$z_{comb} = \sqrt{{z_1}^2 + {z_2}^2 + \cdots + {z_m}^2} \qquad 2.6$$

Results

Several uncertainties were acquired during the calibration procedure, for instance the uncertainty in the temperature inhomogeneity of the thermal bath, though the hot junctions of the thermocouples were bound together. According to [Balkom, 2015], the inhomogeneity of this thermal bath has a value of 0.1 °C. However, there is a pump available in the thermal bath that mixes the fluid for a better homogeneity, resulting in an inhomogeneity of less than 0.1 °C [Huijzer, 2018]. Another uncertainty is found in the resolution of the calibrator display as it only shows one decimal, which means that the value on the displays varies between ±0.05 °C. As a result, the standard uncertainty becomes 0.1 °C and this value has a rectangular probability distribution according to [Balkom, 2015]. Finally, the measuring device of the thermocouples (NI-9211) has a standard uncertainty of 0.01 °C. Table 2.2 shows the procedure for one thermocouple, while the combined standard uncertainty is presented in Table 2.3.

As can be seen in Table 2.3, the standard uncertainty of the thermocouples at the inlet and the outlet (0.12 and 0.13 ° C) of the ETSC were slightly higher than the design requirements (0.1 °C), paragraph 2.1; however, Table 2.2 shows that this standard uncertainty mainly was due to the inhomogeneity of the thermal bath. As mentioned before, the value for the inhomogeneity is less than the calculated value, which means that the standard uncertainty also is less than the values presented in Table 2.3. When the inhomogeneity is assumed to be 0.05 instead of 0.10 °C, then the standard uncertainty reduces to 0.08 °C, which is lower than the design requirement. Furthermore, the $\Delta T/T_M$ has standard uncertainty (0.04 °C) lower than the design requirement (0.05 °C), thus it was concluded that the standard uncertainties are allowed according to the design requirements.

2.3.2 Temperature Input

A validation was needed in order to determine whether the temperature at the inlet of the ETSC met the design requirements stated in paragraph 2.1. Moreover, this validation was used to verify the accuracy in which the temperature in the improved experimental setup could be controlled. During the validation procedure, three measurements were conducted using three different temperature settings (10, 30 and 50 °C) and two thermocouples: (i) the thermocouple located at the temperature sensor of the thermostatic valve and (ii) the thermocouple at the inlet of the ETSC. In each measurement the solar simulator emitted solar radiation (PV800 setting), therefore, the inlet temperature of the ETSC was given time to stabilize; thereafter, each measurement ran for 5 minutes.

Figure 2.5 presents the temperature profiles (T_{TC}), the temperature deviation ($T_{z.min}$, $T_{z.max}$) due to the standard uncertainty of the thermocouple, and the minimum and maxi-

Table 2.2 — Example of determining the combined uncertainty error based on the parameters used in the calibration setup

Quantity	Value	Divisor	z
Calibrator resolution	0.10	√3	0.06
Resolution of datalogger	0.01	1	0.01
Inhomogeneity	0.10	1	0.10
Thermocouple	0.10	6	0.04
Zcomb			0.12

Table 2.3 — The systematic (μ) and random error (Z_{comb}) of the thermocouples used in the experimental setup

Thermocouple	μ [°C]	z_{comb} [°C]
Setup	- 0.07	0.12
Input	- 0.08	0.12
Output	- 0.10	0.13
Environment	- 0.05	0.18
TC1	- 0.10	0.16
TC2	- 0.01	0.16
TC3	0.03	0.13
TC4	0.17	0.18
TC5	0.10	0.16
TC6	0.00	0.12
TC7	0.07	0.21
TC8	0.07	0.13
$\Delta T / T_M$		0.04

mum allowed boundary level (T_{min}, T_{max}), for each measurement and thermocouple. The minimum and maximum boundary levels are based on the average temperature of a measurement ±1 °C. As can be seen in this figure, the temperature profile, including the temperature deviation, fits easily between the boundary levels for each measurement meaning that the stability of the temperature can be achieved for at least 5 minutes.

The figure also shows that different temperatures were observed between the two thermocouples. While an average temperature of 12.5 °C was obtained at the thermostatic valve temperature sensor using a temperature setting of 10 ° C, the average temperature at the inlet of the ETSC was around 10.5 °C. In addition, the average temperature at the thermostatic valve temperature sensor was approximately 47.6 °C, while the average temperatures was approximately 48.8 °C at the inlet of the ETSC; using a temperature setting of 50 °C. Both thermocouples had a temperature of approximately 29.7 °C at a temperature setting of 30 °C, the ambient temperature was approximately 24 °C during the measurements. Because the focus of the experiment was on the temperature stability rather than on reaching a temperature level, the difference between temperature setting and observed temperature was neglected.

The two thermocouples are placed in the improved setup with a distance of around 3 m from each another, where the thermocouple at the thermostatic valve temperature sensor is closer located to the cooling cycle. Because of this location, the temperature profiles and the ambient temperature, it could be concluded that the thermocouple at the thermostatic valve temperature sensor is incorrectly installed. It might be possible that this thermocouple is in contact with the outer wall of the tube, which is not insulated. Re-installing or replacing this thermocouple might result in a better performance; however, for the experimental research it was chosen to use the thermocouple at the inlet of the ETSC as inlet temperature setting.

2.3.3 Volume Flow Control

According to the design parameters in paragraph 2.1, the volume flowrate ranges between 0.25 – 6 L min^{-1}, having an accuracy of 2 % of the measured value. The deviation in volume flowrate was analyzed for a stagnant volume flowrate, which is presented in Figure 2.6. This figure shows that there is a deviation in volume flowrate, despite the absence of applying a volume flowrate by the pump. Thus, a signal noise was obtained over the output signal of the volume flowmeter. To reduce this noise, a Savitzky-Golay filter was used on the volume flowrate data. This filter smooths outs quick changes in the original signal to reduce signal noise [Savitzky, 1964], which is also shown in Figure 2.6. It can be seen in this figure that due to the filter a constant volume flowrate is obtained close to a stagnant flow. Therefore, this filter does eliminate the signal noise.

The same filter was used for different volume flowrates to identify the deviation in volume flowrate, which is presented in Table 2.4. Each measurement was given time to stabilize the volume flowrate (several minutes), followed by a measurement period of 5 min. Also, this measurement was used to obtain the highest volume flowrate that was possible with the improved experimental setup. As can be seen, the deviation in volume flowrate is significantly small compared to the average volume flowrate, and the maximum obtained volume flowrate was 5.0 L min^{-1}.

This data shows that the volume flowrate was measured according to the NEN-EN-ISO 9806 norm, with a flowrate between 0.2 and 5.0 L min^{-1}. Unfortunately, the volume flowrate that was stated in the design requirements was not met, even despite removing the filter that caused an increase in pressure resistance. It is recommended, in future reference, to apply a filter over the volume flow rate or to reduce the signal noise in the output of the flowmeter. This noise could be related to the influence of other appliances, such as the pump and thermostatic bath. Another reason could be that there is a signal noise in the connection from the flowmeter to the DAQ module, or because the output of the converter is not properly grounded.

2.4 Conclusion

Based on the data provided in this paragraph, it can be concluded that the improved experimental setup satisfies the design requirements stated in paragraph 2.1. Although the filter was removed, the maximum volume flowrate was optimized but is still limited due to the pressure resistance inside the volume flowmeter. However, a volume flowrate of 5 L min^{-1} is still quantified as a high-volume flowrate for a solar collector. Furthermore, the needle valves and the thermostatic valve could be replaced with electronic operating valves for acquiring an autonomous setup, which either uses the volume flowrate or the temperature for control operation. Finally, a new type of filter should be installed that does not lead to increasing the pressure resistance inside the setup, and more insulation is required in order to reach low temperatures (<10 °C).

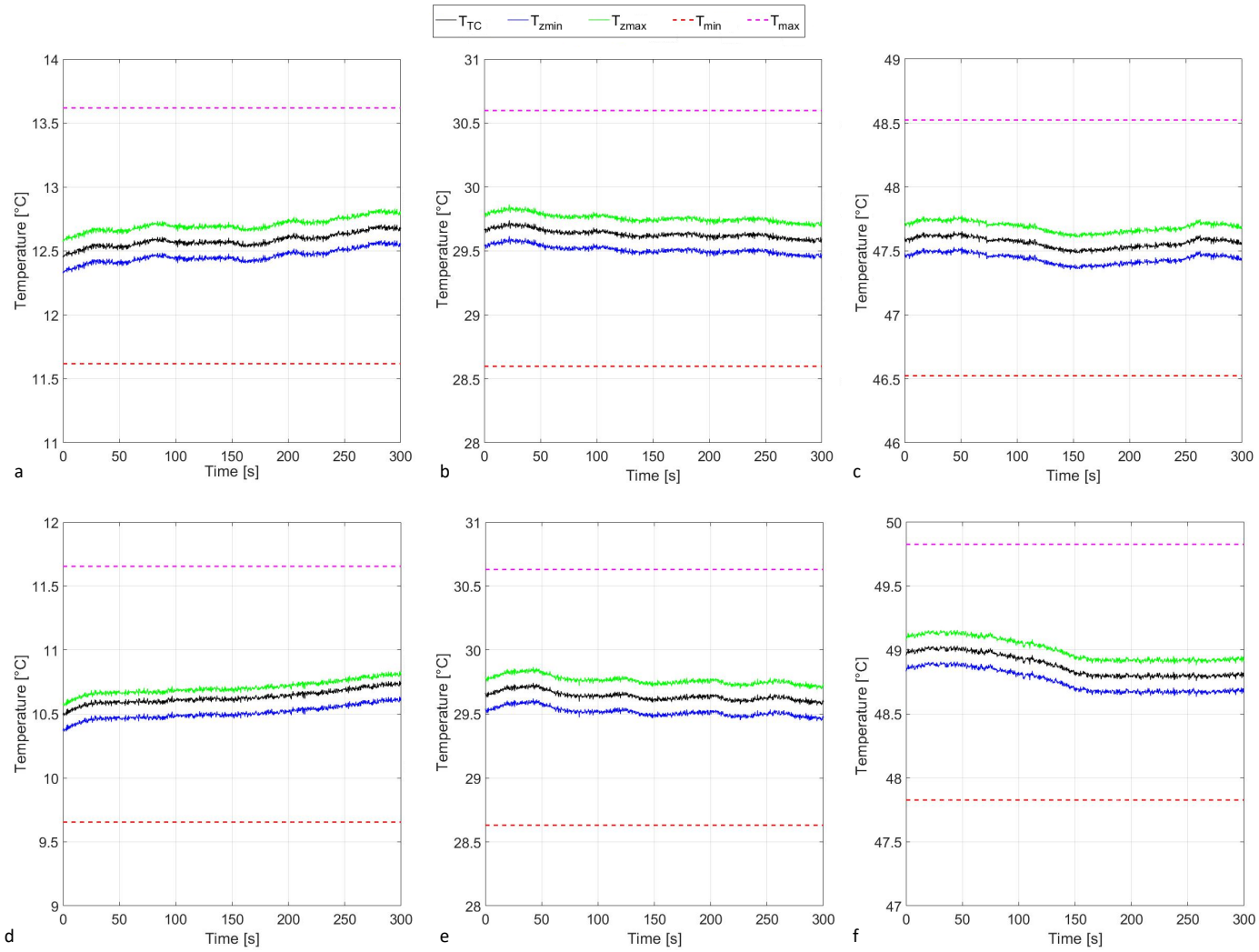

Figure 2.5 — Temperature profile at the setup for a set temperature of 10 °C (a), 30 °C (b) and 50 °C (c) over a measurement period of 5 min, and the temperature profile at the inlet of the ETSC for a set temperature of 10 °C (d), 30 °C (e) and 50 °C (f).

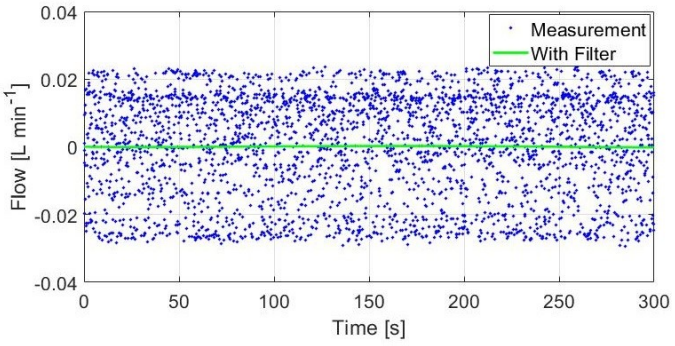

Figure 2.6 — Volume flow profile with and without the Sovitzky-Golay filter for a stagnant volume flow

Table 2.4 — Volume flowrates used in the volume flow validation. The table shows the average volume flow rate, the deviation over the measurement period, and the combined standard uncertainty. The standard uncertainty is based on the deviation and the calibration error shown in Appendix A.2

Volume flow [L min^{-1}]	σ [L min^{-1}]	z_{comb} [L min^{-1}]
0.0	0.0001	0.0001
1.0	0.0014	0.0015
2.0	0.0012	0.0016
5.0	0.0054	0.0060

3| Experimental Research

As stated in chapter 1, one of the research topics of this master thesis was to determine the influence of a continuous volume flow and a start stop mechanism on the thermal performance of the ETSC used in the CV-system. In order to find an answer for the main research questions, four sub-researches were formulated. The first sub-research question is related to the different parameters that influence the thermal performance of an ETSC. A theoretical model was used to identify these parameters, which is described in paragraph 3.1. The following sub-research question was formulated:

(1) What parameters influence the thermal performance of an ETSC and how are they related to one another?

Based on the findings from sub-research question 1, three more sub-research questions were formulated:

(2) What is the effect of inlet temperature on the thermal performance of an ETSC and what are the loss coefficients and optical efficiency of the ETSC?

(3) What is the influence of solar radiation on the thermal performance of an ETSC.

(4) What is the influence of the volume flow, inside the manifold, on the optical performance of an ETSC?

Paragraph 3.2 describes the purpose, research method and the results of sub-research question 2, while paragraph 3.3 discusses the same topics for sub-research question 3. Sub-research question 3 is divided in two several methods, which are both described in paragraph 3.4. Moreover, this paragraph discusses the results of two different measurements, and both the continuous volume flowrate measurements and start stop measurements were conducted and compared. Finally, paragraph 3.5 elaborates the sensitivity analysis of the measurements.

3.1 Theoretical Model of an ETSC

The solar collector used in this thesis was an ETSC, which is also called a vacuum heat pipe collector, and has a similar working principle as a thermo flask; the tubes are evacuated (vacuum) in order to reduce convective and thermal radiative heat losses. A schematic overview of an ETSC and its working mechanism is presented in Figure 3.1a. The main components in an ETSC are the evacuated tube, heat pipe and the manifold. An ETSC consists of three mechanisms, namely (i) the absorption of solar radiation, (ii) transfer of heat in the heat pipe, and (iii) the transfer of heat from the heat to the working fluid in the manifold. Besides this theoretical model, there is also an approximation model for determining the thermal performance of an ETSC based on experimental data.

Absorption of Solar Radiation

Solar radiation (IA) is absorbed inside the vacuum tube that consists of several materials: two layers of glass separated by a vacuum space, and a three layered absorption coating added on the inner glass layer, consisting of a copper, aluminum, and aluminum-nitrogen layer. Often borosilicate glass layers are used as it transmits more radiation than ordinary glass while maintaining a similar tensile strength. A cross-section of a vacuum tube and its working mechanism are shown in Figure 3.1b.

Solar radiation encounters the outer glass layers, where it is absorbed (α) in the material, reflected (ρ) and transmitted (τ) [Riffat, 2003]. Because of the borosilicate material properties and the vacuum space, there is limited heat exchange between the two glass layers and almost all heat is transmitted through the outer layer. The inner glass layer has the same material properties as the outer glass layer, meaning that almost all heat is transmitted through the inner glass layer. Therefore, an absorption coating is applied on the inner glass layer to optimize absorbing of the transmitted heat (τ_g) and minimize losses through transmission and reflection. The absorbed heat is collected in an aluminum heat transfer fin that transports this heat towards the heat pipe.

Heat transfer in the Heat Pipe

The heat pipe inside an ETSC is basically a hollow copper pipe that is partially filled with water under vacuum conditions. Due to these vacuum conditions, the water will boil at a temperature of roughly 30 °C. The heat pipe is divided into two parts, namely the evaporator and the condenser; shown in Figure 3.1c. The part where the heat pipe is located in the evacuated tube is referred to as the evaporator, while the condenser is the piece of heat pipe that is present inside the manifold.

The heat, transported through the aluminum fin, travels through the copper layer of the evaporator by means of conduction [Azad, 2007]. Due to this heat, the water inside the heat pipe is evaporated under influence of convection, thereby turning it into hot vapor that will rise upwards to the condenser; assuming that the ETSC is installed under an angle. The condenser transfers the heat from the vapor to the working fluid in the manifold, resulting in enough energy loss in the water vapor to convert it back into the liquid state. The water flows back to the evaporator, under influence of gravity, where the process is repeated. This water flows at the sides of the heat pipe resulting in the creation of a condensa-

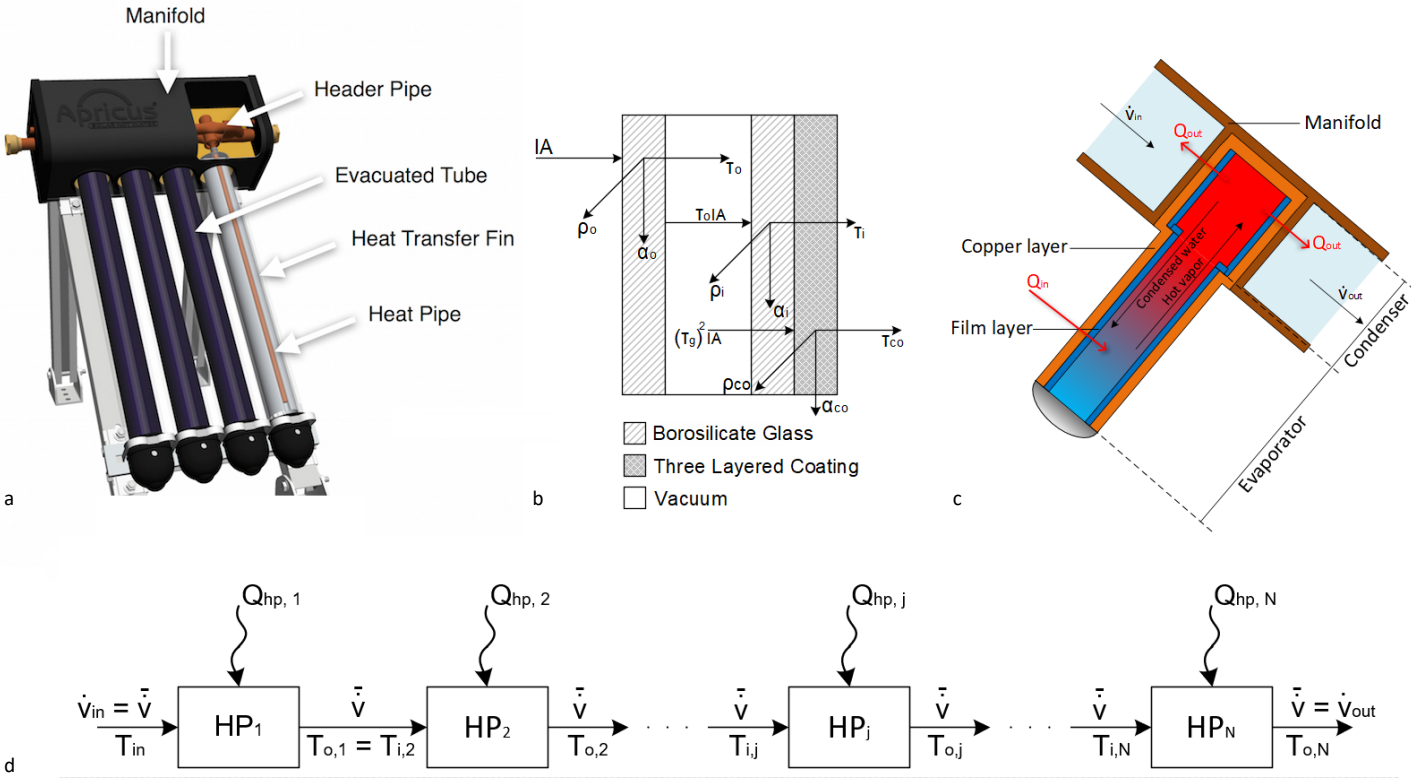

Figure 3.1 — a) A schematic overview of main components in an ETSC [Apricus, 2018], b) the absorption of solar radiation (IA) divided into three mechanisms per layer: transmission (τ), absorption (α), and reflection (ρ), c) the heat transfer mechanism from the heat pipe to the working fluid in the manifold, and d) the heat transfer of a number of *N* heat pipes inside the manifold, presenting a heat balance for a node j.

tion film layer (conduction layer). In the condenser, the heat is transported through convection between the hot vapor and the heat pipe wall, a condensation film layer, and the copper layer of the heat pipe to the working fluid in the manifold.

Manifold

In the manifold, the heat from the heat pipe is transferred to the working fluid in the manifold resulting in a temperature increase of this fluid. First this heat is transferred via conduction through the copper layer of the heat pipe holder and secondly via convection transferred to the working fluid. As this working fluid can either be stagnant or flowing, the convection coefficient (h) changes and thereby the convective heat transfer (Q) (equation 3.1.) [Mills, 2014].

$$Q = 2\pi r L\, h\, \Delta T \qquad \textbf{3.1}$$

The convective heat transfer coefficient is dependent on the Nusselt number (Nu) and the conductive heat transfer coefficient (k); this relation is described in equation 3.2. According to [Mills, 2014], the Nusselt Number is a function of the Reynolds number (Re) and the Prandtl number (Pr), Nu = f (Re,Pr). The Reynolds number is a dimensionless number that characterizes the viscous flow and is therefore dependent on the volume flowrate. The Prandtl number is a dimensionless number that characterizes the heat transport in a fluid due to the fluid properties.

$$Nu = \frac{h\,L}{k} \qquad \textbf{3.2}$$

Eventually the total heat gain of a heat pipe *j* is either related to the volume flow and temperature difference over one heat pipe (equation 3.3), or the volume and temperature increment over time over one heat pipe (equation 3.4). This heat gain is dependent on the volume flow rate ($\dot{v}$) or the volume surrounding a heat pipe *j* in the manifold (V_j), the density of the fluid (ρ) and the thermal heat capacity (c_p). The convective heat transfer coefficient effects the maximum temperature difference over one heat pipe.

$$Q_{hp,j} = \dot{v}\rho c_p\left(T_{o,j} - T_{i,j}\right) \qquad \textbf{3.3}$$

$$Q_{hp,j} = V_j \rho c_p \frac{dT}{dt} \qquad \textbf{3.4}$$

The total heat gain of an ETSC is dependent on the number of heat pipes that are connected to the manifold. Figure 3.1d shows a schematic overview of the influence of the number of *N* heat pipes in the manifold on the thermal performance of an ETSC. The heat balance for an average volume flow is described in equation 3.5 and for a stagnant flow in equation 3.6 ($T_{i,1}$ is equal to T_{in} and $T_{o,N}$ equal to T_{out}).

$$Q_{tot} = \sum_{j=1}^{N} Q_{hp,j} = \bar{v}\rho c_p(T_o - T_i) \quad \textbf{3.5}$$

$$Q_{tot} = V\rho c_p \frac{dT}{dt} \quad \textbf{3.6}$$

Dividing the total heat gain with the original heat, obtained from solar radiation, results in the thermal efficiency of an ETSC, presented in Equation 3.7.

$$\eta = \frac{Q_{tot}}{IA} \quad \textbf{3.7}$$

Thermal Network

Figure 3.2 presents the thermal network of one heat pipe from an ETSC, which consists of the three mechanisms described in this paragraph. As can be seen in this figure, the thermal network can be divided into three sections: absorption of solar radiation, heat losses to the environment, and parameters that determine how efficient the heat pipe works (in other words the optical efficiency). This figure also shows that the convective heat transfer between condenser and working fluid in the manifold is part of the optical efficiency of the ETSC. Furthermore, the efficiency of the ETSC, based on the parameters in thermal network, is equal to the overall ETSC efficiency determined by equation 3.7.

Experimental Thermal Performance

Commonly used in processing experimental data is the quadratic form of the Hottel-Whillier-Bliss equation, which is described in equation 3.8 [Duffie & Beckman, 2006]. This equation states that the efficiency of an ETSC is dependent on the *optical efficiency* of the collector (η_0), a *linear heat loss coefficient* (a_1) and a *quadratic heat loss coefficient* (a_2). The optical efficiency characterizes the performance of absorbing solar energy by the solar collector, which is dependent on the materials used in the collector. The optical efficiency can be used to compare the performance of a solar collector under influence of different parameters, such as volume flowrate. The linear heat loss coefficient is the amount of heat lost, mostly through to conduction, due to a temperature increment in the collector compared to the ambient temperature. The quadratic heat loss coefficient is similar to the linear heat loss coefficient; however, most heat is lost due to convection and radiation to the environment.

$$\eta = \eta_0 - a_1\frac{T_M - T_a}{IA} - a_2\frac{T_M - T_a}{IA}|(T_M - T_a)| \quad \textbf{3.8}$$

3.2 Inlet Temperature

Sub-research question 2 was used for determining whether the inlet temperature of the ETSC had an influence on the thermal efficiency of the ETSC. Since the ETSC (used in the experimental research) only had a third of its original capacity due to the limited surface area of the solar simulator, it was unknown if this had any effect on the thermal efficiency; only 10 out of the 30 evacuated tubes were used in the ETSC. This sub-research question was answered with a first set of measurements, which are described in this paragraph. Additionally, this measurement was used for determining the loss coefficients and optical efficiency of the ETSC.

Measurement Method

The measurements were performed using the improved experimental setup (discussed in chapter 2) in combination with the solar simulator. During the measurements, the inlet temperature was varied between 10, 30 and 50 °C. Furthermore,

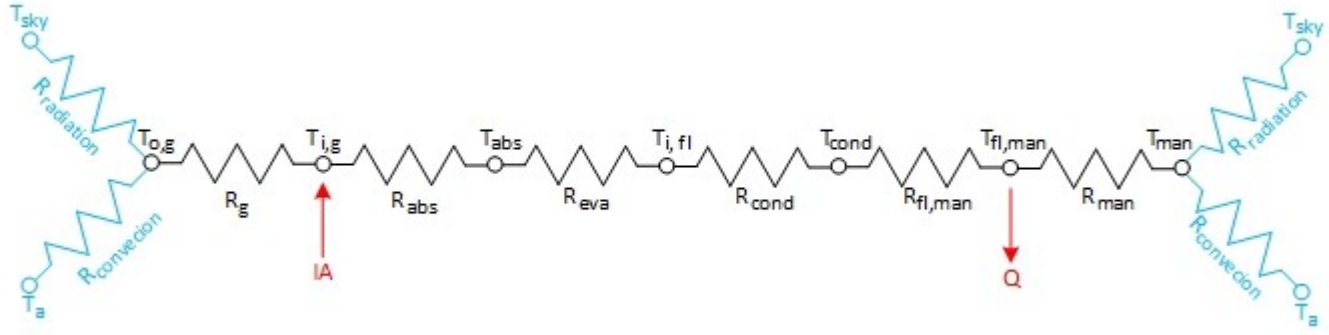

Figure 3.2 — Schematic overview of the thermal network of one heat pipe, divided in the components for three mechanisms: absorption of solar radiation (red), heat losses to the environment (blue), and the conversion of solar radiation into heat (black). The resistance (R) are related to the topics described in this paragraph, where $R_{fl.,man}$ is related to the convective heat transfer between the heat pipe holder and the working fluid in the manifold.

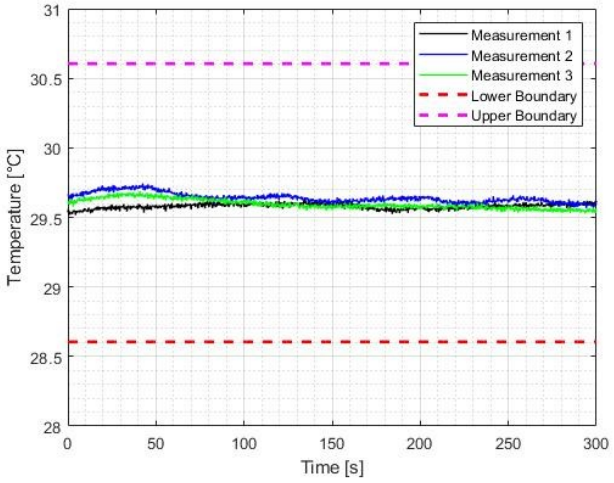

Figure 3.3 — Inlet temperature profiles at the ETSC for three different measurements at a set temperature of 30 °C. It shows that the measurements are well between the minimum and maximum stability boundary conditions for a measurement period of 5 min.

the temperature of the environment was dependent on the temperature fluctuations inside the test facility, and as a result, the temperature of the environment could not be controlled. Additionally, the solar simulator was set on the PV800 solar radiation setting and the volume flowrate through the ETSC had a value of 2 L min^{-1} for each measurement. The solar simulator and ETSC were given time to stabilize the temperature output (approximately 1 hour), which was followed by a measurement period of 5 minutes. Each measurement was repeated three times and will further be referred to as a *measurement group* in this paragraph; a total of 9 measurements were performed.

The total error of each parameter (Z) is dependent on the combined error described in chapter 2, and the standard deviation over the measurement time period. This total error was determined for each parameter using equation 3.9.

$$Z = \sqrt{z_{comb}{}^2 + \sigma_{95\%,m}{}^2} \qquad 3.9$$

Validation

According to [NEN-EN-ISO, 2013], there are guidelines for conducting experiments and comparing experimental data, which are described in chapter 2. One of these guidelines states that the temperature stability of measurements, using the same inlet temperature setting, should be between ±1 °C of the average temperature; in this research, each measurement group should be between these stability boundary conditions. Figure 3.3 presents the inlet temperature profile (at the ETSC) of each individual measurement in a measurement group. Additionally, this figure plots the stability boundary conditions that are based on the average temperature of this measurement group. As can be seen, the three inlet temperature profiles are considerably similar and fairly constant during the measurement period. Moreover, all three profiles are well between the two boundary conditions.

Table 3.1 — Average values, standard deviation and total error of the inlet temperature at the ETSC for each measurement, and the average inlet temperature and boundary condition for each measurement group; all values are in °C.

$T_{in.avg.tot}$	T_{min}	T_{max}	x	$T_{in.avg.x}$	σ_x	Z_x
10.6	9.6	11.6	T_{in_m1}	10.32	0.06	0.14
			T_{in_m2}	10.63	0.05	0.13
			T_{in_m3}	10.94	0.03	0.13
29.6	28.6	30.6	T_{in_m1}	29.58	0.02	0.12
			T_{in_m2}	29.64	0.03	0.13
			T_{in_m3}	29.60	0.04	0.13
48.8	47.8	49.8	T_{in_m1}	48.79	0.03	0.13
			T_{in_m2}	48.88	0.09	0.15
			T_{in_m3}	48.74	0.08	0.15

This example of inlet temperature profiles in one measurement group represents each measurement group, therefore, the results of each measurement group are presented in Table 3.1. Besides the inlet temperature profiles and stability boundary conditions, this table also shows the average temperature of each measurement group and each measurement, and shows the deviation and total error of each measurement. As can be seen, the average temperature combined with its total error was between the stability boundary conditions for each measurement. It can also be noticed from this table, that the average temperature of each measurement group is not similar to the temperature setting of that measurement group. Despite this difference, the data was used for determining the thermal performance, as the focus of the sub -research question is on the difference in thermal performance between different inlet temperature settings.

The maximum allowed deviation is 10% in volume flowrate between two measurement cycles that uses the same volume flowrate. The average volume flowrate during the measurements was 2.01 L min^{-1}, meaning that the measurement boundaries were between 1.81 and 2.21 L min^{-1}. During the measurements, it was observed that the minimum volume flowrate was 1.99 L min^{-1} and the maximum volume flowrate was 2.03 L min^{-1}; as described in chapter 2, the accuracy of the volume flowrate is negligible compared to the measurement value. Based on the inlet temperature data and the volume flowrate data it was concluded that the measurements were performed according to the NEN—EN-ISO 9806 norm.

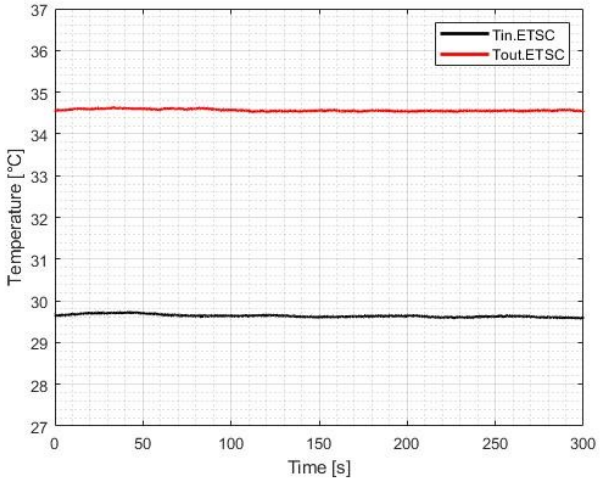

Figure 3.4 — Inlet and outlet temperature profiles at ETSC for a measurement at a set temperature of 30 °C, representing all measurements performed in this research.

Thermal Performance

The thermal performance of the ETSC was determined (for each measurement group) using equation 3.5, which requires the temperature difference over the ETSC. Figure 3.4 plots the inlet and outlet temperature of the ETSC for one measurement. The figure shows that both temperature profiles were stable (relatively small deviation of < 0.07 °C) during the measurement. The data was used to determine both the average temperature profile over the manifold as well as the temperature difference profile between inlet and outlet. The average values of these profiles were used for determining the thermal performance of the ETSC. Figure 3.4 represents the inlet and outlet temperature profiles of each measurement.

For the thermal performance, it was assumed that the water inside the ETSC had a density of 1,000 kg m^{-3} and a thermal capacity of 4,190 J $kg^{-1}K^{-1}$. The solar radiation and the ambient temperature were observed during the measurements, which are presented in Table 3.2. Furthermore, this table presents the average temperature difference, mean temperature over the manifold, volume flowrate and thermal efficiency (equation 3.7) for each measurement group; these values are the average values of each individual measurement in a measurement group. As can be seen, the thermal efficiency is higher for a lower inlet temperature than for a higher inlet temperature that can be explained with the difference between the mean temperature over the manifold and the ambient temperature. The mean temperature over the manifold is less than the ambient temperature when using an inlet temperature of approximately 10 °C, resulting in heat gain instead of heat losses due to the environment. An inlet temperature of approximately 50 °C results in a higher mean temperature than the ambient temperature, resulting in heat losses. Finally, it can be seen that the total error in thermal efficiency is approximately 0.01.

Table 3.2 — Overview of the average values and total error of the inlet temperature experiment, based on three measurements, for the: intensity (I), volume flowrate ($\dot{v}$), ambient temperature (T_a), temperature difference over manifold (ΔT), mean temperature over the manifold (T_M), and the thermal efficiency (η)

		T_{in} = 10 °C		T_{in} = 30 °C		T_{in} = 50 °C	
x		$\bar{x}$	Z_x	$\bar{x}$	Z_x	$\bar{x}$	Z_x
I	[W m^{-2}]	1001	5.30	1001	4.90	1002	6.60
$\dot{v}$	[L min^{-1}]	2.03	0.00	1.99	0.00	2.01	0.00
T_a	[°C]	31.72	0.47	28.69	0.67	29.10	0.55
ΔT	[°C]	5.10	0.06	4.92	0.07	4.63	0.07
T_M	[°C]	13.18	0.10	32.07	0.07	51.12	0.11
η	[-]	0.78	0.01	0.74	0.01	0.70	0.01

Optical Efficiency

Another aspect of this sub-question was to determine the optical efficiency and the linear and quadratic heat loss coefficients. Figure 3.5 plots the thermal efficiency as a function of the difference between the mean temperature over the manifold and the ambient temperature; a secondary polynomial trend line represents the Hottel-Whillier-Bliss equation (equation 3.8). In this equation there are three unknown parameters, the optical efficiency and both heat loss coefficients, and due to the three measurement groups there are three equations (equation 3.10—3.12). In these equations the factor *x* represents (T_M-T_a) and y the product of intensity and surface area (IA).

$$\eta_1 = \eta_0 - a_1\frac{x_1}{y_1} - a_2\frac{x_1}{y_1}|x_1| \quad \textbf{3.10}$$

$$\eta_2 = \eta_0 - a_1\frac{x_2}{y_2} - a_2\frac{x_2}{y_2}|x_2| \quad \textbf{3.11}$$

$$\eta_3 = \eta_0 - a_1\frac{x_3}{y_3} - a_2\frac{x_3}{y_3}|x_3| \quad \textbf{3.12}$$

These three equations were used to determine the optical efficiency and the heat loss coefficients, shown in Table 3.3; the computation is described in appendix B.1. Table 3.3 also shows the optical efficiency and heat loss coefficients determined by the SP Technical Institute of Sweden (Appendix B.2). As can be seen, there is a difference in optical efficiency and heat loss coefficients, which can either be related to the difference in volume flowrate or to the difference in evacuated tubes available in the ETSC. However, for this thesis it was

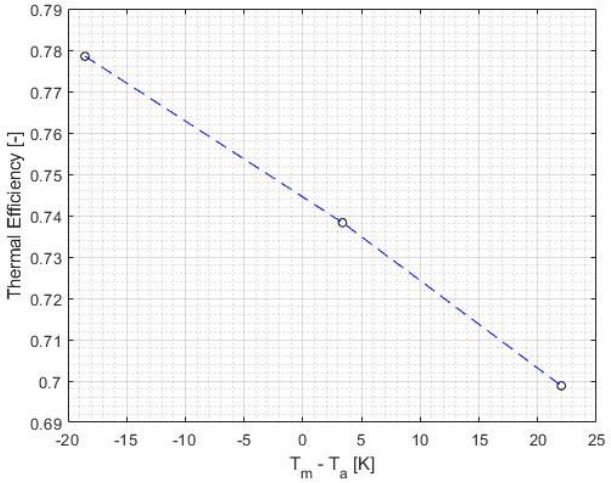

Figure 3.5 — The thermal efficiency versus the difference between the mean temperature over the manifold and the ambient temperature. The second order polynomial represents the thermal efficiency curve based on the Hottel-Whillier-Bliss equation and the measurement data.

assumed that the heat loss coefficients do not depend on the volume flowrate. As a result, the heat loss coefficients found in this experiment were used for processing the data found in other experiments.

3.3 Solar Radiation Level

Another sub-research question was formulated in order to investigate the influence of the solar radiation on the thermal performance of an ETSC. According to the theoretical model, the radiation influences the total heat (IA) and the temperature difference over the manifold (absorbed radiation in the evacuated tube). This set of measurements were used to conduct research on the behavior of the optical efficiency under influence of different solar radiation levels.

Measurement Method

Similar to the measurements of paragraph 3.2, the measurements were performed using the improved experimental setup and the solar simulator. The solar simulator has four different solar radiation settings, categorized in photovoltaic (PV) and solar thermal (ST): PV200, PV800, PV1000, and ST1000. During the measurements, the PV200, PV800 and PV1000 settings were used as they use the same solar spectrum at different radiation rates, while the ST1000 setting uses a different solar spectrum [Eternal Sun B.V., 2015]. Furthermore, the temperature of the environment was set to be variable for the same reason as discussed in paragraph 3.2. For these measurements, the inlet temperature was fixed on 30 °C and a volume flowrate of 2.0 L min^{-1} was used. Identical to the previous measurements, after the solar simulator and ETSC reached a stabilized a measurement was performed over a time period of 5 min. Each measurement was also repeated three times and will further be referred to as a *measurement group* in this paragraph.

Table 3.3 — The optical efficiency and heat loss coefficients (a_1 and a_2) from this experiment and found in the Solar Keymark (Appendix B.2). The experiment results were found and a volume flowrate of 2.0 L min^{-1}, while the Solar Keymark uses a volume flowrate of approximately 3.3 L min^{-1}

Parameter		Experiment	Solar Keymark
η_0	[-]	0.743	0.761
a_1	[W $m^{-2}K^{-1}$]	1.236	2.299
a_2	[W $m^{-2}K^{-2}$]	0.029	0.010

Validation

For this set of measurements, a validation was required in order to verify that the measurements were performed according to the guidelines set in chapter 2. As the average temperature of all measurements was 29.51 °C, the temperature boundary was between 28.51 and 30.51 °C. The minimum value observed in the measurements had a value of 29.24 °C, while the maximum value was 29.65 °C; both with a maximum total error of 0.13 °C. The average volume flowrate was 2.00 L min^{-1}, resulting in the maximum boundaries of 1.80 and 2.20 L min^{-1}. During the measurements, the minimum volume flowrate was 1.99 L min^{-1} and the maximum volume flowrate was 2.01 L min^{-1}. Based on these data it was concluded that the measurements were performed according to the NEN-EN-ISO 9806 norm.

Since the solar simulator operates with radiation settings (in case of this set of measurements PV200, PV800 and PV1000), the emitted radiation rates were determined using a pyranometer. Figure 3.6 presents the radiation level for each solar simulator setting per measurement. As can be seen in this figure, there is an insignificantly small difference in radiation level between the measurements in each measurement group. Also, the radiation level was 365 W m^{-2} rather than 200 W m^{-2} while using the PV200 setting; similar results were obtained for the PV800 and PV1000 setting. This difference in radiation rate could be related to a spectral mismatch between the output of the solar simulator and the distance between the simulator and the ETSC [Eternal Sun B.V., 2018]; however, this difference was unimportant, since the solar radiation rates were measured and used in the data analysis.

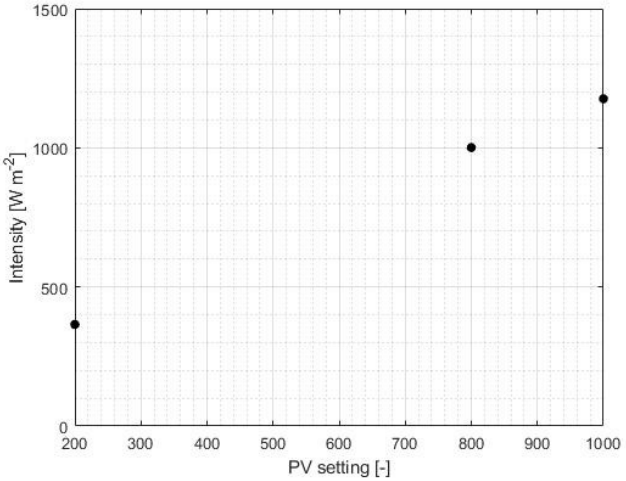

Figure 3.6 — The relation between the solar simulator setting and the radiation level measured by a pyranometer.

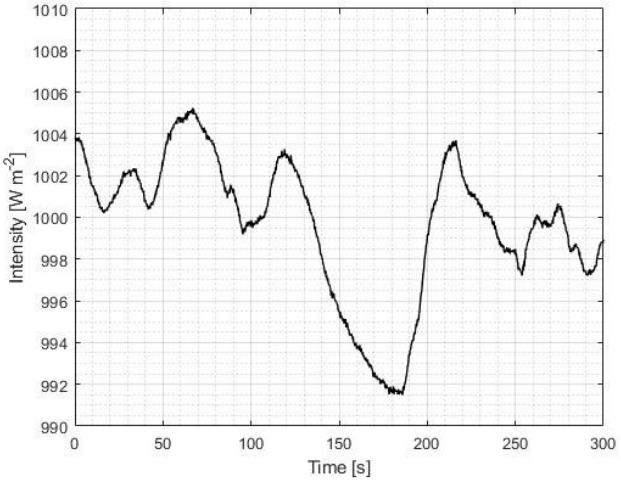

Figure 3.7 — Radiation output profile of the solar simulator (PV800) measured with a pyranometer.

The radiation profile of a measurement using the PV800 setting is plotted in Figure 3.7. This figure shows that the radiation output of the solar simulator is not consistent, which could have an influence on the thermal performance. However, the average value of the radiation profile for each measurement was used as the average solar radiation is required for data analysis (equation 3.5 – 3.8). Therefore, it was assumed for data processing that the average radiation level was a good approximation for the thermal performance of the ETSC.

Optical Efficiency

The thermal efficiency, for each measurement group, was determined using a similar approach as discussed in paragraph 3.2. Also, the inlet and outlet temperature of the ETSC were comparable to Figure 3.4, resulting in obtaining constant temperature profiles during each measurement. This data was used to acquire the average temperature over the manifold and the average temperature difference between the inlet and outlet of the ETSC, which are presented in Table 3.4. This table also shows the average solar radiation level, the average ambient temperature, and the average volume flowrate for each measurement group. The thermal efficiency was determined using equation 3.5 and 3.6, combined with the assumptions made in paragraph 3.2 regarding the density and thermal capacity of water.

The optical efficiency was determined using the heat loss coefficients from the first set of measurements (paragraph 3.1) combined with the thermal efficiency from these measurements; the results are shown in Table 3.4. It can be seen from this table that the optical efficiency decreases when the solar radiation decreases, which might be related to the inaccuracy in solar radiation. However, according to [Liu, 2015] the efficiency of a solar collector decreases with decreasing solar radiation level. Thus, it could be that the optical efficiency slightly changes when the solar radiation level changes.

3.4 Volume Flowrate

The last sub-research question is related to the main research question of this experimental research, namely to investigate the influence of volume flow on the thermal performance of the ETSC. This sub-research question was divided into two sets of measurements: (i) using different continuous volume flowrates, and (ii) start-stop measurements. The first section describes the first set of measurements, while the second section describes the second set of measurements. Both set of measurements are compared to one another in a third section. During the measurements, the improved experimental setup (chapter 2) was used in combination with the solar simulator.

3.4.1 Constant Volume Flowrate

As described in the theoretical model, the volume flowrate has an influence on both the convective heat transfer between the working fluid inside the manifold and the heat pipe holder, thus on the thermal efficiency. Therefore, this set of measurements was used for conduction research on the influence of different constant volume flowrates on the optical efficiency of the ETSC.

Measurement Method

In this set of measurements there were two variables, one of these variables was the ambient temperature (paragraph 3.2) and the other variable was the volume flowrate, which was varied between 0.2, 0.5, 1.0, 1.5, 2.0 and 5.0 L min^{-1}. Furthermore, a constant solar radiation level was achieved by using the PV200 setting on the solar simulator, and a temperature

Table 3.4 — Overview of the average values and total error of the radiation level experiment, based on three measurements, for the: intensity (I), volume flowrate ($\dot{v}$), ambient temperature (T_a), temperature difference over manifold (ΔT), mean temperature over the manifold (T_M), the thermal efficiency (η), and the optical efficiency (η_0)

		PV200		PV800		PV1000	
x		$\bar{x}$	Z_x	$\bar{x}$	Z_x	$\bar{x}$	Z_x
I	[W m^{-2}]	365	3.10	1001	4.90	1176	4.00
$\dot{v}$	[L min^{-1}]	2.00	0.00	1.99	0.00	2.00	0.00
T_a	[°C]	28.74	0.21	28.69	0.67	32.92	0.73
ΔT	[°C]	1.76	0.08	4.92	0.07	5.82	0.07
T_M	[°C]	30.20	0.06	32.07	0.07	32.52	0.05
η	[-]	0.73	0.01	0.74	0.01	0.74	0.01
η_0	[-]	0.72	0.01	0.73	0.01	0.75	0.01

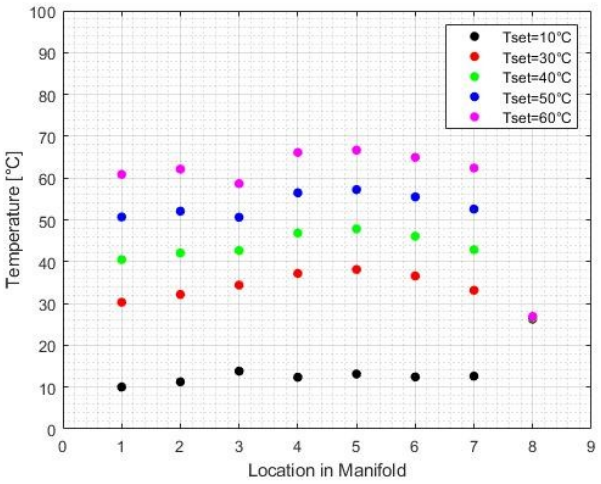

Figure 3.8 — Temperature profile inside the manifold under influence of radiation (PV200 setting). The x-axis represents the location in the manifold, in example: number 1 is TC1.

Table 3.5 — Average values and total error of the volume flowrate through the ETSC for each measurement, and the average volume flowrate and boundary condition for each measurement group; all values are in L min^{-1}.

$\dot{v}_{in.avg.tot}$	$\dot{v}_{min}$	$\dot{v}_{max}$	x	$\dot{v}_{in.avg.x}$	Z_x ($\times 10^{-3}$)	$\dot{v}_{in.avg.tot}$	$\dot{v}_{min}$	$\dot{v}_{max}$	x	$\dot{v}_{in.avg.x}$	Z_x ($\times 10^{-3}$)
			$\dot{V}_{in\_m1}$	0.20	1.32				$\dot{V}_{in\_m1}$	1.50	1.56
0.2	0.18	0.22	$\dot{V}_{in\_m2}$	0.20	1.34	1.50	1.35	1.65	$\dot{V}_{in\_m2}$	1.50	0.87
			$\dot{V}_{in\_m3}$	0.20	1.96				$\dot{V}_{in\_m3}$	1.50	1.58
			$\dot{V}_{in\_m1}$	0.50	1.20				$\dot{V}_{in\_m1}$	2.00	1.14
0.50	0.45	0.55	$\dot{V}_{in\_m2}$	0.50	1.02	2.00	1.80	2.20	$\dot{V}_{in\_m2}$	2.00	1.56
			$\dot{V}_{in\_m3}$	0.50	0.74				$\dot{V}_{in\_m3}$	2.00	1.74
			$\dot{V}_{in\_m1}$	1.01	1.48				$\dot{V}_{in\_m1}$	5.07	5.97
1.01	0.91	1.11	$\dot{V}_{in\_m2}$	1.01	0.63	5.08	4.57	5.59	$\dot{V}_{in\_m2}$	5.08	5.93
			$\dot{V}_{in\_m3}$	1.01	0.94				$\dot{V}_{in\_m3}$	5.09	3.99

Table 3.6 — Overview of the average values and total error of the constant volume flow experiment, based on three measurements, for the: intensity (I), volume flowrate ($\dot{v}$), ambient temperature (T_a), temperature difference over manifold (ΔT), mean temperature over the manifold (T_M), the thermal efficiency (η), and the optical efficiency (η_0)

		0.2		0.5		1.0		1.5		2.0		5.0	
x		$\bar{x}$	Z_x	$\bar{x}$	Z_x	$\bar{x}$	Z_x	$\bar{x}$	Z_x	$\bar{x}$	Z_x	$\bar{x}$	Z_x
I	[W m^{-2}]	365	2.9	365	3.1	365	3.3	365	6.9	370	3.1	363	3.1
T_a	[°C]	24.69	0.22	27.70	0.52	27.68	0.56	28.29	0.35	28.74	0.21	29.29	0.21
ΔT	[°C]	15.40	0.09	6.53	0.11	3.38	0.07	2.29	0.06	1.76	0.07	0.69	0.05
T_M	[°C]	36.48	0.06	32.64	0.06	31.06	0.08	30.59	0.05	30.20	0.06	29.73	0.05
η	[-]	0.68	0.01	0.72	0.01	0.73	0.01	0.74	0.01	0.75	0.01	0.76	0.02
η_0	[-]	0.68	0.01	0.70	0.01	0.72	0.01	0.72	0.01	0.72	0.01	0.72	0.02

of 30 °C was used at the inlet of the ETSC. Similar to previous sets of measurements, after the solar simulator and ETSC reached a stabilized outlet temperature, a measurement was performed over a period of 5 minutes. This process was repeated three times per measurement (further referred to as a *measurement group*).

Validation

For this set of measurements, a analysis was required in order to verify that the measurements were performed according to the guidelines set in chapter 2. Since the average temperature of all measurements was 29.28 °C, the temperature boundaries were 28.28 and 30.28 °C according to the NEN-EN -ISO 9806 norm. During the measurements, the minimum temperature was 28.75 °C and the maximum temperature was 29.46 °C with a maximum total error of 0.13 °C. Therefore, the inlet temperatures at the ETSC were between the temperature boundaries and it was concluded that the temperature measurements were performed according to the NEN-EN-ISO 9806 norm.

Table 3.5 presents the average volume flowrate and the minimum and maximum volume flowrate according to the NEN-EN-ISO 9806 guidelines for each measurement group. Additionally, this table presents the average volume flowrate and total error of each individual measurement. As can be seen, the volume flowrates of each measurement are relatively similar to the average volume flowrate, and as a result were between the minimum and maximum values. Thus, it was concluded that the measurements were performed according to the guidelines.

Optical Efficiency

The thermal efficiency for each measurement group was obtained using a similar approach as discussed in paragraph 3.2, also, a similar result was observed for the inlet and outlet temperature as shown in Figure 3.4. Furthermore, the optical efficiency was determined using equation 3.8 in combination with the heat loss coefficients found in the first set of measurements (paragraph 3.2). Table 3.6 presents the average values for the temperature difference over the inlet and outlet of the ETSC, the mean temperature over the manifold, solar radiation level, the thermal efficiency and the optical efficiency. This table shows that the optical efficiency decreases with a decrease in volume flowrate, which could be related to the lower convective heat transfer rate at lower volume flowrates.

3.4.2 Start Stop Mechanism

In contrast to using a continuous flow, the temperature output cannot be measured while using only a stagnant flow. Therefore, a second set of measurements was required in order to find the influence of a start-stop mechanism on the thermal performance of an ETSC.

Measurement Method

Each measurement consisted of two parts (called a *cycle*), the stagnant flow time period (stagnant period) and the continuous flow time period (volume flow period). During the stagnant period, the working fluid in the manifold was heated under influence of solar radiation emitted by the solar simulator; the PV200 setting was used. Also, the temperature was approximately 30 °C at the inlet of the ETSC for each start of the measurement. Furthermore, three different stagnant periods were used, namely 2, 5 and 10 minutes; a stagnant period of 10 minutes is common among solar collector start stop operation mechanism. In the volume flow period, a volume flowrate of 5.0 L min^{-1} was used for transporting the working fluid inside the manifold to the outlet of the ETSC, to acquire an outlet temperature profile. This cycle of two periods was repeated four times for each measurement (referred to as *measurement group*), from which the first cycle was intended for stabilizing the temperature increase in the ETSC.

Temperature Profile

During the measurements, the temperature was measured at eight different locations throughout the manifold, which are plotted in Figure 3.8; an overview of the thermocouple locations is shown in chapter 2. As can be seen in this figure, there were 2 thermocouples that showed deviant temperature profiles: thermocouple 3 (TC3) and especially thermocouple 8 (TC8), where TC8 showed a constant temperature profile that was similar to the temperature of the environment. Therefore, it was concluded that these thermocouples were incorrectly installed or shifted during the installation of the insulation layer and were neglected in the analysis. Also, it can be seen that the temperatures in the middle of the manifold (TC4 and TC5) were higher than at the side (TC1) thereby creating a parabolic temperature distribution over the length of the manifold. The reason for this phenomenon is that heat is lost at the side of the ETSC due to the fluid inside the connections towards the ETSC.

Optical Efficiency

Due to the volume flow period of the measurement, the temperature profile inside the manifold is transported to the outlet of the ETSC. Figure 3.9 plots the temperature profile observed at the outlet of the ETSC for one cycle and shows that there is a clear distinction between the stagnant period and the volume flow period. The peak in this temperature profile represents the heat absorbed during the first time period inside the manifold. The figure also plots the initial temperature (T_0) of the measurement, and it can also be seen that the outlet temperature decreases during the stagnant period due to heat losses.

The temperature difference between this peak and the initial temperature was multiplied with the volume flowrate profile, density of the fluid, and the thermal capacity of the fluid, to acquire the absorbed heat profile, which is presented in Figure 3.10; the density and thermal capacity were assumed to be constant (paragraph 3.1). Integration of this profile results in the absorbed energy (E_{tot}) during the stagnant time period, which is shown in Table 3.7 for each measurement group. Consequently, this total amount of energy was divided by the total time of one cycle to obtain the average heat absorption (Q_{avg}). It has to be noted that the volume flow period is the time needed for the entire volume inside the manifold to pass the outlet of the ETSC, while in reality this is a fixed value (for example 2 minutes). Therefore, this measurement determines the maximum value for the average heat absorption, which in reality would be lower.

Determining the average thermal efficiency was based on a similar method as described in paragraph 3.2, which was used to determine the optical efficiency based on the heat loss coefficients found in the first set of measurements; both efficiencies can be found in Table 3.7. Also, the average volume flowrates are shown in this table that were based on the volume flow profile, acquired during the volume flow period, and the total cycle time, resulting in low volume flowrates. From the data in this table, it seems that there is an optimal stagnant period for acquiring the optimal optical efficiency.

3.4.3 Comparison

The optical efficiencies are plotted versus their volume flowrate using both set of measurements, which are shown in Figure 3.11. From this figure it can clearly be seen that there is a slight decrease in optical efficiency for using different volume flowrates. Additionally, it highlights that there might be an optimal stagnant period for acquiring an optimum optical efficiency while using a start stop mechanism. Also, from this figure it seems that using a continuous volume flowrate will result in a higher optical efficiency than using a start stop mechanism. It could be that using a stagnant flow will result in an even lower convective heat transfer rate between the heat pipe holder and the working fluid in the manifold. Unfortunately, the geometry of the manifold does not allow for theoretical determination of the convective heat transfer coefficient, which means that more conclusive research is required to verify this hypothesis. Moreover, the difference between stagnant flow and continuous volume flowrate could also be related to heat losses to adjacent fluid volumes (parabolic temperature profile inside the manifold), which results in lower heat absorption rates.

It has to be noted that in reality the solar radiation changes during the day, which might lead to a quick change in operation mechanism in the CV-system from start-stop operation to continuous operation. Since a stagnant flow results in a higher outlet temperature, compared to a continuous flow using the same inlet temperature, it could be that warm water is transported to the storage tank sooner (due to the TDV) while using a start-stop mechanism. When the start-stop mechanism is used for a short period of time, it could be that this mechanism is more beneficial than a continuous volume flowrate, despite its lower optical efficiency.

3.5 Sensitivity Analysis

A sensitivity analysis was conducted in order to characterize the accuracy in which the optical efficiency was determined. This sensitivity analysis was divided into three topics: (i) the influence of several important parameters on the optical efficiency, (ii) the assumption of constant heat loss coefficients, and (iii) the influence of value decision of several parameters during the start stop data analysis.

Parameter Influence

Several experimentally determined parameters were used in the determination of the optical efficiency in this experimental research. Therefore, research was conducted on finding the absolute error of these parameters using three different scenarios. The absolute error is defined, in this section, as the absolute deviation of a parameter in order to increase the optical efficiency with 0.01. The first scenario uses a solar radiation level of 1000 W m^{-2}, an inlet temperature of 30 °C at the ETSC, and a volume flowrate of 2.0 L min^{-1}. This results in a temperature difference over the manifold of approximately 5 °C and an optical efficiency of 0.76 (according to the measurement data). In a second scenario, the solar radiation level was decreased to 365 W m^{-2}, thereby decreasing the temperature difference to around 1.76 °C and the optical efficiency to 0.73. A third scenario also decreases the volume flow to 0.2 L min^{-1}, which resulted in a temperature difference of approximately 15.4 °C and an optical efficiency of 0.70.

Table 3.8 presents the absolute error for each parameter that was used in the optical efficiency calculation and highlights the absolute errors that were less than the total error of the measurements. As can be seen, the radiation level has the highest influence on the optical efficiency during this experimental research, since most measurements were performed using the PV200 setting. Though, the absolute error is relatively close to the total error of the measurements. Additionally, the temperature difference had a higher total error during the measurements than the absolute error in scenario 2. All other parameters had significantly smaller total errors during the measurements than the absolute errors, thus it can be concluded that the maximum deviation in optical efficiency was related to the solar radiation level.

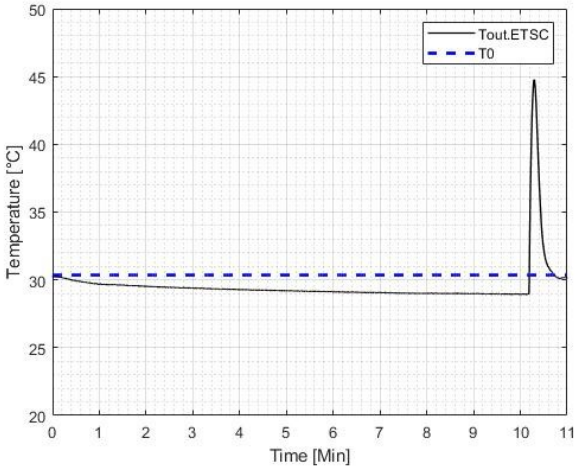

Figure 3.9 — Temperature profile measured at the outlet of the ETSC. Furthermore, the temperature at the start of the measurement (T_0) is plotted.

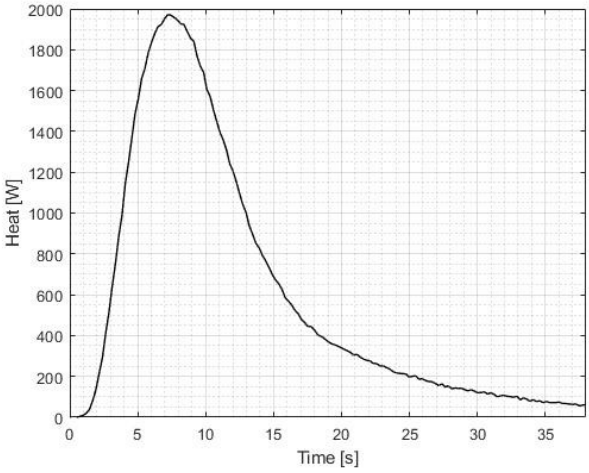

Figure 3.10 — Heat profile acquired during the volume flow period of a measurement. This profile is based on the temperature profile, volume flow profile, and the properties of water. Integration of this profile results in the energy absorbed during the stagnant period inside the manifold.

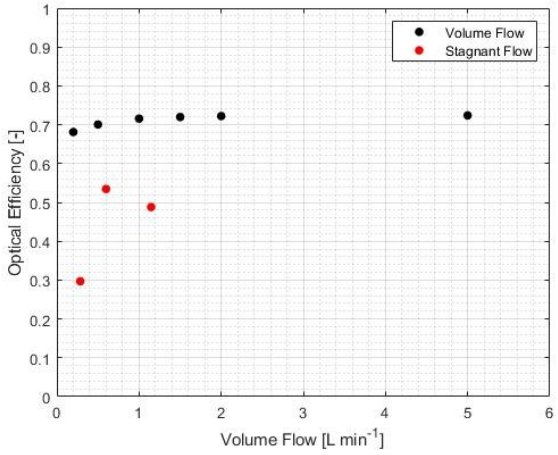

Figure 3.11 — The optical efficiencies of both the constant volume flow and start stop (stagnant) measurements.

Table 3.7 — Overview of the average values and total error of the start stop experiment, based on three measurements, for the: stagnant period (t_{stag}), volume flow period (t_{vf}), volume flowrate during the peak ($\dot{v}_{peak}$) and averaged over the cycle ($\dot{v}_{avg}$), absorbed energy (E_{tot}), average heat over one cycle (Q_{avg}), efficiency (η), and the optical efficiency (η_0).

		2 minutes		5 minutes		10 minutes	
x		$\bar{x}$	Z_x	$\bar{x}$	Z_x	$\bar{x}$	Z_x
t_{stag}	[s]	120		120		120	
t_{vf}	[s]	38.2		38.2		38.2	
$\dot{v}_{peak}$	[L min^{-1}]	4.75	0.00	4.73	0.00	4.75	0.00
$\dot{v}_{avg}$	[L min^{-1}]	1.15	0.00	0.53	0.00	0.28	0.00
E_{tot}	[kJ]	23	0.97	53	2.37	89	3.77
Q_{avg}	[W]	145	6.14	157	7.01	139	4.98
η	[-]	0.43	0.02	0.46	0.02	0.39	0.02
η_0	[-]	0.46	0.02	0.53	0.02	0.37	0.01

Table 3.8 — Absolute errors that result in an increase of 0.01 in optical efficiency, defined per parameter. The highlighted areas indicate a higher total error (measurements) than an absolute error.

Parameter		Scenario 1	Scenario 2	Scenario 3
I	[W m^{-2}]	14.00	5.11	5.11
$\dot{v}$	[L min^{-1}]	0.03	0.03	0.00
T_a	[°C]	4.93	1.74	1.73
ΔT	[°C]	0.07	0.02	0.20
T_M	[°C]	0.21	0.20	0.24

Table 3.9 — The optical efficiency and loss coefficients found during measurements at different volume flowrates

Parameter		0.2 L min^{-1}	1.0 L min^{-1}	2.0 L min^{-1}
η_0	[-]	0.692	0.714	0.722
a_1	[W m^{-2}K^{-1}]	1.306	0.149	1.236
a_2	[W m^{-2}K^{-2}]	-0.035	0.122	0.029

Table 3.10 — Heat loss coefficient terms under influence of the mean temperature over the manifold. The values have to be multiplied with x 10^{-2}.

Coefficient term	T_M=30 °C	T_M=40 °C	T_M=50 °C
Linear heat loss	0.73	4.37	8.01
Quadratic heat loss	0.03	1.23	4.13

Heat Loss Coefficients

One of the major assumptions in this experimental research was that the heat loss coefficients were assumed to be constant. These heat loss coefficients were based on three measurement groups, which is the precise number of datapoints needed to determine these coefficients. Thus, a slight deviation in thermal efficiency could have an enormous influence on this determination, which could be solved by acquiring more datapoints. Unfortunately, the number of measurements was restricted in this master thesis.

In paragraph 3.2 it was stated that a difference in the heat loss coefficients between the measurement and the Solar Keymark values could be related to the difference in volume flowrate. Therefore, a similar research was conducted as described in paragraph 3.2 for a volume flowrate of 0.2 and 1.0 L min^{-1}. Table 3.9 presents the optical efficiency and heat loss coefficients that were found in this research, and as can be seen, there is a difference between these coefficients. However, the optical efficiency found in this research was relatively similar to the results found in paragraph 3.4, namely 0.692 instead of 0.681 (0.2 L min^{-1}) and 0.714 instead of 0.716 (1.0 L min^{-1}). As a result, it was concluded that despite the difference in heat loss coefficients, the results found in this experimental research are representable for the analysis of the thermal performance of an ETSC.

Influence Parameters in Stagnant Measurement

Several parameters were used in the process of determining the optical efficiency, which had to be chosen based on experimental data and/or estimated. This sensitivity analysis describes and discuses three important parameters: (i) the mean temperature over the manifold, (ii) the initial temperature, and (iii) the radiation during the volume flow period.

The mean temperature over the manifold varies during the stagnant period as the temperature inside the collector increases due to radiation emitted by the solar simulator. According to paragraph 3.2, the heat loss coefficients are constant over the difference between the mean temperature over the manifold and the ambient temperature. As a result, the heat loss coefficient terms changes over time in the Hottel-Whillier-Bliss equation. Additionally, this equation also uses the thermal efficiency, which in this experimental research was based on the average heat absorption rate (paragraph 3.4).

Table 3.10 shows the difference in heat loss coefficients terms when the mean temperature over the manifold varies between 30, 40 and 50 °C; these values represent the temperature data found in the measurement. As can be seen in this table, the mean temperature over the manifold has an enormous effect on the heat loss coefficient terms; the linear coefficient term varies between 0.007 and 0.08, while the quadratic coefficient term varies between almost 0 and 0.04. Since the optical efficiency is a function of the thermal efficiency and both these coefficient terms (equation 3.8), the optical efficiency has even higher deviations when using different mean temperatures over the manifold. Therefore, it can be concluded that this parameter has a great impact on the data processing discussed in paragraph 3.4, which uses a constant value for this parameter.

Another parameter is the initial temperature that influences the determination of energy absorbed in the stagnant period. This parameter had a value based on the starting values for both the inlet and outlet temperature at the ETSC. However, a change in this value directly influences the temperature difference obtained with the peak profile and as a result the total absorbed energy changes. Consequently, the average heat absorption rate changes and with it the thermal efficiency and optical efficiency. Nonetheless, only a small fraction of energy is either added or extracted due to this difference in value that will minimize the influence on the average heat absorption rate, thus the values obtained in paragraph 3.4 most likely will represent the energy absorption using a start stop mechanism. A more conclusive research is needed in order to verify the negligible effect of initial temperature on the heat absorption rate.

Finally, during the volume flow period there was still solar radiation available due to the solar simulator. Unfortunately, the solar simulator could not be turned off during the volume flow period as the start-up time of this simulator is at least 15 minutes, which resulted in an incorrect radiation profile during the stagnant period of the next cycle. As a volume flowrate of 5.0 L min^{-1} was used, the influence of the solar radiation on the temperature output profile was minimized. Paragraph 3.4 shows that the temperature difference was 0.69 °C between the inlet and outlet of the ETSC using a volume flowrate of 5.0 L min^{-1}, while the maximum temperature difference during the stagnant period was 15 °C. Therefore, it was concluded that the influence of a continuous solar radiation is negligible.

Part 2 — Numerical Research

4| System Layout

The secondary part of this master thesis was to investigate the possibility of simulating the CV system in TRNSYS18. TRNSYS18 is a software package that is able to simulate transient behavior of a system, for instance a solar combisystem, using individual component models, such as pumps, pipes and solar collectors; these components are called types [TRNSYS, Volume 1, 2017]. Each type is described by a series of equations to determine the desired output. The TRNSYS software package includes a library of types that can be expanded by (i) extra paid libraries provided by TRNSYS, for example the TESS library, or (ii) by creating a type in the Fortran environment. In TRNSYS, the types used in a system are connected to each other using the output of one type to another type or multiple types; the program is able to connect components in a closed loop. TRNSYS calculates the types in order of appearance in the input file for each simulation time step.

During the numerical research, only one simulation model was developed: the CV-system (Chapter 1). Figure 4.1 presents a schematic overview of this system and shows the types that were used in TRNSYS18 for simulating this system. Additionally, the figure also indicates at which location the temperatures and mass flowrates (ṁ) were determined. As can be seen, the CV simulation model only consists of a heat generation profile and neglects the energy demand profiles of possible inhabitants that uses this system. The heat generation profile consists of the ETSC, pipes, a pump, the TDV, and a thermal storage tank.

This chapter firstly describes each of these components used in the simulation model with their design parameters, in which most of these parameters were based on the reference model from TASK54, described in Appendix C.1. The numerical models from each of these components are briefly discussed, while detailed models can be found in the documentation of TRNSYS. Subsequently, a numerical analysis research was conducted for several components in order to verify that the output of the component was realistic.

4.1 System Components

For some of the components, used in the CV model, there were multiple types that could be used for the simulation due to the standard library and TESS library of TRNSYS18. In this section, a brief explanation of each component is given combined with the design parameters required by TRNSYS.

4.1.1 Evacuated Tube Solar Collector

The reference model from TASK54 used a flat plate solar collector, which was simulated with TRNSYS-type132. Unfortunately, there was no documentation available of this TRNSYS-type component, thus it was unclear how this component computes the simulation and whether this component could be used for simulating an ETSC. There are several other TRNSYS-types in the standard library and extended TESS library that can be used for simulating a solar collector; however, TRNSYS-type538 was used as it is the most suitable for simulating an ETSC. This type models an ETSC or any other collector that uses a linear or quadratic efficiency curve and uses incidence angle modifiers (IAMs) to account for off-normal radiation effects. Also, this model is capable of including the capacitance (mass) of the collector [Tess, Volume 10, 2012].

Numerical Model

The numerical model of the TRNSYS simulation is similar to the theoretical model described in Chapter 3. In the numerical model, there are four different factors that influence the thermal performance of the ETSC. The first factor is related to the energy stored in the working fluid inside the manifold when there is a stagnant flow ($Q_{sto,j}$), which is described in equation 3.3 for a number of *N* heat pipes. Another factor is the energy transferred to the working fluid under influence of a volume flowrate ($Q_{fl,j}$), which is described in equation 3.4 for a number of *N* heat pipes. It has to be noted that the TRNSYS model does not use a number of *N* heat pipes but a number of *j* nodes. Furthermore, the numerical model accounts for the solar irradiation ($Q_{solar,j}$) and the heat losses ($Q_{lost,j}$), resulting in expression 4.1. The heat losses of the ETSC are in

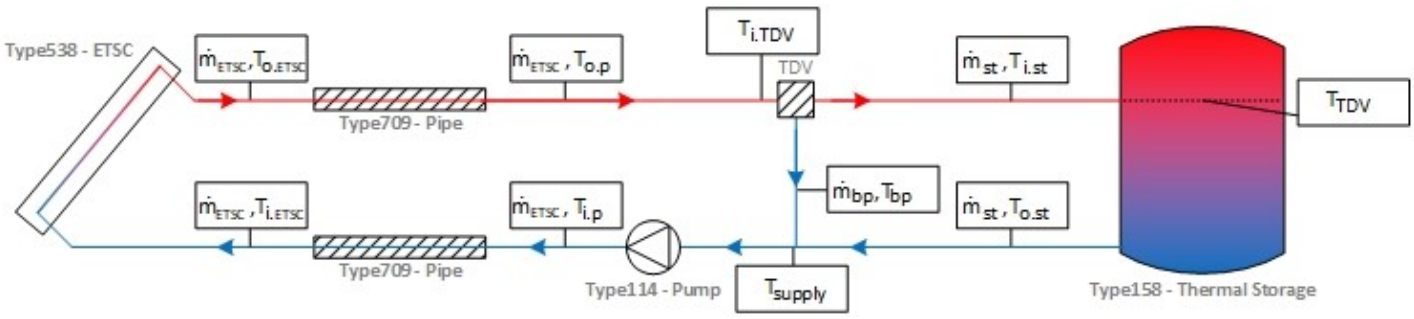

Figure 4.1 — Schematic overview of the CV-system showing the types used in TRNSYS. Furthermore, it shows an overview of the temperature and mass flow datapoints used in the verification and system modeling.

the numerical model also dependent on the linear loss coefficient and quadratic loss coefficient as described in Chapter 3.

$$Q_{sto,j} + Q_{fl,j} = Q_{solar,j} + Q_{lost,j} \quad \textbf{4.1}$$

The heat from solar irradiation in the numerical model, equation 4.2, incorporates the efficiency of the ETSC using the collector fin efficiency (F') and the transmission and absorption coefficients at normal solar incidence $(\tau\alpha)_n$, and also accounts for the incident angle modifier (IAM); therefore, it differs from the theoretical model from Chapter 3. Expression 4.3 is used in the numerical model that is based on all these individual heat balances.

$$Q_{solar,j} = F'(\tau\alpha)_n \, IAM \, IA = F'S \quad \textbf{4.2}$$

System Parameters

TRNSYS-type538 requires the ETSC specifications used in the CV-system, which are described in the Solar Keymark (Appendix B.2). As the numerical research was conducted simultaneously with the experimental research, the data provided in chapter 3 could not be used. The product of mass, density and thermal capacitance of the ETSC is denoted in the TRNSYS-type as the capacitance of the collector (C). Also, the CV-system was designed to use water as working fluid, thus the properties of water were used. Table 4.1 shows an overview of the design parameters used in the simulation model.

Incidence Angle Modifier

During the day the sun changes position in relation to the surface of a solar collector, which can be defined by the incidence angle. This incidence angle consists of two angles: (i) the solar zenith angle, and (ii) the solar azimuth angle. The zenith angle is the angle between the solar collector and the center of the sun, which influences the longitudinal IAM; a zenith angle of 0° means that the sun is perpendicular to the surface. The azimuth angle is the horizontal angle of the sun's position compared to the solar collector, which influences the transversal IAM; an azimuth angle of 90° means that the sun is positioned west of the solar collector. Figure 4.2 plots the longitudinal and transversal IAM for the ETSC used in the CV-system, while Appendix C.2 discusses the procedure in which these profiles were determined.

4.1.2 Thermo-Differential Valve

Since the TDV is a component that is designed by Conico Valves Bv, there does not exist a TRNSYS-type in the standard library and TESS library. Therefore, the TDV was modelled in TRNSYS using four components: a flow diverter, a tee-piece, a delay input, and a calculator. Figure 4.3 shows an overview of these components in TRNSYS and their connections to each other. The temperature and mass flow from the piping after the ETSC output ($T_{o.p}$ and $\dot{m}_{ETSC}$) are connected to the input of TRNSYS-type11f, which simulates a flow diverter with one input and two outputs. This type uses a control signal to determine the mass flowrates for the two outputs via function 4.4. As a result, either the mass flow flows towards the storage tank ($\dot{m}_{i,st}$) or bypasses the tank ($\dot{m}_{bp}$). It has to be men-

$$(V\rho c_p)_j \frac{dT_n}{dt} + \dot{v}\rho C_p(T_j - T_{i,j-1}) = F'\left(S_j - A_j a_1(T_j - T_a) - A_j a_2(T_j - T_a)\left|(T_j - T_a)\right|\right) \quad \textbf{4.3}$$

Table 4.1 — Design parameters of both the ETSC (Solar Keymark properties) and water used in the CV-system simulation.

Parameter		Value
Number of collectors	[-]	1
$A_{aperture}$	[m^2]	2.78
C	[kJ K^{-1}]	19.662
η_0	[-]	0.761
a_1	[W $m^{-2}K^{-1}$]	2.299
a_2	[W $m^{-2}K^{-2}$]	0.010
c_p	[J $kg^{-1}K^{-1}$]	4190
ρ	[kg m^{-3}]	1000

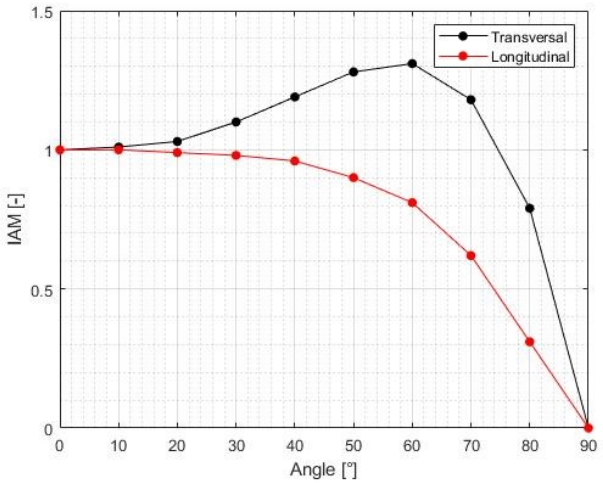

Figure 4.2 — Transversal and longitudinal IAM profile of the ETSC at different incidence angles.

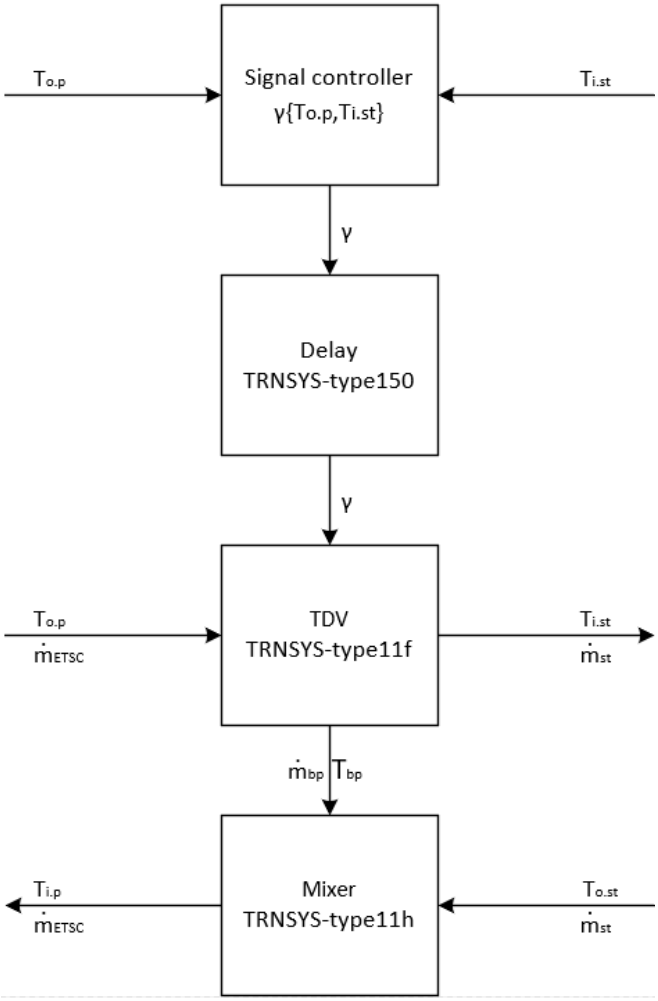

Figure 4.3 — Overview of simulation components of the TDV, and the input and output of each component.

tioned that the temperature output is independent of mass flowrate, which means that the output temperature is equal to the inlet temperature even if there is no mass flowrate.

$$\dot{m}_{out}\begin{cases}\dot{m}_{out,1}=\dot{m}_{in}(1-\gamma)\\ \dot{m}_{out,2}=\dot{m}_{in}\,\gamma\end{cases} \qquad 4.4$$

TRNSYS-type11h was used to combine the mass flow rate from the storage tank ($\dot{m}_{o.st}$) and bypass. As there is only a mass flowrate from the storage tank when the bypass has no mass flowrate (and vice versa), the temperature going to the piping at the ETSC inlet ($T_{i.p}$) either has the temperature of the storage tank ($T_{o.st}$) or the bypass temperature (T_{bp}).

A calculator was used for comparing the pipe outlet temperature with the storage tank temperature at the same height as the inlet temperature of the TDV ($T_{i.st}$), called the signal controller. This controller determines the control signal (γ) using function 4.5**,** in which LT stands for lower than (this is the code used in TRNSYS). This LT-function compares $T_{o.p}$ with $T_{i.st}$, and produces a value of 1 if $T_{o.p} < T_{i.st}$ or 0 if $T_{o.p} > T_{i.st}$ As a result the control signal is 1 if the pipe outlet temperature is lower than the storage tank temperature, resulting in a mass flow output towards the bypass. The control signal is 0 when the pipe outlet temperature is higher, and as a result the mass flow output is towards the storage tank.

$$\gamma = LT(T_{o.p}, T_{i.st}) \cdot 1 + (1 - LT(T_{o.p}, T_{i.st})) \cdot 0 \qquad 4.5$$

TRNSYS-type150 was used for delaying this control signal in case that the TDV needed a certain reaction time for switching position. This type can hold a value for a number of time steps and as a result is dependable on the calculation time step.

4.1.3 Piping

Because it was unknown which TRNSYS-type was used for the hydraulic piping in the reference model from TASK54, a comparison was made between three different TRNSYS-types that are available in the standard TRNSYS library and the extended TESS library. From this comparison, discussed in Appendix C.3, it was concluded that TRNSYS-type709 would be used for the CV-system simulation model. TRNSYS-type709 simulates the thermal behavior of a fluid that flows through a pipe or duct [TESS, Volume 07, 2012].

TRNSYS-type709 is a so-called plug-flow model, which means that the pipe is divided in segments that shift position when a mass flow enters the pipe (a new segment). The size of this new segment is a function of the simulation time step and mass flow rate, which has the temperature of the incoming fluid. The output of the pipe is the segment(s) and/or fraction of a segment equal to the mass of the incoming fluid. Additionally, this model excludes mixing and conduction behavior of adjacent segments. In case that the number of maximum allowed segments is reached, two adjacent segments with a minimum temperature difference will be combined for creating a single segment.

Figure 4.4 shows an example of a pipe divided into three segments, in which each segment has their own temperature (T_1, T_2, and T_3) and length (L_1, L_2 and L_3). In a single time step, a fluid mass with a temperature T_i enters the pipe that displaces the same amount of mass at the outlet of the pipe; in this example, segment 3 and a fraction of segment 2. As a result, the average weighted mass of these segments determines the average outlet temperature (T_0). Equation 4.6 shows the average outlet temperature as function of segment j and a fraction (a) of segment k. In this example segment j is equal to segment 3 and segment k to segment 2. In the simulation, there are two conditions that must be met, namely $0 \leq a \leq 1$, and condition 4.7.

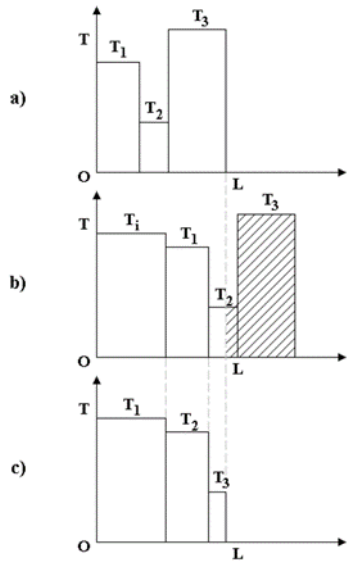

Figure 4.4 — Schematic overview of the pipe displacement principle from TRNSYS-type709 [TESS, Volume07, 2012]

$$T_0 = \frac{1}{\dot{m}\Delta t}\sum_{j=1}^{k-1}\left(M_j T_j + aM_k T_k\right) \quad \textbf{4.6}$$

$$\sum_{j=1}^{k-1}\left(M_j + aM_k\right) = \dot{m}\Delta t \quad \textbf{4.7}$$

Additionally, there are heat losses from the fluid inside the pipe to the environment in each segment; this relation is described in the differential equation 4.8**.** The total resistance of the pipe (UA) is dependent on four resistances: (i) convection between the liquid flowing in the pipe and the pipe wall, (ii) conduction through the pipe wall, (iii) conduction through the insulation material, and (iv) convection to the environment.

$$M_j c_p \frac{dT_j}{dt} = -(UA)_j\left(T_j - T_a\right) \quad \textbf{4.8}$$

Table 4.2 presents the design parameters used in the simulation for the piping. These values are based on the values used in the reference model and material properties: copper tube with a glass-wool insulation layer.

4.1.4 Thermal Storage

TRNSYS-type340 was used for simulating the storage tank in the reference model from TASK54, unfortunately, this type was not compatible with TRNSYS18, and thus an alternative type was used: TRNSYS-type158. This type simulates a cylindrical storage tank with a constant volume, in a vertical configuration, that has two possible inlet and outlet combinations, an auxiliary heat input per node, and a thermostat. The main difference between TRNSYS-type340 and TRNSYS-type158 is the limited number of inlets and outlets [TRNSYS, Volume 4, 2017].

Table 4.2 — Design parameters of the piping used in the CV-system simulation. The parameters are based on the reference model from TASK54 and material properties.

Parameter		Value
D_i	[m]	0.02
D_o	[m]	0.022
L	[m]	10
L_{ins}	[m]	0.013
k_p	[W $m^{-1}K^{-1}$]	401
k_{ins}	[W $m^{-1}K^{-1}$]	0.04
k_{fl}	[W $m^{-1}K^{-1}$]	0.606
μ_{fl}	[kg $m^{-1}s^{-1}$]	0.00089

The numerical model of TRNSYS-type158 is divided into nodes to acquire an appropriate level of stratification. Figure 4.5 shows a schematic overview of the storage tank and a nodal energy balance for a node *j*. As can be seen in this figure, there are several heat transfer mechanisms: storage loss to the environment ($Q_{loss,j}$), conduction between fluid nodes ($Q_{con,j-1}$ and $Q_{con,j+1}$), and addition of thermal heat through a fluid stream ($Q_{fl,j}$). The net balance of these mechanisms results in the stored heat in one node ($Q_{sto,j}$), equation 4.9. Also can be seen that the environmental heat loss is via conduction and convection to the top, bottom and edges of the tank.

$$Q_{sto,j} = Q_{fl,j} + Q_{loss,j} + Q_{con,j} \quad \textbf{4.9}$$

The heat loss to the environment is dependent on the overall energy loss rate (UA) and the ambient temperature, equation 4.10. Furthermore, equation 4.11 describes the conduction between fluid nodes, where A_j is the available surface area for conduction and L_j the height of a node *j*.

$$Q_{loss,j} = UA_{st,j}\left(T_{st,j} - T_a\right) \quad \textbf{4.10}$$

$$Q_{con,j} = k_j A_j \frac{T_j - T_{j+1}}{L_{con,j}} + k_{j-1}A_{j-1}\frac{T_j - T_{j-1}}{L_{con,j-1}} \quad \textbf{4.11}$$

Similar to the piping, the design parameters for the thermal storage were based on the values used in the reference model from TASK54; these values are shown in Table 4.3.

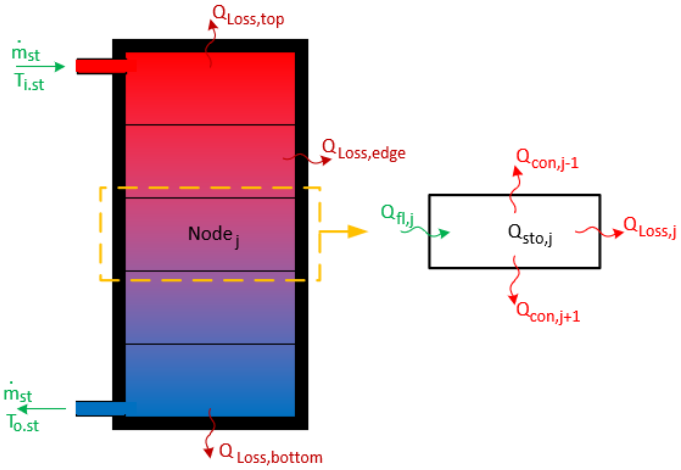

Figure 4.5 — Schematic overview of the storage tank and the nodal energy balance of TRNSYS-type158

Table 4.3 — Design parameters of the thermal storage used in the CV-system simulation. The parameters are based on the reference model from TASK54.

Parameter		Value
V_{st}	[L]	800
D_i	[m]	0.79
UA	[W K^{-1}]	4.4
k_j	[W $m^{-1}K^{-1}$]	1.2
T_a	[°C]	15

4.1.5 Pump

TRNSYS-type114 was chosen for simulating the pump in the CV-system, because it was unknown which TRNSYS-type was used in the reference model from TASK54. TRNSYS-type114 is a single (constant) stage pump that is able to contain a constant mass flow output. Also, this type neglects the startup and stop characteristics of the pump and the effects due to pressure drop. Neglecting these parameters was not important for the numerical research, as these characteristics were unknown. Besides, the numerical research focusses rather on the implementation of the TDV in TRNSYS than the pump characteristics.

In TRNSYS-type114 a mass balance check is performed by comparing the mass flow output with the mass flow input; the mass flow input value is further ignored. The user specifies a single mass flow output, however, a controller can be used that give different mass flow rates based on a parameter, such as the temperature output of the ETSC. Furthermore, the pump on and off status can be controlled using a control signal (γ); if γ < 0.5, then the pump is turned off and if γ ≥ 0.5, then the pump is turned on. Additionally, the model component uses the pump efficiency to determine the temperature change of the fluid inside the pump. In the CV-system this change in temperature was neglected, which means that the temperature at the outlet is always equal to the temperature at the inlet.

4.2 Analysis of the Components

Even though all the simulation types described in paragraph 4.1 were made and tested by the manufacturer TRNSYS, it was not a guarantee for accurately simulating the CV-system. Therefore, an analysis of performance was conducted for several of these types, which are discussed in this paragraph. As the storage tank was only used for storing heat that is acquired in the ETSC, which is controlled by the TDV, its validation was less of importance and for this reason it can be found in Appendix C.4.

4.2.1 Evacuated Tube Solar Collector

Several research topics were conducted in order to validate the TRNSYS-type538. These topics are (i) the temperature and useful energy gain using a constant volume flowrate, (ii) stagnation temperature, (iii) capacity of the ETSC, (iv) dynamic behavior, and (v) the influence of the simulation time step.

Constant Volume Flowrate

The temperature output and useful energy gain were determined using the test conditions described in the Solar Keymark (Appendix B.2.), as the optical efficiency is dependent on the volume flowrate. Additionally, a normal incidence angle was used for the beam irradiation (IAM = 1), and an inlet temperature and ambient temperature of 30 °C. Subsequently, the theoretical temperature output was determined using equation 3.5, 3.7 and 3.8.

Figure 4.6 shows the error in percentage between the output temperature of the simulation and theory, while Figure 4.7 plots the useful energy gain. As can be seen in Figure 4.6, the error was relatively constant using 100 nodes or higher (1,000 nodes is the maximum allowed nodes). Also, there is an error of approximately 0.08%, which is an insignificant error according to Figure 4.7. This figure shows that there is a negligible difference between the simulation data and the test data while using 50 nodes.

Stagnation Temperature

Another aspect of an ETSC is its stagnation temperature, which is the temperature at which equilibrium occurs between the absorbed solar radiation and its heat losses. Be-

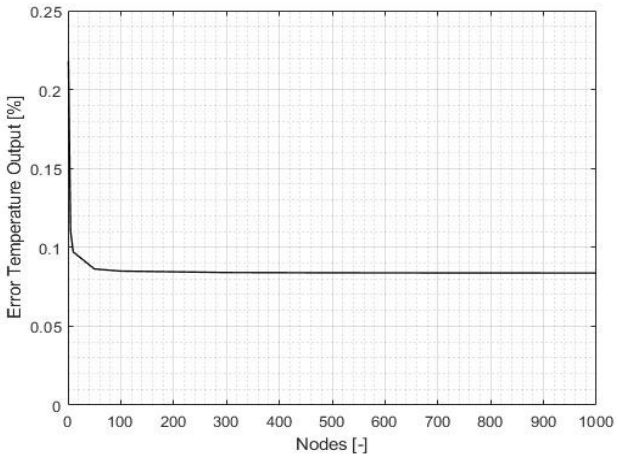

Figure 4.6 — Error of simulation result in comparison to the prediction of outlet temperature using the Solar Keymark test conditions: I = 1,000 W m^{-2}, T_a = 30 °C, $T_{i,ETSC}$ = 30°C and ṁ = 0.0898 kg s^{-1}.

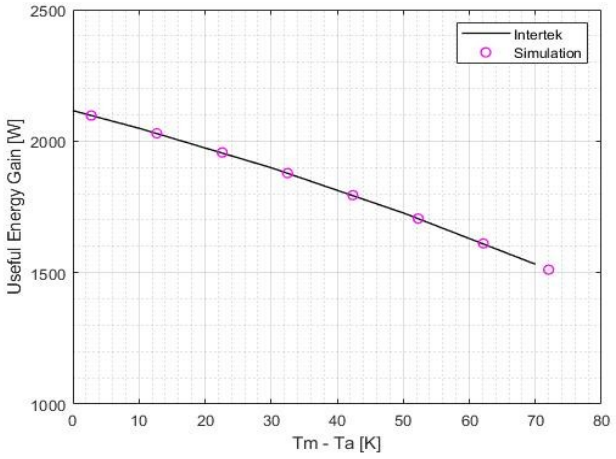

Figure 4.7 — Useful energy gain, due to solar irradiation, compared to mean temperature over the manifold and ambient temperature difference using the Solar Keymark test conditions: n = 50, I = 1,000 W m^{-2}, T_a = 30 °C, $T_{i,ETSC}$ = 30°C and a ṁ = 0.0898 kg s^{-1}.

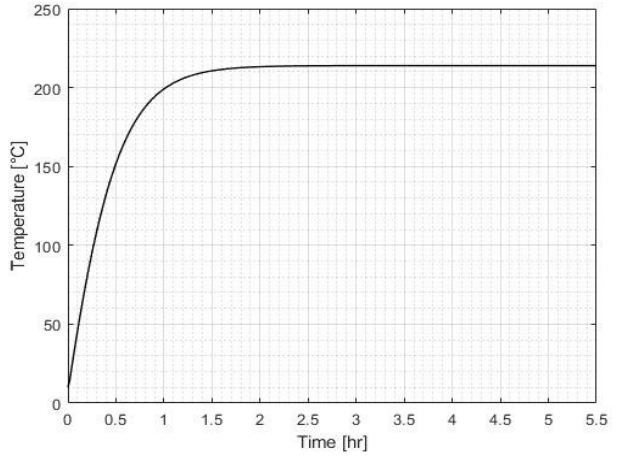

Figure 4.8 — Stagnation temperature profile of the TRNSYS-type538 simulation using I = 1,000 W m^{-2}, T_a = 30 °C and IAM = 1.

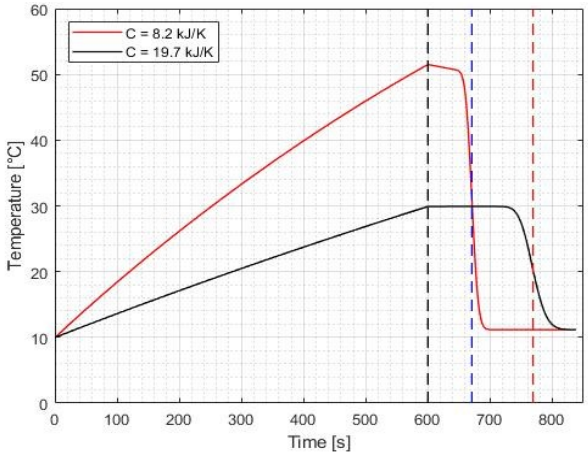

Figure 4.9 — Temperature profiles for a stagnant flow of 600 s (t_1), followed by a volume flow of 100 kg hr^{-1} and I = 1,000 W m^{-2}.

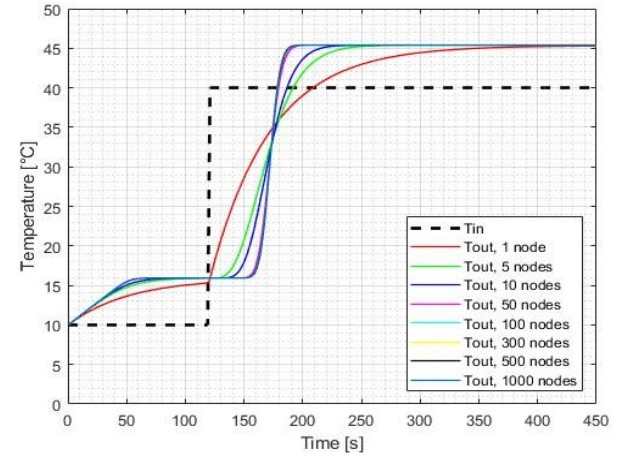

Figure 4.10 — Outlet temperature for different numbers of nodes, after a change in input temperature from 10 °C to 40 °C. The simulation used I = 1,000 W m^{-2}, T_a = 30 °C and a ṁ = 0.0898 kg s^{-1}.

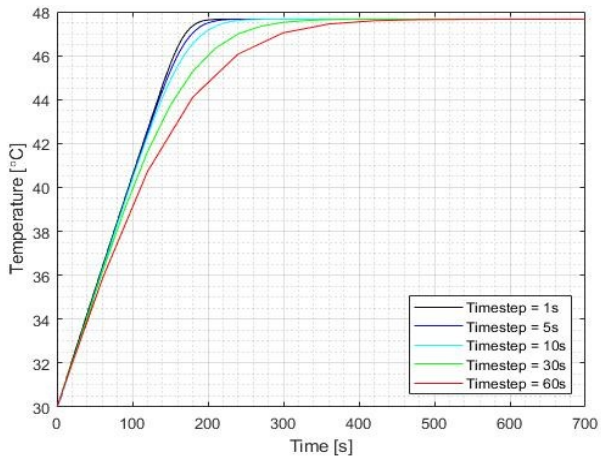

Figure 4.11 — Transient behavior of ETSC temperature output for different time steps. The simulation used I = 1,000 W m^{-2}, T_a = 30 °C and a ṁ = 0.0898 kg s^{-1}

cause the radiation is dependent on meteorological conditions, the ETSC can have different stagnation temperatures [Helden, 2015]. The theoretical stagnation temperature was determined using equation 3.8 for an irradiation level of 1,000 W m^{-2} and ambient temperature of 30 °C. As a result, the theoretical stagnation temperature was 213.9 °C.

The data acquired from the stagnation temperature simulation is plotted in Figure 4.8, and as can be seen, the maximum temperature for equilibrium was 213.9 °C. Unfortunately, the stagnation temperature described in the Solar Keymark was 228.5 °C under similar meteorological conditions. Though, it could be that the certificate used additional diffuse radiation (IAM ≠1) that will increase the amount of absorbed heat, thus the stagnation temperature. If the azimuth angle is adjusted from 0° to 45° in the simulation model, than the diffuse radiation increases and the beam radiation remains the same, as a result the stagnation temperature increases to 228.5 °C.

Capacitance of the ETSC

The capacitance of an ETSC is the amount of heat that is needed to increase the temperature of the working fluid (inside the manifold) with 1 K. Therefore, this parameter has an enormous influence on the performance of the ETSC during start stop operation and dynamic behavior of the ETSC. TRNSYS-type538 uses this capacitance (19.7 kJ K^{-1}) to determine the mass of the working fluid inside the manifold, by multiplying this capacity with the thermal capacity. Unfortunately, this calculation is incorrect as part of the capacitance of the ETSC is related to its construction materials instead of entirely for the working fluid. Consequently, the working fluid mass determined by TRNSYS is approximately 4.96 kg, while the real mass is less than 1.96 kg (C = 8.2 kJ K^{-1}).

Figure 4.9 presents the temperature output profile for both an ETSC capacitance of 8.2 and 19.7 kJ K^{-1}, using a stagnant flow for $\Delta t = t_1$, that is followed by a mass flowrate of 100 kg hr^{-1}. Meanwhile, an radiation level of 1,000 W m^{-2} was used during stagnant flow that after t_1 returned to an irradiation level of 0 W m^{-2}. Also, a (inlet) temperature of 10 °C was used for the initial temperature of the simulation and the temperature when the mass flowrate was applied. Since the mass inside the manifold increases its temperature (> 10°C) till t_1, the temperature output > 10 °C after t_1 represents this mass: (t_2-t_1) for a capacitance of 8.2 kJ K^{-1} and (t_3-t_1) for a capacitance of 19.7 kJ K^{-1}. Furthermore, it can be seen that the slope in which the temperature increases during stagnant flow is steeper for a capacitance of 8.2 kJ K^{-1} than for a capacitance of 19.7 kJ K^{-1}, resulting in a difference in output temperature during the same time period. Unfortunately, the capacitance of the ETSC in the Solar Keymark was determined for acquiring the appropriate value for the outlet temperature, and is not a measure for the mass of the working fluid inside the manifold. Because TRNSYS-type538 does not distinguish the capacitance of the entire ETSC from the capacitance of the working fluid inside the manifold, this type is not able to accurately simulate the mass inside the manifold; thus also not capable of simulating a start stop mechanism.

Dynamic Behavior

Due to the TDV, the CV-system is highly dependent on dynamic behavior; thus also the ETSC. As the theoretical model from chapter 3 describes, an ETSC is dependent on a number of *N* heat pipes that transfer heat throughout the entire manifold, which means that when the input temperature changes it will take time to be noticed at the outlet of the ETSC. When the manifold is divided into 1 node in the simulation model, the input temperature immediately mixes with the entire volume inside the manifold, thereby creating an output temperature that is not realistic. Increasing the number of nodes will result in a more realistic output; however, also increase the simulation calculation time. Figure 4.10 plots the input temperature profile used in the validation (10°C to 40°C) and the outlet temperature profile for different numbers of nodes. This figure shows that there is a negligible temperature difference between using 50 nodes or higher, which means that at least 50 nodes should be used in order to achieve a realistic temperature output.

Simulation Time Step

Lastly, the influence of the simulation time step on the dynamic behavior of the output temperature was investigated. A to large simulation time step (such as 60 s) will result in shorter simulation calculation time, however, will decrease the accuracy of the outlet temperature profile, compared to a short simulation time step (in example 1 s). Figure 4.11 shows the dynamic behavior of the output temperature for different simulation time steps. As can be seen, using a time step of 10 s or less will result in a significantly small temperature difference, thus the time step should be maximal 10 s.

Conclusion

TRNSYS-type538 is suitable for simulating the dynamic behavior of the ETSC, as demonstrated in this section; however, this type cannot accurately simulate the start stop operation. The numerical model behind this type does not distinguish the capacitance of the entire solar collector with the capacitance of the working fluid in the manifold, as a result this type calculates an incorrect mass output during start stop operation. Unfortunately, there was no alternative solar collector model found in the standard library and TESS library that does distinguish between these capacitance rates at the moment of conducting this numerical research. Therefore, more research is required to find an alternative type outside these libraries or a new type has to be developed.

4.2.2 Thermo-Differential Valve

A verification of the TDV simulation model was required in order to observe whether the model functioned as it was supposed to. An input temperature profile was used in combination with a constant mass flowrate of 300 kg hr^{-1} and a storage tank temperature of 65 °C to verify this TDV model. Figure 4.12 shows both the TDV inlet and storage tank inlet temperature profile and the mass flow rates at the outlet towards the storage tank and bypass. As can be seen, the temperature profile starts with a temperature lower than the tank temperature, which results in a mass flow in the bypass; the mass flow towards the tank remains 0. At the moment that the input temperature becomes higher than the storage tank, there is an immediate change in mass flow output.

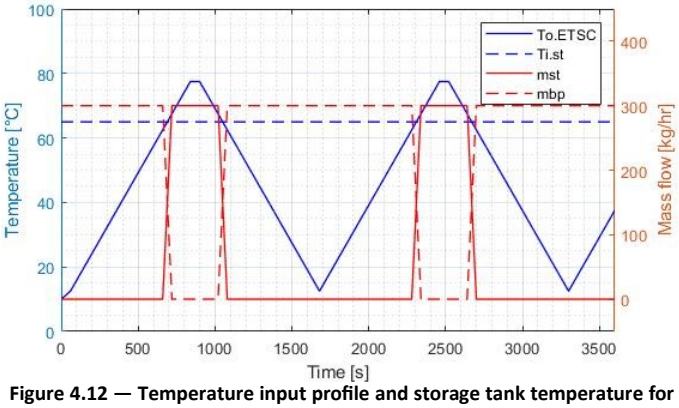

Figure 4.12 — Temperature input profile and storage tank temperature for validating the mass flow output of the TDV simulation. And the mass flow output of the TDV towards the storage tank and bypass.

The previous evaluation was conducted without using a delay; however, due to TRNSYS-type150 this is possible. Figure 4.13 plots the mass flowrate at the outlet towards the storage tank and bypass, while using the same conditions as used in the previous evaluation, with and without a delay of 5 times the simulation time step. As can be seen in this figure, the first change in position without a delay is approximately at t = 625 s, while the same change is around t = 1000 s for the simulation with a delay.

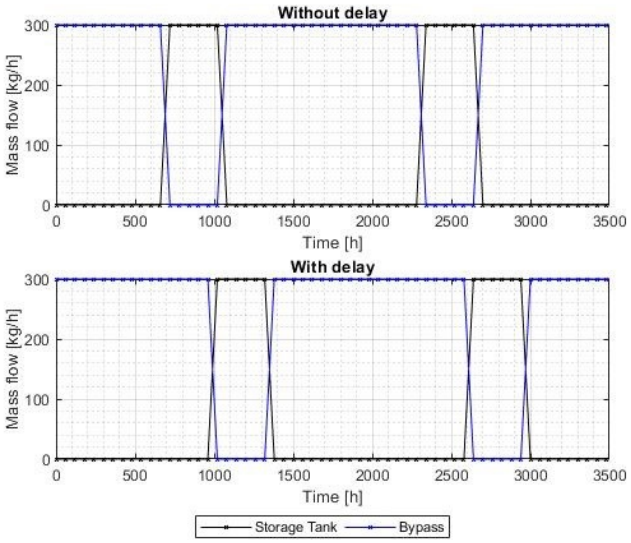

Figure 4.13 — Mass flow rate for TDV outlet towards storage tank and bypass with and without a delay of 5 times the timestep.

As mentioned before, the TDV is highly dependent on dynamic behavior and with it dependent on the simulation time step. The influence of the simulation time step on the reaction of the TDV is indicated in Figure 4.14. This figure shows that the TDV changes position with a faster response when using a small simulation time step (15 s) rather than a large time step (60 s). The advantage of a faster response is that the model has a higher accuracy of simulating the real response (less than a second), resulting in more realistic heat gain in the storage tank. Lastly, it can also be seen that the moment of changing position by the TDV occurs at different times, which is related to the temperature input file to the TDV; this file is correlated to the time step in TRNSYS.

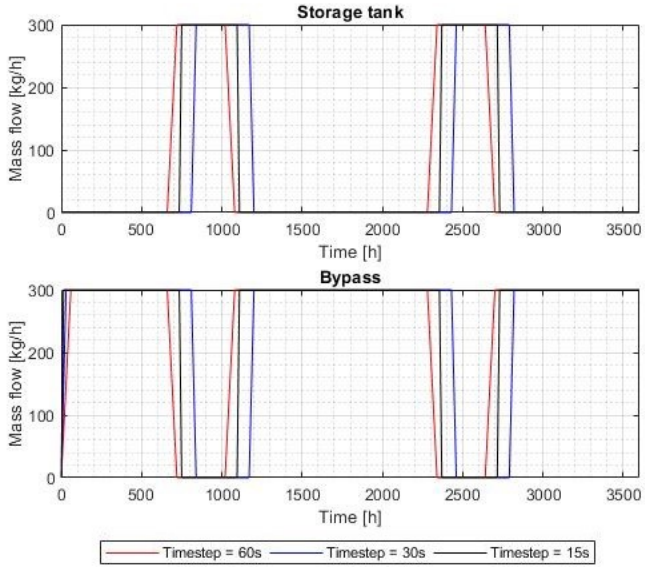

Figure 4.14 — Mass flow rate for TDV outlet towards storage tank and bypass for different timesteps

Based on the data provided in this section, it can be concluded that the TDV behavior can accurately be simulated in TRNSYS. However, the simulation time step has an enormous influence on the temperature and mass output, and with it the thermal performance of the CV-system.

4.2.3 Piping

Several research topics were conducted in order to validate the TRNSYS-type709: (i) dynamic behavior, (ii) stagnant behavior, (iii) number of nodes, and (iv) simulation time step. The simulation results from TRNSYS were compared to a theoretical model that is described in Appendix C.3.

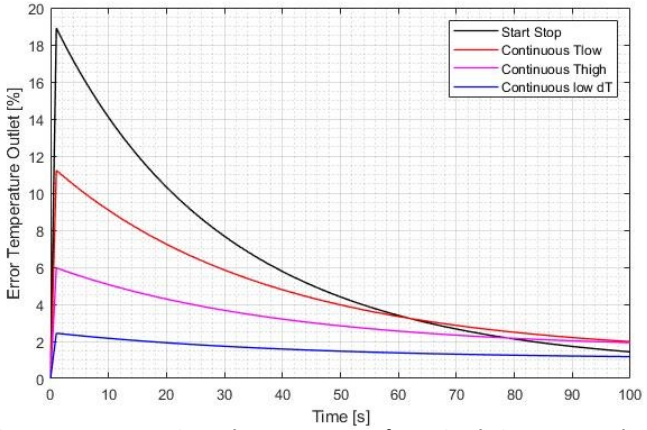

Figure 4.15 — Error in outlet temperature from simulation compared to theory for four different scenarios. 100 nodes were used in the TRNSYS simulation and T_a = 15 °C.

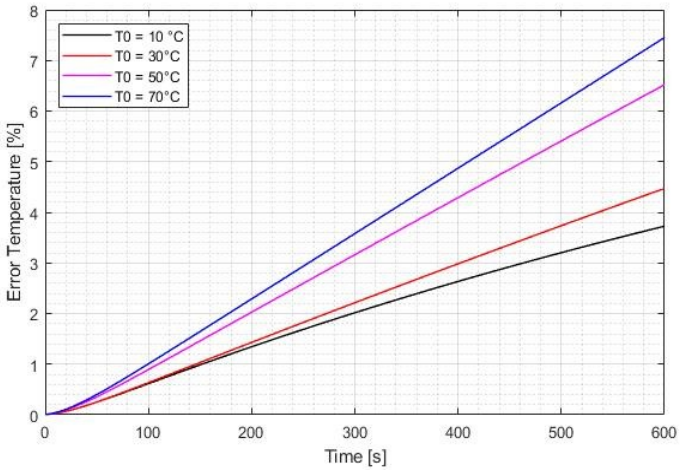

Figure 4.16 — Error in temperature from simulation compared to theory for a stagnant flow using four different initial temperatures, 100 nodes and T_a = 15 °C.

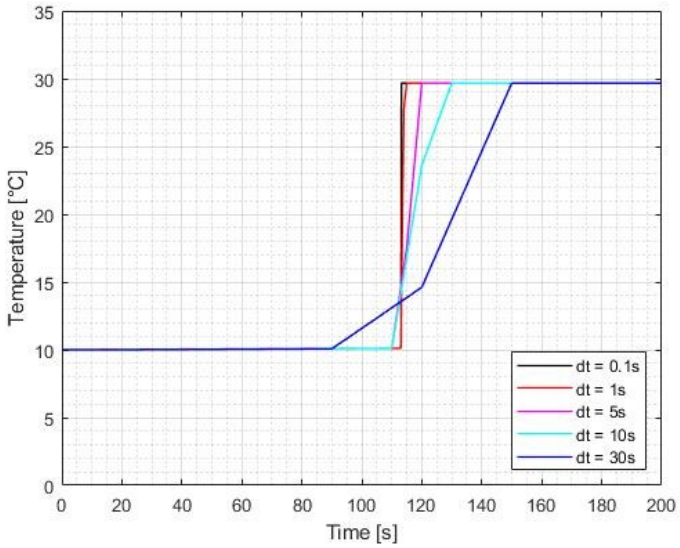

Figure 4.17 — Outlet temperature from the simulation using five different time steps for a change in temperature of 10 °C to 30°C. The model used 100 nodes, $\dot{m}$ = 300 kg hr^{-1} and T_a = 15 °C.

Dynamic Behavior

Similar to the ETSC, the piping is highly dependent on dynamic fluctuations due to the TDV in the CV-system. Due to this dynamic fluctuation, a sudden increase in temperature might be noticed at the pipe inlet that influences the pipe outlet temperature. The theoretical model in Appendix C.3 shows that a sudden increase in inlet temperature influences the heat losses to the environment and the heat storage in the pipe wall for a certain mass flowrate. Because of the influence of these parameters, four different scenarios were developed in order to validate the simulation model.

The first scenario describes the parameters that represent the start stop operation, in which a high temperature difference is acquired (in example 10 to 60 °C) at a high mass flowrate (283 kg hr^{-1}). The second scenario represents a continuous mass flowrate (113 kg hr^{-1}) with a pipe inlet temperature increase at a low temperature (10 to 30 °C), while another scenario uses a similar mass flowrate at a high temperature (60 to 70°C). A last scenario characterizes a continuous mass flowrate in which a low temperature increase (30 to 32° C) is noticed, which is often the case during continuous operation. For each scenario, the error was observed between the pipe outlet temperature of the simulation and the according theoretical values for t = 100 s, Figure 4.15.

As can be seen in Figure 4.15, the highest error in temperature output is acquired in the start stop scenario. The outlet temperature error deviates between 19 and 10 % for this scenario, as the mass inside the solar collector needs approximately 23 s to reach the outlet (m = 1.96 kg). Furthermore, this figure shows that the continuous flow has a lower error when using high temperatures than using low temperatures. This difference might be related to the high influence of heat losses to the environment compared to the storage rate in the pipe wall, while using high temperatures. However, the smallest error (approximately 2.5%) was observed when using a low temperature increase, which represents the continuous flow operation. In conclusion, the dynamic behavior might be feasible for simulating a continuous operation, while it simulates incorrect values using the start stop operation.

Stagnant Behavior

Besides the dynamic behavior of the CV-system, the pipe experiences a stagnant flow because of the start stop operation. This flow results in continuous heat losses to the environment and heat storage in the pipe wall of the entire mass in the piping (Appendix C.3). For the validation, the error in temperature inside the manifold between theory and simulation was determined using four different initial temperatures, plotted in Figure 4.16. As this figure shows, the error increases over time and since the stagnant period in operation mode is 600 s, the error eventually deviates between 3.8 and 7.4 %

depending on the initial temperature. Consequently, when a volume flow is applied after this period, a volume with an incorrect temperature is transported further throughout the CV-system resulting in an unrealistic profile. It has to be noted that the closer the initial temperature is to the ambient temperature, the smaller the error becomes.

Simulation Time Step

Similar to the validation used in the solar collector, the simulation time step has the highest accuracy when it is chosen as small as possible, thereby increasing the simulation calculation time. The influence of this time step on the temperature output of the pipe was investigated by suddenly increasing the inlet temperature from 10 to 30 °C, which is shown in Figure 4.17. Because a mass flow rate of 100 kg hr^{-1} was used, it takes approximately 113 s before a temperature rise is visible at the outlet of the pipe. It can be seen in Figure 4.17 that when a time step of 5 s or higher is used it results in a change in outlet temperature before 113 s, which is not realistic. Additionally, there is a negligible difference in the temperature outlet profile for a time step of 1 s and 0.1 s. For realistically simulating the pipe outlet temperature it is recommended to use a time step as close as possible to 1 s.

Conclusion

The data discussed in this section shows that the inaccuracy in dynamic behavior is around 2.5 % between the theory and simulation when using a continuous mass flowrate and a small temperature difference. Despite this inaccuracy, it was concluded that this TRNSYS-type can be used for simulating the continuous operation of the CV-system. However, there is a significant outlet temperature difference in both the dynamic and stagnant behavior when a start stop operation is used, which results in an inaccurate temperature response compared to reality. As there was no better alternative found, more research is required in order to find a more suitable piping simulation model.

5| Case Study

In order to investigate the feasibility of simulating the CV-system described in Chapter 4 in TRNSYS, two cases were developed that are based on the CV-system control operation: continuous operation and start stop operation. Despite the results found for each component in the system component analysis, Paragraph 4.2, these components were used in these cases. As a result, the values found in this chapter do not represent the reality and cannot be accurately compared to the measurement conducted by [Kratz, 2018]. Additionally, only the temperature profiles were available throughout the system during the measurement, but it was unknown what the other parameters were; for example the solar radiation profile. Though, this research was conducted in order to verify that a similar pattern can be reached in temperature profiles throughout the system in comparison to these measurements.

Three different node configurations were examined during the simulations, namely configuration 1 representing a minimum number of nodes per component (yet still realistic), configuration 2 consisting of the minimum number of nodes determined during the system component analysis, and configuration 3 using the maximum allowed nodes for each component. Table 5.1 presents the values for each of these configurations per component.

Table 5.1 — Three different node configurations used during the analysis of determining the influence of the number of nodes

Configuration	ETSC	Piping	Storage Tank
1: Minimum nodes	10	10	10
2: Analysis Chapter 4	50	50	25
3: Maximum nodes	1000	100	50

5.1 Case 1 - Continuous Operation

The continuous operation research was divided into two topics, for analyzing the thermal performance of the CV-system. The first topic investigates the performance using node configuration 3, the design parameters described in Chapter 4, no delay in TDV, and the simulation parameters which are defined in Table 5.2. The second topic investigates the influence of using a delay in the TDV, node configuration, and simulation time step on the thermal performance.

5.1.1 Simulation Data

The measurement data during continuous operation from [Kratz, 2018] is plotted in Figure 5.1, which shows the temperature profile at the outlet of the ETSC ($T_{o.ETSC}$), the temperature at the inlet of the TDV ($T_{i.TDV}$), the temperature towards the inlet of the ETSC close to the storage tank (T_{supply}), and the temperature inside the storage tank at the same height as the TDV (T_{TDV}); Figure 4.1 shows the location of these temperature profiles in the CV-system. As can be seen in Figure 5.1, there is a delay between the $T_{o.ETSC}$ and $T_{i.TDV}$ temperature profile, which is related to the piping between the ETSC and the TDV, and as a result , a parabolic temperature profile is acquired at $T_{i.TDV}$ that is higher than T_{TDV}. At the moment that $T_{i.TDV} > T_{TDV}$, the mass flow is directed from the TDV through the storage tank, resulting in a displacement of mass from the bottom of the storage tank towards the inlet of the ETSC. Since this mass has a lower temperature than the top of the storage tank, the T_{supply} signal decreases directly.

Table 5.2 — Simulation parameters used during the continuous operation analysis

Parameter		Value
I	[W m^{-2}]	800
T_0	[°C]	30
$T_{a.ETSC}$	[°C]	30
$T_{a.p}$	[°C]	15
$\dot{m}$	[kg hr^{-1}]	120
Simulation time step	[s]	1
Simulation run time	[s]	3600

Figure 5.2 presents the simulation data that was acquired for the same temperature profiles by TRNSYS, which shows a comparable pattern as plotted in Figure 5.1. However, there are differences noticeable between temperature profiles, such as the temperature decrease in T_{supply} that could be related to the location of piping in the system. The TRNSYS model assumes that there is 10 m piping between the ETSC and the TDV and 10 m between the pump and the ETSC, while in reality all components are connected with a certain length of piping, and according to Chapter 4, this has an influence on the temperature profiles. Additionally, the parameters in the measurement are not constant, such as the radiation level and incidence angle, while the TRNSYS model assumes these parameters to be constant, which could also result in deviations between temperature profiles. The main conclusion of the simulation data was that similar temperature profiles can be simulated in TRNSYS for a continuous operation, though the location and length of the piping in the system need to be accurately defined.

The mass flowrate through the storage tank was compared to the temperature profile of the node in the storage tank at the same height of the TDV, Figure 5.3. As can be seen, the temperature only increases when there is a mass

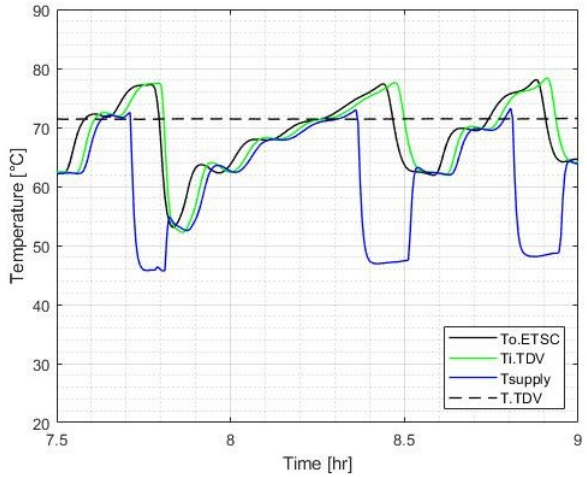

Figure 5.1 — Measurement data from the CV-system during continuous operation [Kratz, 2018] .

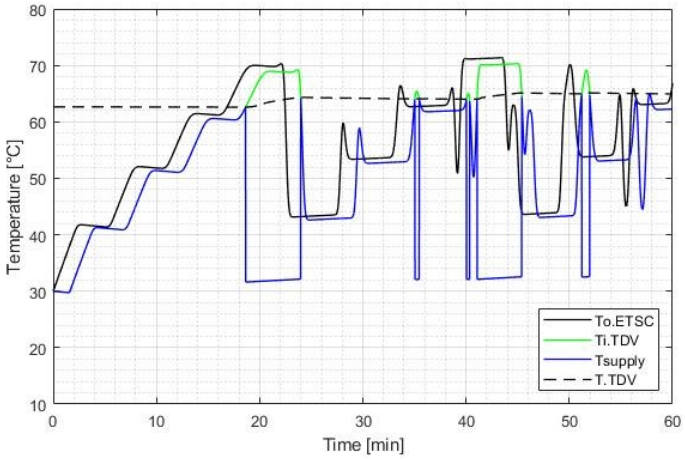

Figure 5.2 — Temperature profiles of the continuous operation simulation in TRNSYS using the parameters specified in Table 5.2 with no delay in changing position between TDV outlets.

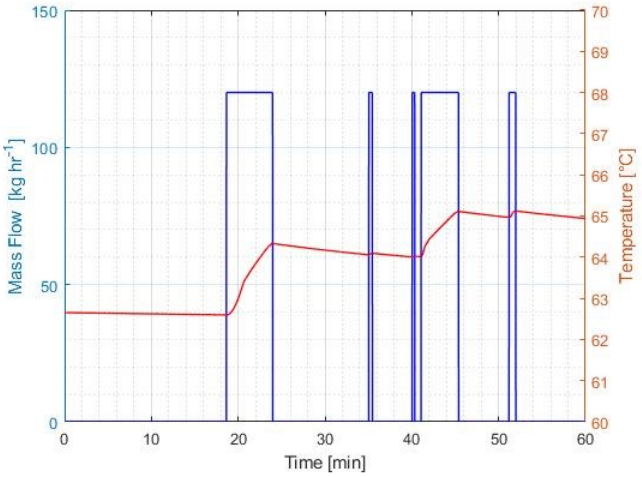

Figure 5.3 — Mass flow profile through the storage tank and the temperature profile in the storage tank at height of the TDV inlet, during the continuous operation simulation in TRNSYS.

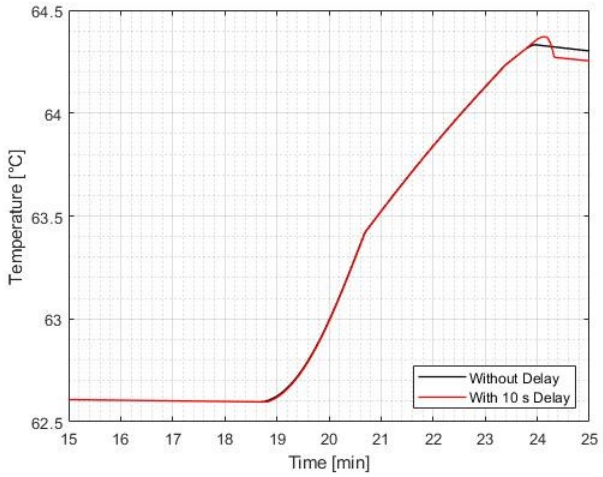

Figure 5.4 — Temperature profile in the storage tank at height of the TDV inlet, during the continuous operation simulation in TRNSYS, with and without a delay of 10 s in changing position between TDV outlets.

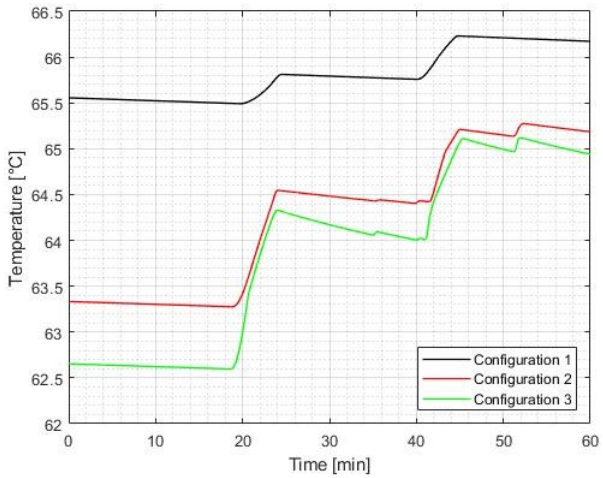

Figure 5.5 — Temperature profile in the storage tank at height of the TDV inlet, during the continuous operation simulation in TRNSYS, for the three different node configurations.

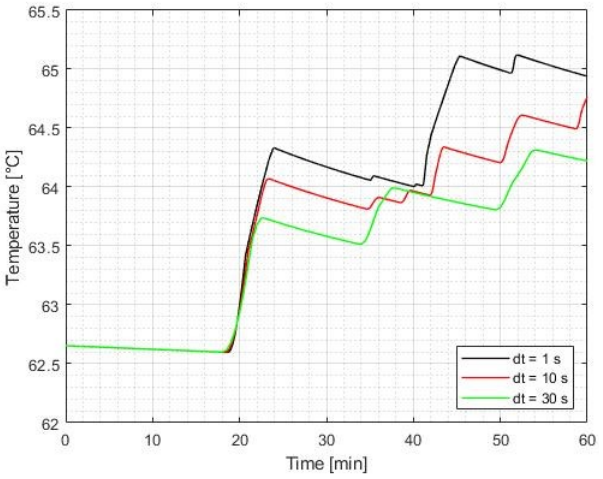

Figure 5.6 — Temperature profile in the storage tank at height of the TDV inlet, during the continuous operation simulation in TRNSYS, for different simulation time steps

flow rate to the storage tank, which visualizes the temperature input coming from the TDV, and decreases in temperature in absence of a mass flow rate, due to heat losses to the environment and conduction between storage tank nodes. Even though the temperature profile in the storage tank could be realistic, TRNSYS-type158 is not able to determine the heat storage rate in the storage tank as heat can be generated during multiple cycles through the ETSC.

5.1.2 Configuration Analysis

As explained in Chapter 4, the TDV can be simulated either with or without a delay that is based on the simulation time step. Figure 5.4 plots the temperature profile of the node in the storage tank at height of the TDV with and without a delay of 10 times the simulation time step (= 10 s). From this figure it can be noticed that up until approximately 23 min both temperature profiles were equal, which is the start of the simulation until the first input from the TDV, and shows different results afterwards. In absence of a delay in the TDV, only flows with a higher temperature than the node temperature entered the storage tank, which resulted in an increase in temperature followed by a decrease in temperature due to heat losses (Figure 5.3). When a delay is applied in the TDV, the mass flow will continue to flow towards the storage tank, for 10s, even when the temperature in the TDV became lower than the node temperature. At this moment the node temperature decreased resulting in lower node temperatures in comparison to when no delay was applied.

Node configuration 3 was used in the analysis of Paragraph 5.1.1 in order to acquire the most realistic results, while different node configuration could have been used. Figure 5.5 shows the node temperature profile for these configurations during the same simulation time. As can be seen in this figure, the initial node temperature differs in each configuration due to the stratification level inside the tank, which is dependent on number of nodes (Appendix C.4), as the TDV is located at 80 % of the storage tank height. This difference in temperature has an enormous impact on the node temperature gain as the TDV switches position later if the node temperature is higher. Furthermore, the heat losses in the storage tank were higher when a larger number of nodes was used, which could be related to the heat loss rate due to conduction between nodes (equation 4.4); a larger number of nodes results in a smaller L_{con} compared to a smaller number of nodes, thus the heat loss rate due to conduction becomes higher. Also mixing of nodes might occur when using a large number of nodes as the initial temperature difference between nodes is relatively small compared to using a smaller number of nodes. Eventually, the heat gain between configuration 2 and 3 becomes fairly similar, and thus it was concluded that (especially) the number of nodes in the storage tank influences the thermal performance of the CV-system.

A last parameter that was analyzed was the influence of the simulation time step on the node temperature profile, Figure 5.6. This figure shows that there is a difference in both the pattern of the temperature profile between different simulation time steps, heat gain and heat loss pattern, and in thermal performance of the CV-system, height of temperature profile. This difference could be related to the calculation made by TRNSYS, which averages all values in the system (such as temperature) over one time step. This averaging of values is crucial in the thermal performance as the CV-system is highly dependent on dynamic behavior. This relation is verified in Figure 5.6, which shows that the temperature profile was significantly lower while using large time steps (30 s) than using small time steps (1 s).

5.1.3 Conclusion

From the data provided in this paragraph, it seems that TRNSYS is capable of accurately simulating the CV-system during continuous operation, despite the incorrect data output from several TRNSYS-types. However, it has to be noted that the simulation data is highly dependent on design parameters, such as the location and length of the piping, and on the parameters of the simulation configuration, mainly the number of nodes used in the storage tank and simulation time step. Therefore, extra care needs to be taken when defining these parameters before running an entire simulation as a yearly simulation will take a long simulation calculation time.

Since this research was conducted using constant parameters, it is recommended to also run a simulation with variable parameters that would represent a daily cycle. During a daily cycle, the ambient temperature, the solar radiation and the solar path (incidence angle) changes, thereby influencing the thermal performance of the ETSC and heat losses to the environment, and with it the overall thermal performance.

5.2 Case 2 - Start Stop Operation

The analysis of the start stop operation in TRNSYS consist of a comparison of the temperature and mass profiles obtained from TRNSYS and the measurement that was performed by [Kratz, 2018]. In contrast to the continuous operation, an analysis on the influence of a delay in TDV, node configuration and time step on the thermal performance are not discussed in this paragraph, as similar results were found as in paragraph 5.1.

The design parameters, discussed in chapter 4, were used in the simulation in combination with the simulation parameters shown in Table 5.3, which were chosen to acquire a representative temperature profile compared to the measurement. Additionally, a delay of 6 times the simulation time step was used for changing position between the TDV outlets, and the start stop operation of the pump was divided into a

Table 5.3 — Simulation parameters used during the start stop operation analysis

Parameter		Value
I	[W m^{-2}]	350
T_0	[°C]	32
$T_{a.ETSC}$	[°C]	30
$T_{a.p}$	[°C]	15
$\dot{m}_{continuous}$	[kg hr^{-1}]	600
Simulation time step	[s]	1
Simulation run time	[s]	3600

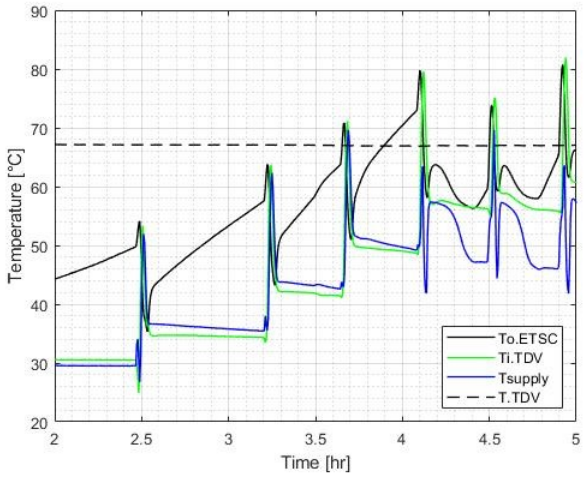

Figure 5.7 — Measurement data from the CV-system during start stop operation [Kratz, 2018] .

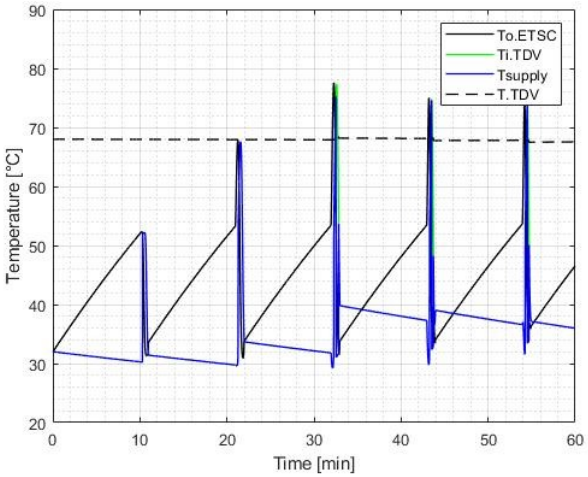

Figure 5.8 — Temperature profiles of the start stop operation simulation in TRNSYS using the parameters specified in Table 5.2 with 6 s delay in changing position between TDV outlets.

stagnant period of 600 s followed by a volume flow period of 60 s. These time periods were also chosen to acquire similar temperature profiles as in the measurement, though these periods are not the values used during the measurement.

Figure 5.7 presents the temperature profiles throughout the CV-system observed by the measurement that was performed by [Kratz, 2018]. As can be seen in this figure, the temperature increases gradually in the ETSC between t = 2 hr and approximately t = 2.5 hr. $T_{o.ETSC}$ shows the temperature profile of the outlet of the ETSC, however, this temperature is equal to the temperature in the ETSC during the stagnant period. The start of the volume flow period can be observed by a sudden increase in $T_{o.ETSC}$, which is related to a fluid temperature increase under continuous operation conditions, followed by a sudden decrease in temperature, which is the result of cold water entering the ETSC (T_{supply}).

During the stagnant period, $T_{i.TDV}$ and T_{supply} lose heat to the environment, resulting in a decrease in its temperature. Though, Figure 5.7 shows that $T_{i.TDV}$ and T_{supply} were almost constant during the stagnant period, meaning that the heat losses to the environment were minimal. During the volume flow period, the volume inside the piping before the ETSC is displaced towards the ETSC, which has a temperature equal to T_{supply}. Additionally, there is a delay visible between $T_{o.ETSC}$ and $T_{i.TDV}$ that is related to the time needed for the water to travel through the piping. Furthermore, $T_{i.TDV} < T_{TDV}$ after one cycle of these periods, thus no heat is transported to the storage tank, and the process is repeated. At the moment that $T_{i.TDV} > T_{TDV}$, the water is directed to the storage tank with a delay in switching position between TDV outputs.

The same temperature profiles were determined using TRSNSYS, from which the results are plotted in Figure 5.8. This figure shows similar temperature patterns as described in the previous section; firstly, a gradual increase in temperature during stagnant period in the ETSC, followed by a sudden increase in temperature, and almost immediately afterwards a rapid decrease. Secondly, there was a gradual temperature decrease in the piping (T_{supply} and $T_{i.TDV}$) during the stagnant period and, in the volume flow period, a high peak of a warm volume. As the start stop mechanism operates mainly during morning and evening periods, when the radiation level is insufficient for continuous operation, both the ambient temperature and solar radiation changes rapidly. As a result, the thermal gain in the ETSC changes during the time, which can be observed in the measurement data, Figure 5.7. Since the simulation uses constant parameters, there is a difference in temperature profiles between measurement and simulation. In spite of this difference, it seems that TRNSYS is able to simulate the start stop operation, however, conclusive research is required in order to verify this hypothesis.

6| Conclusions and Recommendations

The aim of this master thesis was divided into two separate research topics, in which the first research, the experimental research, aimed on investigating the difference in thermal performance of the ETSC between using a continuous and start stop operation. The focus of this research was to improve the experimental setup and defining the influence of several parameters on the thermal performance of the ETSC that is used in the CV-system. These parameters were based on a theoretical model of an ETSC. The second research topic, the numerical research, aimed to determine whether it was possible to simulate the CV-system in TRNSYS. This research focusses on the accuracy of individual TRNSYS-types used in the CV-system and on similarities between the simulation, that uses constant parameters, and a measurement performed by Conico Valves bv.

6.1 Conclusions

Experimental Setup

The data provided in this report shows that the improved experimental setup was designed according to the design requirements, which were based on the NEN-EN-ISO 9806 norm for solar thermal testing. Firstly, the standard uncertainties of the thermocouples (0.12 and 0.13 °C) used in the setup were higher than the allowed uncertainty (0.1 °C); however, this was the result of assuming an uncertainty in the thermal bath of 0.10 °C. When this value is halved, which is more realistic, than the standard uncertainty reduces to approximately 0.8 °C, which is less than the allowed uncertainty. Additionally, the allowed deviation of $\Delta T / T_M$ (0.4 °C) was also lower than the design requirement (0.05 °C).

Secondly, the thermocouple in the setup, located at the temperature sensor of the thermostatic valve, which experienced higher heat losses to the environment that could be related to incorrect installment of this thermocouple. However, as the thermocouple at the inlet of the ETSC showed accurate readings, this thermocouple was used for determining the stability and temperature range of the setup. It was found in the verification that the inlet temperature profile at the ETSC was stable for at least a time period of 5 min, and had a temperature range of 10 to 50 °C.

Furthermore, it was found that the original signal of the volume flowmeter acquired a noise signal, which was reduced using a Savitzky-Golay filter; there was a deviation in volume flowrate during a stagnant flow. As a result of this filter, the deviation in volume flowrate was reduced to significantly low values compared to the allowed deviation from the NEN-EN-ISO 9806 norm. Additionally, the volume flow ranges between 0.2 and 5.0 L min^{-1} in the experimental setup, which is lower than the design requirement (6 L min^{-1}). Though, a volume flowrate of 5 L min^{-1} is still sufficient for the experimental research.

Lastly, in the experimental research it was observed that the measurements were performed according to the design requirements. The deviation was less than the boundaries of these requirements, temperature (±1 °C) and volume flowrate (2 %), for measurements groups that uses the same set inlet temperature at the ETSC or set volume flowrate.

Experimental Research

From the theoretical model it was concluded that there are three main parameters that influences the thermal performance of an ETSC besides its construction material and geometry: solar radiation, inlet temperature, and volume flowrate. Especially, the volume flowrate has an important influence on the optical efficiency, because it changes the convective heat transfer rate between the evacuated tube and the working fluid in the manifold.

From the experiment results it was found that the optical efficiency slightly decreases when the volume flowrate decreases. Although, it seems that using a constant volume flowrate achieves higher optical efficiencies than using a start stop operation. This might be related to the influence of lower convective heat transfer rates at lower volume flowrates, or because heat is lost to adjacent fluid volumes at the inlet and outlet of the ETSC during a stagnant flow .

In the experimental research, it was also observed that the emitted radiation of the solar simulator is different than its radiation setting, which could be related to the distance between the solar simulator and the ETSC resulting in a spectral mismatch. Furthermore, it was noticed that there is a deviation in the emitted radiation profile that, according to the sensitivity analysis, could have an influence on the thermal performance of the ETSC throughout a measurement.

In the analysis of investigating the optical efficiency between start stop and continuous operation, it was assumed that there was a constant linear and quadratic heat loss coefficient. However, the sensitivity analysis shows that these loss coefficients change with the volume flowrate, thereby influencing the optical efficiency. Additional experiments were performed from which it was concluded that there is a small difference in optical efficiency between these experiments and the ones used in the comparison between start stop and continuous operation.

Finally, it was also concluded in the sensitivity analysis that several parameters influence the thermal performance during start stop operation: the mean temperature over the collector, initial temperature, and emitted radiation during the continuous period. Both temperatures had to be estimated based on the experimental data and are therefore susceptible for deviation in calculated thermal performance, while the solar radiation was measured. Since the mean temperature over the collector changes throughout the measurement, the heat loss coefficients also change and with it the optical efficiency. Furthermore, the influence of the initial temperature and radiation level were concluded to have a negligible effect on the thermal performance.

Numerical Research

Firstly, the individual components were investigated that were used in the CV-system layout in TRNSYS. There was no TRNSYS component available for the TDV, as it is a novel concept, which had to be created using standard TRNSYS-types and was proven to work as it should be during a verification analysis. Furthermore, the TRNSYS-type538 was used for simulating the ETSC, which is suitable for simulating the ETSC during continuous operation. However, this TRNSYS-type is incapable of distinguishing the difference between the capacity of the fluid inside the manifold from the entire capacity, and as a result this type calculates an incorrect mass output during start stop operation. Unfortunately, there was no alternative found for replacing this TRNSYS-type.

Similar to the ETSC simulation component, the pipe simulation component also showed deviations between the theoretically determined and simulated temperature output. During the dynamic behavior analysis, a deviation of 2.5% was observed while simulating the continuous operation, which was assumed to be an acceptable deviation; this deviation occurs occasionally during continuous operation. On the contrary, when a start stop operation was simulated, both the dynamic and stagnant behavior showed inaccurate temperature responses. Also for the pipe simulation model, there was no other suitable alternative found.

Secondly, the entire CV-system in TRNSYS was compared to measurements, performed by Conico Valves bv, using two cases: the continuous operation and start stop operation. As some of the parameters from the measurements were unknown (such as solar radiation level and solar path) and the temperature output of the system layout was inaccurate, the simulation data could only be compared to the measurement data on the shape of the temperature profiles. It was concluded during both these analyses that TRNSYS is capable of accurately simulating the CV-system during continuous and start stop operation. Though, this accuracy is highly dependent on the design parameters, for instance the location and length of piping, and the simulation parameters, such as time step and node configurations.

6.2 Recommendations

Experimental setup

During the verification of the experimental setup, several aspects were found that could be improved. First of all, the filter had to be removed in order to acquire higher volume flowrates, since the filter caused high pressure resistance. A filter has to be placed in order to fully fulfill the design requirements. Secondly, the needle valves and the thermostatic valves could be replaced with electronic operating valves for acquiring an autonomous setup. Lastly, the setup requires more insulation in order to reach lower temperatures or to acquire a more stable temperature signal during measurements at low temperatures (<10°C).

Experimental research

The characteristics of the volume flow influences the convective heat transfer rate between the working fluid inside the manifold and the evacuated tube, thus the optical efficiency. As the geometry of the manifold did not allow to determine this characteristic (Reynolds number), this influence during the measurements could not be verified. In order to find a more conclusive result of this influence, more research is required to analyze the development of convective heat transfer rate through the manifold at different volume flowrates.

The results found during the start stop operation used an approximation based on a continuous volume flowrate, mainly the heat loss coefficients. However, the start stop operation deviates in working principle from a continuous operation, which could mean that another analysis of data is required in order to find the appropriate optical efficiencies.

Numerical Research

It is recommended to conduct more research on either finding or creating a more appropriate TRNSYS-type for simulating the ETSC and piping. Both these simulation types have an enormous influence, especially during start stop operation, on the thermal performance of the CV-system. During the master thesis it was decided that it was not useful to conduct research using weather data, as the simulation model did not represent the reality. Therefore, when more appropriate simulation models are found, they can be used for conducting a more detailed research on comparing the measurement data with the simulation data.

Bibliography

Almond, D. (2018). Why use a magnetic flow meter? The pros and cons. Retrieved from PVL Engineers Supplying Engineers: http://www.pvl.co.uk/

Apricus. (2018). Evacuated Tube Solar Collectors. Retrieved from Apricus Solar Hot Water: http://www.apricus.com/html/solar_collector.htm#.W2v17tIzaUk

Aucklat. (2017). Efficiency adjusting factor. Retrieved from Aucklat Heating World: Solar water heating, wood pellot stove heating, gas heating: http://www.aucklatsolar.com/efficiency2.html

Azad, E. (2007). Theoretical and experimental investigation of heat pipe solar collector. Tehran: Iranian Research Organization for Science and Technology.

Bachmann, S., Fischer, S., & hafner, B. (2017). Definition of reference solar combi system, Germany. Stuttgart: ITW.

Balkom, M. v. (2015). Design of a new experimental set-up for photovoltaic thermal (PVT) panels. Eindhoven: Technische Universiteit Eindhoven.

Becker, H., & Theis, K. (2016). Sustainable Development in Germany. Wiesbaden: Federal Statistical Office (Destatis).

Conico Valves bv. (2017). Modelling and testing of solar systems with the Thermo-Differential Valve. Veldhoven.

Danfoss. (2018). Data Sheet Thermo. operated water valve AVTA. Retrieved from Danfoss.com: http://files.danfoss.com/technicalinfo/dila/04/IC.PD.500.A8.02.pdf

Duffie, J. A., & Beckman, W. A. (2006). Solar Engineering of Thermal Processes. New Jersey: John Wiley & Sons.

EngineeringToolbox. (2003). Ventilation Ducts - Roughness & Surface Coefficients. Retrieved from The Engineering Toolbox: https://www.engineeringtoolbox.com/surface-roughness-ventilation-ducts-d_209.html

Eternal Sun B.V. (2015). Calibration report Eternal Sun solar simulator. Eternal Sun B.V.

Eternal Sun B.V. (2018). Mail communication about spectral mismatch of the solar simulator.

European Commission. (2017). Renewable energy: Moving towards a low carbon economy. Retrieved from European Commission: Commission and its priorities: https://ec.europa.eu/energy/en/topics/renewable-energy

Grundfos. (2018). ALPHA2 Auto Adapt Circulatiepomp. Retrieved from Grundfos: https://nl.grundfos.com/products/find-product/ALPHA2.html

Helden, W. v., & Zondag, H. (2015). Chapter 6 Solar Thermal Collectors. Eindhoven: Technische Universiteit Eindhoven.

Huber. (2015). Operating instructions Unichiller 015-H-MPC. Offenburg: Peter Huber Kältemaschinenbau GmbH.

Huijzer, M. (2018, May). Error analysis thermocouples. (M. v. Duijnhoven, Interviewer)

IEA. (2015). SHC Task 54 Price Reduction of Solar Thermal System. Retrieved from Solar Heating & Cooling Programme of International Energy Agency: http://task54.iea-shc.org/description

Kemenade, E. v. (2015). Chapter 3 Heat Exchangers. Eindhoven: Technische Universiteit.

Klerk, F. d. (2018, January). Experiment PVT panels on old experimental setup. (M. v. Duijnhoven, Interviewer)

Kratz, P. (2018). 24 hour Measurement Data of the CV-system. Veldhoven: Conico Valves bv.

Krohne. (2016). Optiflux 4000 Technical Datasheet. Duisburg: Krohne Messtechnik GmbH

Liu, X., J, Huang, & Mao, Q. (2015). Sensitive Analysis for the Efficiency of a Parabolic Trough Solar Collector Based on Orthogonal Experiment. New York: International Jounal of Photoenergy.

ME Mechanical Team. (2018). Heat Exchanger Analysis. Retrieved from me-mechanical engineering: https://me-mechanicalengineering.com/heat-exchanger-analysis/

Mills, A. F. (2014). Basic Heat and Mass transfer. Harlow: Clays Ltd, St Ives plc.

NEN-EN-ISO. (2013). NEN-EN-ISO 9806 Zonne-energie Thermische Zonnecollectoren Beproevingsmethoden (ISO 9806:2013,IDT). Delft: NEN-EN-ISO.

Riffat, S., Zhao, X., & Doherty, P. (2003). Developing a theoretical model to investigate thermal performance of a thin membrane heat-pipe solar collector. Nottingham: The University of Nottingham.

Rijvers, L. (2018, January). Experiment specifications PVT panels. (M. v. Duijnhoven, Interviewer)

Ruth, N. v. (2017, October). Experiment specifications solar collector. (M. v. Duijnhoven, Interviewer)

Savitkzy, A., & Golay, M. (1964). Smoothing and differntation of data by simplified least square procedures

TESS. (2012). Volume 07 Hydronics Library Mathematical Reference. Madison: TRNSYS18.

TESS. (2012). Volume 10 Solar Library Mathematical Reference. Madison: TRNSYS18.

TRNSYS. (2017). Volume 1 Getting Started. Madison: TRNSYS18.

TRNSYS. (2017). Volume 4 Mathematical Reference. Madison: TRNSYS18

Welty, J., Rorrer, G., & Foster, D. (2015). Fundamentals of Momentum, Heat and Mass Transfer. Singapore: John Wiley & Sons.

Wiltec. (2018). Stainless Steel Heat Exchanger 10 Plates Plate Heat Exchanger 22 kW. Retrieved from Wiltec Wildanger Technik GmbH: https://www.wiltec.de/hrale-stainless-steel-heat-exchanger-10-plates-plate-heat-exchanger-max-22kw.html

Appendixes

Appendix A| Design of Experimental Setup

Appendix A.1 Design of Components

The thermal circuit discussed in paragraph 2.2 consists of 5 major components, namely the thermostatic bath, thermostatic valve, plate heat exchanger, centrifugal pump and flowmeter. This paragraph discusses each of these components on its design procedure and specifications.

Thermostatic Bath

The cooling power (Q) needed for the setup is based on three factors, namely the solar irradiation (I), surface area (A), and collector efficiency (η); Equation A.1 shows the relation between these factors [Mills, 2014][Welty, 2015]. There are two values that can be used as surface area, namely the surface area of the solar simulator and the aperture area of the solar collector.

$$Q_c = I \cdot A \cdot \eta_{col} \quad \text{A.1}$$

The maximum required cooling power was determined using the test area of the solar simulator, which is 1100 x 2000 mm [Eternal Sun B.V., 2015]; this results in an area of 2.2 m^2. The highest solar irradiation setting of the solar simulator is 1,000 W m^{-2} and the collector efficiency was assumed at 0.60, which results in a power output of 1.3 kW. However, the area of a solar collector is normally less than the area of the solar simulator, thus it was assumed that the maximum output is lower than 1.3 kW. For instance, an average solar collector has a surface area of 2 m^2, which results in a power output of 1.2 kW.

A similar result was found in a previous experiment [Klerk, 2018]. In this experiment, a PVT panel with a continuous flow of 42 L hr^{-1} was used that resulted in a temperature difference of 25 °C. The heat gain in the PVT-panel was determined using equation A.2, using the density and thermal heat capacity of water; this resulted in a heat gain of 1.2 kW.

$$Q_t = \dot{v} \cdot \rho \cdot c_p \cdot \Delta T \quad \text{A.2}$$

The thermostatic bath used in the experimental setup of [Balkom, 2015] was the Unichiller 015-H-MPC of manufacturer Huber, which has a cooling capacity of 1.5 kW at a temperature of 15 °C [Huber, 2015]. However, at a temperature of 7.5 °C the cooling power is reduced to 1.2 kW. Based on an average collector area of 2.0 m^{-2}, the minimum temperature of 10 °C is feasible.

Thermostatic Valve

A thermostatic water valve is used for mechanical flow regulation based on a desired temperature setting; figure A.1 shows an overview an overview of the Danfoss AVTA thermostatic valve. This valve consists of three components: (1) a component for controlling the temperature input, (2) a component for autonomic regulation of the flow, and (3) a temperature sensor. The temperature sensor is installed at the location where the temperature is to be controlled. If there is a change in temperature noticed at the sensor, the internal pressure of the sensor changes, causing a force to exert on the bellows of the valve. A counterforce is created through a spring when a temperature setting is given in component 1. If there is a balance between the pressure force and the counterforce, the valve spindle remains in position; otherwise the spindle moves until a new balance is found or the valve is fully open or closed. Imbalance of forces occurs when the temperature changes at the sensor or if another temperature input is given.

The Danfoss AVTA 15 with adsorption charge was chosen as thermostatic valve in the experimental setup. In an adsorption charge thermostatic valve, when the temperature changes at the temperature sensor, the adsorption of active carbon

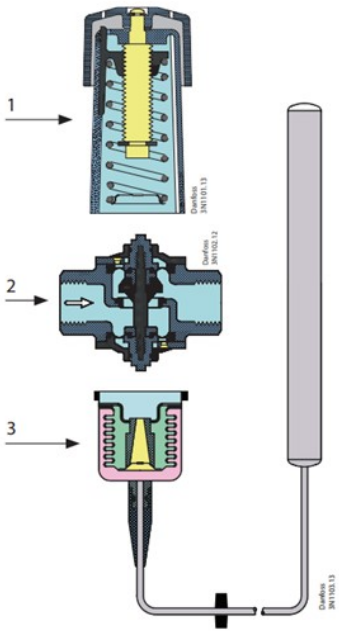

Figure A.1 — Schematic overview of the Danfoss AVTA thermostatic valve [Danfoss, 2018]. 1) setting knob, reference spring and setting scale, 2) valve body with orifice, closing cone and setting elements, and 3) hermetically sealed thermostatic element with sensor, bellow and charge

es at the temperature sensor, the adsorption of active carbon and CO_2 changes, resulting in a pressure difference in component 3. This thermostatic valve has a regulation temperature range of 10 to 80 °C, while the maximum temperature of the sensor is 130 °C. Furthermore, the maximum allowed volume flow velocity through the valve is 1.9 m^3 hr^{-1} and the maximum pressure on the sensor is 25 bar.

Plate Heat Exchanger

A counter flow plate heat exchanger was used in the design of the improved setup. The design of this heat exchanger is dependent on the temperatures of the hot and cold stream as well as the maximum heat for exchange. Figure A.2 shows the temperature profile of the hot and cold stream along the length of the heat exchange surface in a counter flow heat exchanger. As can be seen, the temperature difference at x = L (ΔT_1) is dissimilar to the difference at x = 0 (ΔT_2), because the energy capacity is also dependent on the volume flow of the cold and hot stream, equation A.2.

As mentioned in before, it was assumed that the maximum heat gain was approximately 1.2 kW. The lowest solar collector input temperature is 10 °C (hot stream) and the cold stream inlet is assumed at 7.5 °C. The volume flow of the solar collector cycle is between 20 and 360 liters per hour, according to paragraph 2.1, and the volume flow of the cooling cycle was assumed at 600 liters per hour. The temperature outlet of the hot and cold flow was determined using Equation A.2, in combination with the density and heat capacity of water, and had a value of respectively 62.6 °C and 9.2 °C.

The design of a heat exchanger is defined by the heat conduction coefficient (k) of its material, wall thickness (L), and heat exchange surface. The heat exchanger in the setup is made of stainless steel (AISI 304), which has a heat coefficient of 16.2 W $m^{-1}K^{-1}$. The wall thickness of the heat exchanger is between 0.5 and 1.2 mm. The relation between these parameters is shown in Equation A.3 [Kemenade, 2015].

$$A = \frac{Q}{\frac{k}{L}\,\Delta T_{LM}} \qquad \text{A.3}$$

The definition of the logarithmic mean temperature difference (ΔT_{LM}) is described in Equation A.4 [Kemenade, 2015]; temperatures are defined at length x = L and x = 0.

$$\Delta T_{LM} = \frac{(T_H - T_C)_L - (T_H - T_C)_0}{Ln\left(\frac{(T_H - T_C)_L}{(T_H - T_C)_0}\right)} \qquad \text{A.4}$$

A value of 16.61 for ΔT_{LM} was found using the values for the temperature input and output of both streams as described above. As a result, the required heat transfer surface

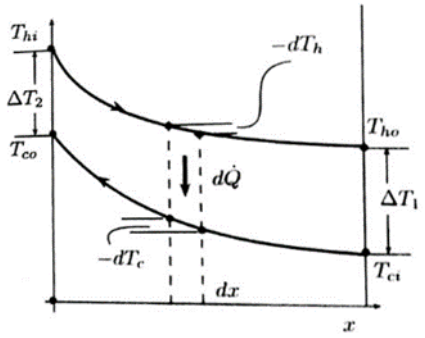

Figure A.2 — Temperature profile of the cold and hot stream versus the length of the heat exchange surface in a counter flow heat exchanger [ME Mechanical Team, 2018]

Table A.1 — Specifications of the plate heat exchanger [Wiltec, 2018]

Parameter		Value
Effective heat exchange surface	[m^2]	0.12
Maximum Power	[kW]	22
Maximum pressure	[bar]	20
Maximum volume flowrate	[m^3 h^{-1}]	4
Plate number	[-]	10
Temperature range	[°C]	-195 to 225
Volume	[L]	0.18

is between 2.2 and 5.35 10^{-3} m^2 and these values are significantly smaller than the surface area of the plate heat exchanger used in the experimental setup, which is 0.12 m^2; more specifications of the plate heat exchanger are shown in Table A.1.

Pump

Finding an appropriate continuous pump for low volume flows is challenging as most circulation pumps are designed for high flows. The pump should have enough capacity to overcome pressure losses that are present in this setup and close to the required maximum volume flow required of 360 liter per hour is required. There are two forms of pressure losses in the experimental setup, namely losses through friction in the piping, and difference in height. The pressure losses (Δp) in the piping was determined using the Darcy-Weisbach equation: Equation A.5.

$$\Delta p = f\frac{L}{D}\frac{\rho}{2}v^2 \qquad \text{A.5}$$

The friction factor (f) is dependent whether there is a turbulent or laminar flow in the piping. Therefore, the Reynolds number (Re) is determined using Reynolds definition

(Equation A.6). A volume flow of 6 L min^{-1} was pumped through the pipe-network that consists of both copper piping and PVC tubing, having inner diameters of respectively 10 mm and 13 mm, resulting in velocity (v) of 1.27 m s^{-1} and 0.75 m s^{-1}. When using the density and dynamic viscosity of water (1000 kg m^{-3}, 0.00089 kg m^{-1} s^{-1}), the Reynolds number was calculated for each of these pipes: an Re of 12,712 for the copper pipes and an Re of 9,779 for the PVC pipes. Both numbers are significantly higher than 2300, meaning that a turbulent flow is present in the complete pipe-network.

$$Re = \frac{\rho v D}{\mu} \quad \text{A.6}$$

Due to the fact that a turbulent flow is present in the piping, the friction factor was determined using the Colebrook interpolation equation: Equation A.7. This friction factor is related to the Reynolds number, the inner diameter and the roughness of the material (e); the roughness of copper is 2 µm and of PVC 7 µm [Engineering Toolbox, 2003]. As a result, the friction factor of the copper piping is 0.029 and of the PVC tubing 0.031.

$$\frac{1}{\sqrt{f}} = -2\log\left(\frac{1}{3.7}\frac{e}{D} + \frac{2.51}{Re\sqrt{f}}\right) \quad \text{A.7}$$

Assuming lengths of 4 m and 6 m for the copper and PVC piping result in pressure losses of 0.095 and 0.042 bar, respectively, using Equation A.5. In addition, a height difference of 1.5 m, resulting in a pressure loss of 0.15 bar, leaving the total pressure to be 0.287 bar. As the pipe bends were not included in the calculation, a safety margin of 10% was used as compensation, thus, a total of 0.316 bar. Based on this knowledge the Grundfos Alpha 2 25-40 Auto Adapt Circulation pump was used, because this pump has a higher capacity (approximately 0.42 bar) than needed in the experimental setup, Figure A.3. Table 2.3 shows an overview of the specifications of this pump.

Flowmeter

A magnetic flowmeter was used in the experimental setup because of its high accuracy, absence of moving parts and flow obstructions in the measurement unit [Almond, 2018]. This type of flowmeter uses Faraday's law of electromagnetic induction for determining the volume flow [Krohne, 2016], Equation A.8, in which the relation between the voltage (U) and the mean flow velocity ($\bar{v}$), magnetic field strength (B), and inner diameter of the flowmeter (D) is described. A correction factor (κ) is needed to correct for the geometry of the flowmeter.

$$U = \bar{v}\,\kappa\,B\,D \quad \text{A.8}$$

Table A.2 — Specifications of the Grundfos Alpha 2 25-40 Auto Adapt Circulation pump [Grundfos, 2018]

Parameter		Value
$\dot{V}_{max}$	[L hr^{-1}]	2400
$T_{fluid,\ range}$	[°C]	2 – 110
$T_{a,\ range}$	[°C]	0 – 40
P	[-]	230 V, 50/60 Hz
p_{max}	[bar]	10

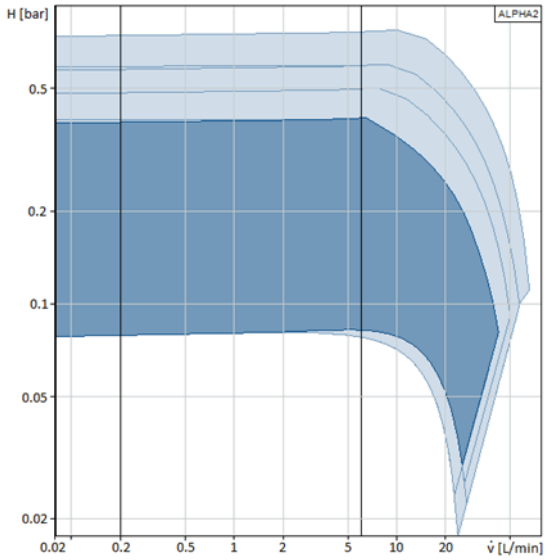

Figure A.3 — Pump curves bar from the Grundfos Alpha 2 25-40 Auto Adapt Circulation pump [Grundfos, 2018]

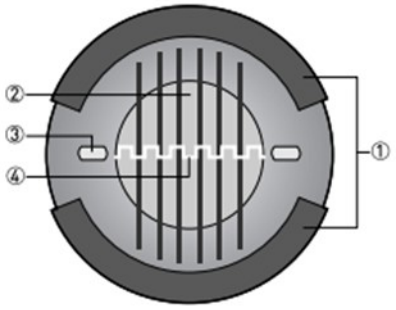

Figure A.4 — Schematic overview of the measuring principle of a magnetic flowmeter. It shows the location of the field coils (1), magnetic field (2), electrodes (3), and the induced voltage, which is proportional to the flow velocity (4) [Krohne, 2016]

A pair of field coils produces a current for inducing a magnetic field through which an electrically conductive fluid flows. Because the pipe is electrically insulated, a voltage signal is generated inside the fluid and subsequently transported to electrodes at the side of the pipe. According to Faraday's law, this signal is related to the mean velocity and thus the flow rate through the pipe. This principle and location of the components is shown in Figure A.4. A signal converter is installed for increasing the voltage signal, filtering and converting it into a signal for data analysis.

The experimental setup contains the magnetic flowmeter Optiflux4000 connected to an IFC100 signal converter from the manufacturer Krohne. This flowmeter has a measuring range of -12 to 12 m s^{-1} and a nominal diameter of 6 mm, which results in a volume flow measuring range of 0 to 6 L min^{-1}. The process temperature range spans from -40 to 120 ° C, while the ambient temperature ranges from -40 to 65 °C. The measuring accuracy is 0.4% of the measurement value; the calibration report of the flowmeter and datasheet of the converter are provided in Appendix A.2.

Appendix A.2 Datasheet Flowmeter

KROHNE

Calibration Certificate - Kalibrierzertifikat - Certificat d'étalonnage
DIN 55 350-18-4.2.2

Customer / Kunde / Client	:	**Technische Universiteit Eindhoven**
Customer Order / Bestellnummer / Commande Client	:	**30042413-353220**
Product / Produkt / Produit	:	
Type / Typ / Type	:	**OPTIFLUX 4000 DN 6 mm/ 1/4 inch**
Sales Order / VK-Auftrag / Commande de vente	:	**240018504 10 1**
Serial Number / Seriennummer / Numéro de série	:	**A18020643**
Tag Number / Tagnummer / Repère	:	

Calibration Method / Kalibriermethode / Méthode d'étalonnage

The flow sensor has been calibrated against a piston-prover. The calibration certificate of this prover registers the traceability to national standards, which establishes the physical units of measurements according to the International System of Units (SI).

Die Prüfung des Durchflussmessgeräts erfolgt im Vergleich zu einem Piston-Prover. Die Kalibrierung des Provers ist rückführbar auf Nationale Standards. Die physikalischen Einheiten sind nach dem SI-System definiert.

Le capteur de mesure a été étalonné avec un piston étalon. Le certificat d'étalonnage de cet étalon prouve la traçabilité aux étalons nationaux qui utilisent des unités de mesures physiques selon le Système International (SI).

Test Equipment Data / Kalibrierstanddaten / Données du banc d'étalonnage

Serial Number / Seriennummer / Numéro de série	:	PST A09	
Calibration fluid / Kalibrierflüssigkeit / Fluide d'étalonnage	:	Water / Wasser / Eau 21.37	°C
Uncertainty / Unsicherheit / Incertitude	:	0.02 %	

Calibration Results / Kalibrier Resultats / Résultats d'étalonnage

Flow Rate Durchflussmenge Débit (%)	Set Flow rate Gewählte Durchfluss Débit réglé (m3/h)	Deviation Abweichung Ecart (%)
97.71	0.1989	-0.05
49.06	0.0999	+0.05

Calibration Data / Kalibrierdaten / Données d'étalonnage

GK : 0.0000 GKh : L1 :
GKl : 8.8104 GK070 : 0.0000 L2 :
L3 :

Date / Datum / Date : 2018-02-26 Signature / Unterschrift / Signature :

KROHNE Altometer, 3313LC12 Dordrecht, Nederland, Tel.:+31 (0)78 6306 300, Fax.:+31 (0)78 6306 390, www.KROHNE.com

Converter parameter datasheet

Converter type : IFC 100 S/N : A18020643

	C1.1	calibration
C1.1.1	zero calibration	-0.00388 m/s
C1.1.2	size	6 mm 1/4inch
C1.1.5	GKL	8.8104
C1.1.7	coil resistance Rsp	35.45 Ohm
C1.1.8.1	calib. coil temp.	+20.0 °C
C1.1.8.2	calib. coil temp.	35.45 Ohm
C1.1.9	density	1.000 kg/L
C1.1.10	target conduct.	400 µS/cm
C1.1.11	EF electr. factor	0.97 mm
C1.1.13	field frequency	1/6*line frequentie
C1.1.14	select settling	Standard
C1.1.16	line frequentie	50Hz
	C2.1	hardware
C2.1.1	terminals A	current output
C2.1.3	terminals C	status output
C2.1.4	terminals D	pulse output
	C2.2	current out A
C2.2.1	range 0% … 100%	4.0 … 20.0 mA
C2.2.2	extended range	3.8 … 20.5 mA
C2.2.3	error current	21.5 mA
C2.2.4	error condition	error in device
C2.2.5	measurement	volume flow
C2.2.6	range	+0 … +6 L/min
C2.2.7	polarity	absolute value
C2.2.8	limitation	-120 … +120 %
C2.2.9	low flow cutoff	2.0 ± 1.0%
C2.2.10	time constant	3.0 s
C2.2.11	special function	off
C2.2.15	4mA trimming	4.0000 mA
C2.2.16	20mA trimming	20.000 mA
	C2.5	pulse output D
C2.5.1	pulse shape	Symmetric
C2.5.3	max. pulse rate	100 Hz
C2.5.4	measurement	volume flow
C2.5.5	pulse value unit	L
C2.5.6	value p. pulse	1 L
C2.5.7	polarity	absolute value
C2.5.8	low flow cutoff	0 ±0 L/min
C2.5.9	time constant	0.0 s
C2.5.10	Invert signal	off
	C5.1	device info
C5.1.1	Tag	18020643
C5.1.2	C number	CG10041100
C5.1.3	device serial no.	A18020643
C5.1.4	electronic serial no.	104622349
C5.1.6	Electronic Revision ER	ER3.1.5_

Appendix B| Experimental Research

Appendix B.1 Determining the Optical Efficiency and the Heat Loss Coefficients

Due to the three measurement datapoints in the inlet temperature analysis, there are three efficiency equations according to the theoretical model discussed in Chapter 3, equation B.1 - B.3.

$$\eta_1 = \eta_0 - a_1\frac{x_1}{y_1} - a_2\frac{x_1|x_1|}{y_1} \quad \text{B.1}$$

$$\eta_2 = \eta_0 - a_1\frac{x_2}{y_2} - a_2\frac{x_2|x_2|}{y_2} \quad \text{B.2}$$

$$\eta_3 = \eta_0 - a_1\frac{x_3}{y_3} - a_2\frac{x_3|x_3|}{y_3} \quad \text{B.3}$$

The process of determining the heat loss coefficients and the optical efficiency using these equations is determined in this Appendix. First equation B.1 is rewritten as function of optical efficiency, equation B.4.

$$\eta_0 = \eta_1 + a_1\frac{x_1}{y_1} + a_2\frac{x_1|x_1|}{y_1} \quad \text{B.4}$$

Equation B.4 is used in equation B.2 to acquire equation B.5, from which the quadratic heat loss coefficient can rewritten as function of the linear heat loss coefficient, equation B.6.

$$\eta_2 = \eta_1 + a_1\frac{x_1}{y_1} + a_2\frac{x_1|x_1|}{y_1} - a_1\frac{x_2}{y_2} - a_2\frac{x_2|x_2|}{y_2} \quad \text{B.5}$$

$$a_2 = \frac{\eta_2 - \eta_1 - a_1\left(\frac{x_1}{y_1} - \frac{x_2}{y_2}\right)}{\frac{x_1|x_1|}{y_1} - \frac{x_2|x_2|}{y_2}} \quad \text{B.6}$$

Afterwards, equation B.4 and B.6 were used to rewrite equation B.3 as a function of the linear heat loss coefficient, equation B.7.

$$\eta_3 = \eta_1 + a_1\frac{x_1}{y_1} + \frac{\eta_2 - \eta_1 - a_1\left(\frac{x_1}{y_1} - \frac{x_2}{y_2}\right)}{\frac{x_1|x_1|}{y_1} - \frac{x_2|x_2|}{y_2}}\frac{x_1|x_1|}{y_1} - a_1\frac{x_3}{y_3} - \frac{\eta_2 - \eta_1 - a_1\left(\frac{x_1}{y_1} - \frac{x_2}{y_2}\right)}{\frac{x_1|x_1|}{y_1} - \frac{x_2|x_2|}{y_2}}\frac{x_3|x_3|}{y_3} \quad \text{B.7}$$

Lastly, equation B.7 may be rewritten as function of the linear heat loss coefficient, equation B.8. This function is only dependent on measurement values obtained in Chapter 3.

$$a_1 = \frac{\eta_3 - \eta_1 - \frac{(\eta_2 - \eta_1)\frac{x_1|x_1|}{y_1}}{\frac{x_1|x_1|}{y_1} - \frac{x_2|x_2|}{y_2}} + \frac{(\eta_2 - \eta_1)\frac{x_3|x_3|}{y_3}}{\frac{x_1|x_1|}{y_1} - \frac{x_2|x_2|}{y_2}}}{\frac{x_1}{y_1} - \frac{\left(\frac{x_1}{y_1} - \frac{x_2}{y_2}\right)}{\frac{x_1|x_1|}{y_1} - \frac{x_2|x_2|}{y_2}}\frac{x_1|x_1|}{y_1} - \frac{x_3}{y_3} + \frac{\left(\frac{x_1}{y_1} - \frac{x_2}{y_2}\right)}{\frac{x_1|x_1|}{y_1} - \frac{x_2|x_2|}{y_2}}\frac{x_3|x_3|}{y_3}} \quad \text{B.8}$$

Appendix B.2 Solar Keymark Certificate

CERTIFIKAT

Solar Keymark Certificate
No. SP SC0175-15

Holder/Issued to

Company: TWL Technologie GmbH
Address: Im Gewerbegebiet 8-12, 92271 Freihung, Germany

Product name and description

Vacuum tube thermal solar collectors for water heating. For technical information see Appendix (2 pages).

Models:	**TWL HLK20, TWL HLK30**

Certificate

The product mentioned above is found to comply with requirements in EN 12975-1:2006+A1:2010 and the Specific CEN Keymark Scheme Rules for Solar Thermal Products, and are based on test results according to ISO 9806:2013.

Marking

Products conforming to this certificate shall be marked in accordance with the requirements in the Specific CEN Keymark Scheme Rules for Solar Thermal Products. The marking shall, together with the Keymark logo, show the identification code of the empowered certification body (SP Technical Research Institute of Sweden, No. 012), also see CEN-CENELEC Internal Regulations Part 4 Certification, Annex A.

Validity

This certificate is valid until 2020-01-28 provided that the conditions in the Solar Keymark Rules are fulfilled and the standard or rules are not modified significantly. The validity of the certificate can be checked in the database, see Solar Keymark website http://www.solarkeymark.org

Miscellaneous

The manufacturer's factory production control procedures are under surveillance by the responsibility of SP. This is the first version of this certificate.

Borås, Sweden 2015-04-21

SP Technical Research Institute of Sweden
Certification

Lennart Aronsson
Product Certification Manager

Susanne Hansson
Certification Officer

SWEDAC ACKREDITERING 1002 EN 45 011

012

SP Technical Research Institute of Sweden
Postal address: SP, Box 857, SE-501 15 Borås, SWEDEN
Phone / Fax: +4610 516 50 00, +4633 13 55 02
Reg.number: 556464-6874
E-mail / Internet: info@sp.se, www.sp.se

Annex to Solar Keymark Certificate

Page 1/2

Summary of ISO 9806 Test Results		Licence Number	SP SC0175-15
		Issued	2015-04-21

Company holding the	TWL Technologie GmbH	Country	Germany
Brand (optional)	HLK20	Website	www.twl-technologie.de
Street, street number	Im Gewerbegebiet 8-12	E-mail	vertrieb@twl-technologie.de
Postal Code / City, province	D-92271 Freihung	Tel/Fax	+49 04351-75 17 00

Collector Type (flat plate glazed/un-glazed; evacuate tubular)	Evacuated tubular collector
Thermal / photo voltaic hybid collector? (PVT collector)	No
Integration in the roof possible ? (manufacturers declaration)	No

Collector name	Aperture area (Aa)	Gross length	Gross width	Gross height	Gross area (AG)	Power output per collector module G = 1000 W/m², Tm-Ta 0 K	10 K	30 K	50 K	70 K
	m²	mm	mm	mm	m²	W	W	W	W	W
TWL HLK20	1.86	1 953	1 550	151.5	3.03	1 415	1 371	1 270	1 155	1 025
TWL HLK30	2.78	1 953	2 300	151.5	4.49	2 116	2 049	1 899	1 727	1 532

Performance test method	Glazed liquid heating collector - steady state - outdoor			
Performance parameters related to aperture	η0	a1	a2	
Units	-	W/(m²K)	W/(m²K²)	
Test results - Flow rate and fluid see note 1	0.761	2.299	0.010	

Bi-directional incidence angle modifiers? Yes	*Kϑ values are obligatory for 50°.*									
Incidence angle modifiers Kθ(θT)	Angle	10°	20°	30°	40°	50°	60°	70°	80°	90°
transversal direction	Kθ(θT)	--	1.03	--	1.19	--	1.31	--	--	0.00
Incidence angle modifiers Kθ(θL)	Angle	10°	20°	30°	40°	50°	60°	70°	80°	90°
longitudinal direction	Kθ(θL)	--	--	--	--	0.90	--	--	--	0.00

Stagnation temperature - Weather conditions see note 2	Tstg	228.5	°C
Effective thermal capacity	ceff = C/Ag	4.38	kJ/(m²K)
Max. intende operation temperature - see note 3	Tmax,op	120	°C
Max. operation pressure - see note 3	pmax,op	700	kPa

Pressure drop table - for a collector family, the values shall be for the module with highest ΔP per m² aperture area

Flow rate	kg/(s m²)	0.005	0.010	0.015	0.020	0.025	0.030				
Pressure drop, ΔP	Pa	663	1705	3263	5257	7699	10602				

Optional weather data	Location		Link
Testing Laboratory	Intertek Testing Services Shenzhen Ltd. Guangzhou Branch		
Website	www.intertek.com		
Test report id. number	140605032GZU-001	Date of test report	2014-12-18

During the test GDIF/GTOT was always between 0.11 and 0.22

Comments of testing laboratory:

Aperture area, referenced to above, is according to definition in ISO 9488:2008.

Note 1	Flow rate	0.020 kg/(s m²)	Fluid	Water	
Note 2	Irradiance, G = 1000 W/m²; Ambient temperature , Ta=30 °C				
Note 3	Given by manufacturer				

5P02115/OBL1018-14 Datasheet version: 4.06, 2014-01-15

Test lab: Intertek Testing Services Shenzhen Ltd. Guangzhou Branch
Block E, No.7-2 Guang Dong Software Science Park, Caipin Road, Guangzhou Science City,GETDD, Guangzhou, China.
Telephone: 86 20 82139688

SP 302

Annex to Solar Keymark Certificate

Annual collector output based on ISO 9806 Test Results, annex to Solar KEYMARK Certificate	Licence Number	SP SC0175-15
	Issued	2015-04-21

Annual collector output kWh/module

	Location and collector temperature (Tm)												
	Athens			Davos			Stockholm			Würzburg			
Collector name	25°C	50°C	75°C	25°C	50°C	75°C	25°C	50°C	75°C	25°C	50°C	75°C	
TWL HLK20	2 468	2 010	1 561	2 007	1 593	1 208	1 466	1 124	829	1 581	1 213	882	
TWL HLK30	3 688	3 004	2 333	3 000	2 381	1 805	2 191	1 680	1 238	2 363	1 812	1 319	

Collector mounting: Fixed or tracking	Fixed; slope = latitude - 15° (rounded to nearest 5°)

Overview of locations

Location	Latitude °	Gtot kWh/m²	Ta °C	**Collector orientation or tracking mode**
Athens	38	1 765	18.5	South, 25°
Davos	47	1 714	3.2	South, 30°
Stockholm	59	1 166	7.5	South, 45°
Würzburg	50	1 244	9.0	South, 35°

Gtot	Annual total irradiation on collector plane	kWh/m²
Ta	Mean annual ambient air temperature	°C
Tm	Constant collector operating temperature (mean of in- and outlet temperatures)	°C

The calculation of the annual collector performance is performed with the official Solar Keymark spreadsheet tool ScenoCalc. The collector output is calculated hour by hour according to the efficiency parameters from the Keymark test using constant collector operating temperature (Tm). A detailed description of the calculations is available at http://www.sp.se/en/index/services/solar/ScenoCalc/Sidor/default.aspx.

Certification Body:
SP Technical Research Institute of Sweden Box 857, 501 15 Borås, Sweden
www.sp.se info@sp.se tel +4610 516 5000

Datasheet version: 4.06, 2014-01-15
ScenoCalc version: Ver. 4.06 (Jan, 2014)

SP 302

Appendix C| Numerical Research

Appendix C.1 TASK54 Reference Model Datasheet

TASK 54

SHC SOLAR HEATING & COOLING PROGRAMME INTERNATIONAL ENERGY AGENCY

Reference solar combi system Germany

INFO Sheet A09

Description:	*Definition of reference solar combi system, Germany*
Date:	23.03.2018, revised 31.05.2018 V7: lifetime 25 y (boiler 15 y)[1]
Authors:	Stephan Bachmann (ITW Stuttgart), Stephan Fischer (ITW Stuttgart), Bernd Hafner (RHC-Platform)
Download possible at:	http://task54.iea-shc.org/

Introduction

This document describes the reference solar combisystem for domestic hot water preparation and space heating in Germany. The system is modelled with TRNSYS to calculate the fuel consumption and electric energy needed to provide the required domestic hot water and space heating as well as the substituted fuel provided by the combisystem. Using this result the levelized costs of heating (LCOH) for the substituted fuel is calculated using eq. 1 and the reference costs for the investment of the system, installation costs, fuel and electricity costs.

Hydraulic Scheme of the System

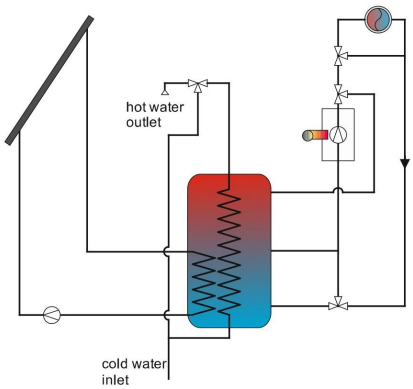

Key data	
Collector area	15 m²
Heat store volume	800 l
Location	Germany, Würzburg
Hemispherical irradiance on horizontal surface	$\Sigma G_{hem,hor}$ =1118.8 kWh/(m² a)
Lifetime of system	25 years Boiler exchange after 15 years

Levelized Cost of Heat (LCoH)

LCoHs solar part without VAT	**0.178 €**
LCoHc conventional part without VAT	**0.127 €**
LCoHo complete system without VAT	**0.137 €**

1

TASK 54

SHC SOLAR HEATING & COOLING PROGRAMME INTERNATIONAL ENERGY AGENCY

Reference solar combi system Germany

INFO Sheet A09

Details of the System

Location	Germany, Würzburg
Type of system	Combisystem
Weather data including - hemispherical irradiance on horizontal surface - beam irradiance on horizontal surface - diffuse irradiance on horizontal surface - ambient temperature in hourly values	Test reference year (TRY Würzburg) $\Sigma G_{hem,hor}$ =1118.8 kWh/(m^2 a) $\Sigma G_{beam,hor}$ = 550.1 kWh/(m^2 a) $\Sigma G_{diff,hor}$ = 568.7 kWh/m^2 a) $T_{amb,av}$ = 9.0 °C
Collector orientation - collector tilt angle to horizontal - south deviation of collector - ground reflectance - resulting hemispherical irradiance on tilted surface	 45 ° south = 0° 0.2 $\Sigma G_{hem,tilt}$ =1229.8 kWh/(m^2 a)
Load information including - heat demand space heating - tapping profile - store heat losses - tapping temperature - average inlet temperature of cold water - cold water inlet temperature amplitude	 9090 kWh/a /1/ EU-tapping profile L (4254 kWh/a) /2/ 2041 kWh 55°C according EU tapping profile 10°C 0 K
Collector information based on gross area	**TRNSYS-type 132**
Number of collectors	6
Collector area of one collector	2.5 m²
Maximum collector efficiency	0.684
Incidence angle modifier for direct irradiance b_0	0.2
Incidence angle modifier for diffuse Irradiance	0.91
Linear heat loss coefficient	3.51 W/(m²K)
2nd order heat loss coefficient	0.011 W/(m²K²)
Effective heat capacity	8.0 kJ/(m²K)
Heat store parameters	**TRNSYS-type 340**
Heat store volume	800 l
Auxiliary volume for DHW preparation	424 l
Store inner diameter	0.79
Rel. height of solar inlet	0.4
Rel. height of solar outlet	0.04
Rel. height of auxiliary inlet	0.9
Rel. height of auxiliary outlet	0.47
Rel. height of space heating inlet	0.2
Rel. height of space heating outlet	0.45
Rel. height of cold water inlet	0.05

2

TASK 54

SHC SOLAR HEATING & COOLING PROGRAMME INTERNATIONAL ENERGY AGENCY

Reference solar combi system Germany

INFO Sheet A09

Rel. height of hot water outlet	0.95
Rel. height of sensor for aux. charging	0.6
Rel. height of sensor for space heating preheating	0.45
Rel. height of sensor for collector loop	0.2
set temperature for DHW	62.5 °C
Temperature difference space heating preheat on	4 K
Temperature difference space heating preheat off	2 K
Overall heat loss capacity rate of store	4.4 W/K
Effective vertical conductivity	1.2 W/(mK)
Heat transfer capacity rate of solar loop HX	$(kA)_{WT,Sol} = 165{,}9 \cdot \dot{m}^{0{,}283} \cdot \vartheta_m^{0{,}524}$ [W/K]
Heat transfer capacity rate of hot water HX	$(kA)_{WT,HW} = 75{,}8 \cdot \dot{m}^{0{,}252} \cdot \vartheta_m^{1{,}026}$ [W/K]
Volume solar loop HX	11.8 l
Volume hot water HX	38.5 l
Maximum heat store temperature	90 °C
Ambient temperature of heat store	15 °C
Solar thermal controller and hydraulic piping	
Total pipe length of collector loop	20 m
Inner diameter of collector loop pipe	20 mm
Temperature difference collector start-up	6 K
Temperature difference collector shut-off	4 K
Electric power of solar thermal controller	3 W
Operating hours of solar thermal controller per year	8760 h
Electric consumption of controller per year	26.3 kWh
Electric power of solar loop pump	55 W
Operating hours of solar loop pump	1073 h
Electric consumption of solar loop pump	59 kWh
Electric consumption of other el. components	-
Conventional system	
Type of auxiliary heating	Gas condensing boiler
Boiler capacity	19 kW
Mass flow	1090 kg/h (delT = 15 K)
Efficiency factor of boiler	0.9
Electric power of controller	3 W
Operating hours of controller per year	8760
Electric consumption of controller per year	26.3 kWh
Electric power of pump	55 W
Operating hours of pump (aux. heating + space heating)	3987 h

TASK 54

SHC SOLAR HEATING & COOLING PROGRAMME INTERNATIONAL ENERGY AGENCY

Reference solar combi system Germany

INFO Sheet A09

Electric consumption of pump per year	219 kWh
Investment costs solar thermal system	
Solar thermal collector, heat store, solar thermal controller solar thermal hydraulic components	8000 € /5/
Installation	2000 € /5/
Credit conventional heat store and share of installation	-1000 €
Overall investment costs solar thermal part I_0	9000 €
Investment costs conventional part	
Boiler and heat store	4000 € /3/
Exhaust system	500 € /3/
Installation	1000 € /3/
Installation material	1000 € /3/
Boiler (exchange after 15 y)	2333 € (= 2/3 of new boiler 3500 €)
Installation new boiler	360 €
Installation material new boiler	100 €
Overall investment costs conventional part I_0	9293 €
Overall investment costs complete system I_0	**18293 €**
Operation costs conventional part per year	
Auxiliary heat demand hot water	3743 kWh/a
Fuel demand hot water	4159 kWh/a
Heat demand space heating	7506 kWh/a
Fuel demand space heating	8340 kWh/a
Fuel demand hot water + space heating E_t	12499 kWh/a
Cost per kWh fuel (gas)	0.066 € kWh/a /4/
Fuel costs	825 €/a
Electricity demand	246 kWh/a
Cost per kWh electric energy /4/	0.254 €
Electricity costs	62 €/a
Maintenance costs	200 €/a /3/
Gas meter	130 €/a /3/
Yearly operation and maintenance cost conventional part C_t	1217 €
Operation costs solar part per year	
Electricity demand	85 kWh/a
Cost per kWh electric energy /4/	0.254 €
Electricity costs	22 €/a
Maintenance costs (I_0 * 2%)	180 €/a
Yearly operation and maintenance cost solar part C_t	202 €/a
Fractional energy savings with credit for 150l-	20.2 %

4

TASK 54

SHC SOLAR HEATING & COOLING PROGRAMME INTERNATIONAL ENERGY AGENCY

Reference solar combi system Germany

INFO Sheet A09

Store, UA=2,05 W/K	
Saved final energy (year t) E_t	3162 kWh
Type of incentives	None
Amount of incentives	0 €
Lifetime of system	25 year
Discount rate r	0 %
Inflation rate	0 %
Corporate tax rate TR	0 %
Asset depreciation (year t) DEP_t	0 €
Subsidies and incentives (year t) S_t (considered in I_0)	0 €
Residual value RV	0 €
Discount rate r	0 %
VAT rate	19 %

Calculation of levelized cost LCOH:

$$LCoH = \frac{I_0 - S_0 + \sum_{t=1}^{T} \frac{C_t(1-TR) - DEP_t \cdot TR}{(1+r)^t} - \frac{RV}{(1+r)^T}}{\sum_{t=1}^{T} \frac{E_t}{(1+r)^t}} \quad (1)$$

Where:

$LCoH$: levelized cost of heat in €/kWh
I_0: initial investment in €
S_0: subsidies and incentives in €
C_t: operation and maintenance costs (year t) in €
TR: corporate tax rate in %
DEP_t: asset depreciation (year t) in €
RV: residual value in €
E_t: saved final energy (year t) in kWh
r: discount rate in %
T: period of analysis in year

Annex: Comparison to Figures Published in Solar Heat Worldwide

To compare the above presented LCoHs based on the saved final energy with the $LCoH_{SHWW}$ presented in Solar Heat World Wide based on the collector yield the following table is presented

Collector yield (year t) E_t	4541 kWh
$LCOH_{SHWW}$ solar part without VAT	**0.124 €**

5

TASK 54

SHC SOLAR HEATING & COOLING PROGRAMME INTERNATIONAL ENERGY AGENCY

Reference solar combi system Germany

INFO Sheet A09

References

[1] EN 12977-2 (2012): "*Thermal solar systems and components – Custom built systems – Part 2: Test methods for solar water heaters and combisystems*".

[2] COMMISSION DELEGATED REGULATION (EU) No 812/2013, ANNEX VII.

[3] Hafner, B. (2016): "*E-Mail*". Dated 13.06.2016.

[4] Check24 (2016): "*Würzburg reference costs*". URL: www.check24.com (accessed in Sept. 2016).

[5] Mean values of evaluated invoices, supplied by Bafa.

[6] Louvet, Y., Fischer, S. et. al. (2017): "*IEA SHC Task 54 Info Sheet A1: Guideline for levelized cost of heat (LCoH) calculations for solar thermal applications*". URL: http://task54.iea-shc.org/.

[7] Louvet, Y., Fischer, S. et.al. (2017): "*Entwicklung einer Richtlinie für die Wirtschaftlichkeitsberechnung solarthermischer Anlagen: die LCoH Methode*". Symposium Thermische Solarenergie, Bad Staffelstein.

[1] To avoid confusion with the results of other works ([1], [8], [9]) also using the notion of LCoH for solar thermal systems, new acronyms were introduced in this Info Sheet. As previous studies have considered different assumptions for the definition of the terms of the LCoH equation, it does not make sense to compare the values they obtained with the LCoHs, LCoHc and LCoHo values defined here. A detailed explanation of the differences between the approaches chosen in the framework of IEA-SHC Task 54 and in the Solar Heat Worldwide report [9] can be found in Info Sheet A13 [10].

Appendix C.2 Incidence Angle Modifier of ETSC

TRNSYS-type538 requires the transversal and longitudinal IAM in order to determine the absorbed irradiation in the ETSC. Unfortunately, the data provided in the Solar Keymark, Appendix B.2 was insufficient for the TRSNSYS model. Therefore assumptions had to be made in order to obtain a transversal and longitudinal IAM curve versus the angle of incidence. These assumptions were based on two data sets found in a literature research [Aucklat, 2017] [TriSolar, 2017], which are presented in Table C.1.

The values found in the Solar Keymark were combined with the assumptions based on Table C.1, which are plotted for the transversal IAM and longitudinal IAM in Figure C.1 and C.2, respectively. A sixth order polynomial fit was used to predict the Transversal IAM and Longitudinal IAM curve. The data required from TRNSYS is similar to the data provided in Table C.1, thus the curves were used to acquire values to the according angle, which are shown in Table C.2.

Table C.1 — Transversal and longitudinal IAM found in [Aucklat,2017] and [], which were used to estimate the IAMs for the ETSC used in this research. The marked areas were the values on which assumptions were made, and used in combination with the values presented in the Solar Keymark, to acquire the IAM curves of the ETSC used in this research.

Source	Angle [°]	0	10	20	30	40	50	60	70	80	90
Aucklat	Transversal IAM	1.00	1.02	1.07	1.15	1.28	1.50	1.49	1.29	0.75	0.00
	Longitudinal IAM	1.00	1.00	1.00	0.99	0.97	0.93	0.85	0.71	0.46	0.00
Tri Solar	Transversal IAM	1.00	1.02	1.08	1.18	1.37	1.40	1.34	1.24	0.95	0.00
	Longitudinal IAM	1.00	1.00	0.99	0.98	0.96	0.93	0.87	0.74	0.38	0.00

Table C.2 — Transversal and longitudinal IAM based on Figure C.1 and C.2. The orange marked areas represent the assumptions that were made, while the green marked areas represent the data described in the Solar Keymark.

Angle [°]	0	10	20	30	40	50	60	70	80	90
Transversal IAM	1.00	1.01	1.03	1.10	1.19	1.28	1.31	1.18	0.79	0.00
Longitudinal IAM	1.00	1.00	0.99	0.98	0.96	0.90	0.81	0.62	0.31	0.00

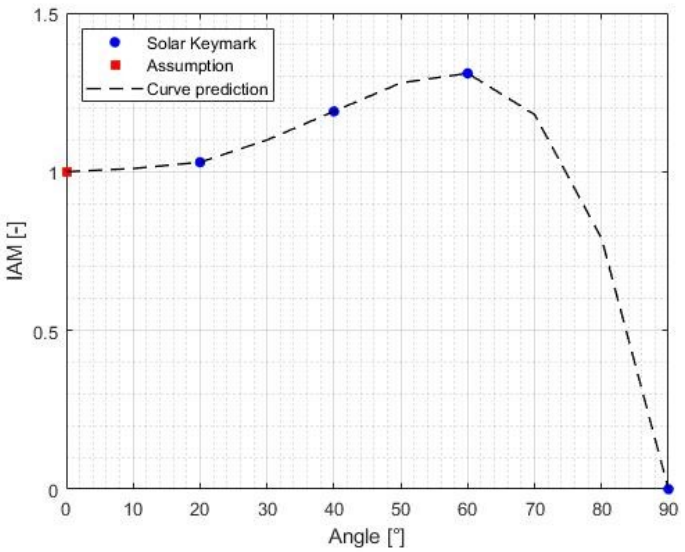

Figure C.1 — Predicted transversal IAM curve based on the Solar Keymark data and assumptions based on [Aucklat, 2017] and [TriSolar, 2017]

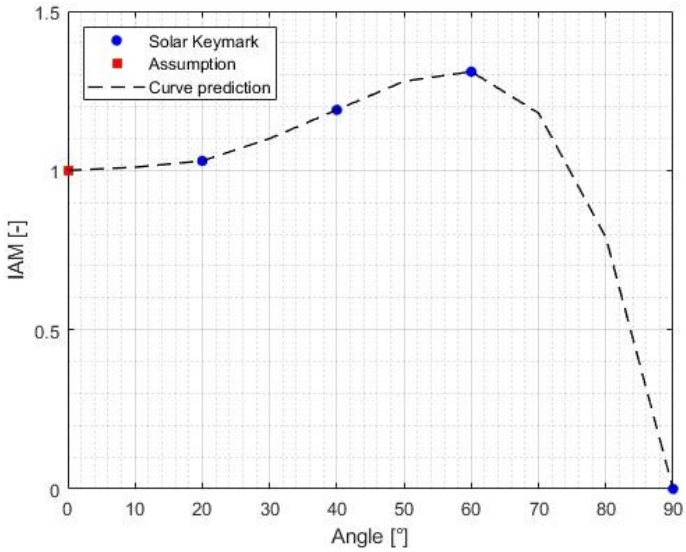

Figure C.2 — Predicted longitudinal IAM curve based on the Solar Keymark data and assumptions based on [Aucklat, 2017] and [TriSolar, 2017]

Appendix C.3 System Component: Piping

Theoretical model

Whether there is a volume flow through a pipe or a stagnant flow, the volume inside the pipe exchanges heat to the pipe and the environment. Figure C.3 show a schematic overview of the pipe and its heat balances. A fist heat balance that occurs in the pipe when the temperature suddenly increases/ decreases is the transfer of heat through the pipe wall, via conduction. The significance of this heat transfer can be determined by the Fourier number (Fo), equation C.1 [Mills, 2014]: if Fo << 1 then there has not been time for conduction to occur in the pipe wall; Fo is a function of the thermal diffusivity (α).

$$Fo = \frac{\alpha t}{L^2} \quad \text{C.1}$$

The Fo was determined for both the pipe wall and the fluid inside the pipe, which also experiences conduction, for different sections in the pipe: at a length of 10, 1, and 0.01 m from the outlet of the pipe. During the calculation, a mass flowrate of 100 kg hr^{-1} was assumed which effects the time needed for the fluid to breach these pipe lengths. Table C.3 presents the values of the Fo, which are << 1, thus there has not been any heat transfer via conduction during these distances. Therefore, the heat transfer via conduction through the pipe and fluid can be neglected.

The pipe wall stores energy ($Q_{p.sto}$), both during a volume flow and stagnant flow, that is based on the heat acquired from the fluid ($Q_{fl->p}$) and heat losses to the ambient ($Q_{p->a}$), Figure C.3b, with the according heat balance, equation C.2.

Table C.3 — Fo values at different lengths from the outlet of the pipe for both the pipe wall and the fluid inside the pipe, $\dot{m}$ = 100 kg hr^{-1}. α_{pipe} = 1.17 10^{-4} m^2 s^{-1} and α_m = 0.155 10^{-6} m^2 s^{-1}.

Parameter		Value
Effective heat exchange surface	[m^2]	0.12
Maximum Power	[kW]	22
Maximum pressure	[bar]	20
Maximum volume flowrate	[m^3 h^{-1}]	4
Plate number	[-]	10
Temperature range	[°C]	-195 to 225
Volume	[L]	0.18

$$Q_{p.sto} = Q_{fl\to p} - Q_{p\to a} \quad \text{C.2}$$

When the pipe is divided into a number of *n* nodes, the stored heat inside the pipe per node can be determined using equation C.3, while the heat gain from the fluid is determined using equation C.4 and heat loss to the ambient via equation C.5.

$$Q_{p.sto.n} = (V\rho c_p)_p \frac{dT}{dt} \quad \text{C.3}$$

$$Q_{fl\to p.n} = UA_{fl}(T_{fl} - T_{p.n}) \quad \text{C.4}$$

$$Q_{p.n\to a} = \frac{1}{R_{ins} + R_{conv}}(T_s - T_a) \quad \text{C.5}$$

As a result, the heat balance can be analytically solved via equation C.6.

$$T_{p.t} = T_{p.(t-1)} + \frac{\left[UA_{fl}(T_{fl} - T_{p.n.(t-1)}) - \frac{1}{R_{ins} + R_{conv}}(T_{p.n.t-1} - T_a)\right]dt}{(V\rho c_p)_p} \quad \text{C.6}$$

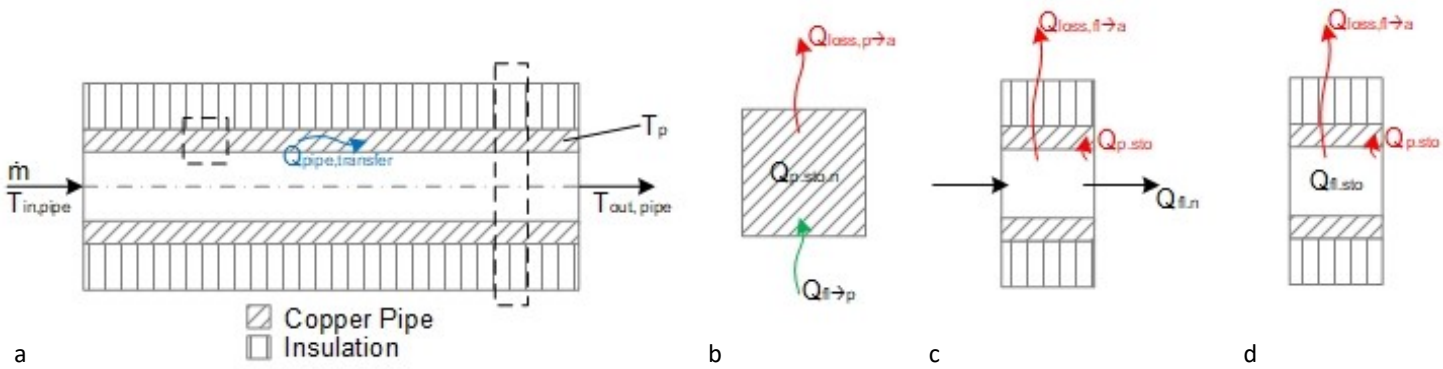

Figure C.3 — Schematic overview of the pipe and the balance in heat transferred through the pipe due to a temperature increase/decrease at the inlet (a), the heat balances in storing heat inside the pipe wall (b), nodal heat balance when a volume flow is applied ©, and the nodal heat balance when there is a stagnant flow (d).

The heat loss of the fluid can either be under influence of a volume flow ($Q_{fl.n}$), Figure C.3c, or a stagnant flow ($Q_{fl.sto}$), Figure C.3d, which has an influence on the general heat balance, equation C.7. The heat loss to the environment ($Q_{fl->a}$) is a function of conduction through the pipe, conduction through the insulation and convection to the environment, equation C.8. The heat balance of the fluid under influence of a volume flow is described in equation C.9, and under influence of a stagnant flow in equation C.10.

$$Q_{fl} = Q_{loss,fl\to a} + Q_{p.sto} \quad \text{C.7}$$

$$Q_{loss,fl\to a} = \frac{1}{R_{ins} + R_{conv} + R_p}\left(T_{fl.n} - T_a\right) \quad \text{C.8}$$

$$Q_{fl.n} = \dot{v}\left(\rho c_p\right)_{fl}\left(T_{in.pipe} - T_{o.pipe}\right) \quad \text{C.9}$$

$$Q_{fl.sto} = V_n\left(\rho c_p\right)_{fl} \quad \text{C.10}$$

Again this heat balance can be solved analytically and for this case two different equations can be found, equation C.11 and C.12.

$$T_{o,pipe} = T_{in,pipe} - \frac{UA_{fl}\left(T_{in,pipe} - T_{s,t-1}\right)}{\dot{v}\left(\rho c_p\right)_{fl}} - \frac{\frac{1}{R_{ins} + R_{conv} + R_p}\left(T_{in,pipe} - T_a\right)}{\dot{v}\left(\rho c_p\right)_{fl}} \quad \text{C.11}$$

$$T_{fl,t} = T_{fl,t-1} + \left[\frac{-UA_{fl}\left(T_{fl,t-1} - T_{s,t-1}\right)}{V_n\left(\rho c_p\right)_{fl}} - \frac{\frac{1}{R_{ins} + R_{conv} + R_p}\left(T_{fl,t-1} - T_a\right)}{V_n\left(\rho c_p\right)_{fl}}\right] dt \quad \text{C.12}$$

Pipe TRNSYS-types

There are three TRNSYS-types available in the standard library and extended TESS library: type 31, 709 and 604. Since type 31 and 709 uses the same numerical model in TRNSYS and type709 allows for specifying the material properties of the pipe and insulation layer, while type31 uses a general heat loss coefficient, thus type31 was left out of the comparison. Figure C.4 plots the simulation results for type 709 and 604 for a sudden change in temperature from 10 to 60 °C under influence of a mass flowrate of 100 kg hr^{-1}, as a result the fluid needs approximately 113 s to reach the outlet of the pipe. As can be seen, TRNSYS-type604 has an increase in temperature before this time and based on the theoretical model this cannot happen as the heat transfer through conduction can be neglected (Fo). In conclusion, TRNSYS type is incapable of accurately simulating a sudden increase in temperature.

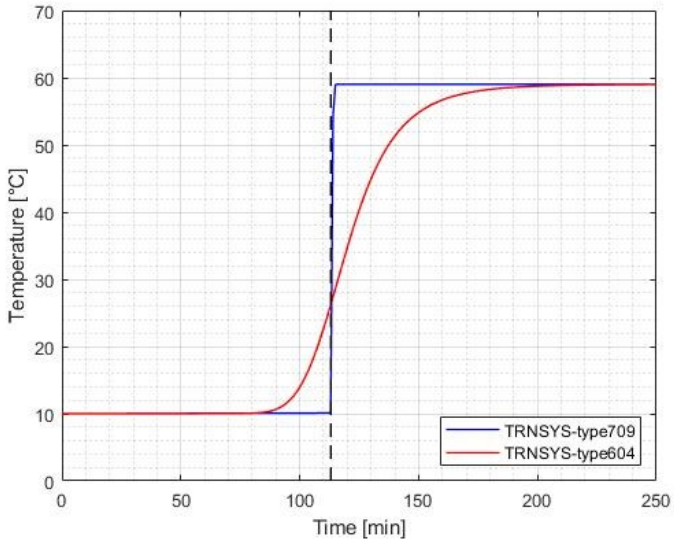

Figure C.4 — Simulation results for TRNSYS-type709 and TRNSYS-type604 when the temperature suddenly increases from 10 to 60 °C, using a mass flowrate of 100 kg hr^{-1}. The time needed for the volume at the inlet of the pipe to reach the outlet of the pipe is approximately 113 s, indicated by the vertical line.

Appendix C.4 System Component: Thermal Storage

The theoretical model of the storage tank is similar to the numerical model of the TRNSYS-type. Based on this numerical model in combination with the neglection of conduction between nodes, the storage tank can be analytically solved for its charge behavior, equation C.13. As a result of the similar equation between theoretical model and numerical model, similar temperature profiles were observed, Figure C.5 and C.6; the difference comes from the assumption made in the theoretical model.

The influence of number of nodes was determined by acquiring the temperature difference (ΔT) between the top of the storage tank and the bottom of the storage tank, presented in Figure C.7, and the inlet energy profile, shown in Figure C.8; TRNSYS-type158 has a maximum allowed number of nodes of 50. As can be seen in Figure C.7, the higher the number of nodes thus the more direct is the increase in ΔT at the start of the simulation. This means that $T_{in,st}$ increases the temperature in the top node at the start of the simulation, while the temperature in the bottom node remains unaffected. Also, a higher number of nodes results in a longer period where ΔT_{max} is achieved. In contrast, using 5 nodes result in a ΔT far below the ΔT_{max}. Furthermore, it can be seen that a high number of nodes will eventually have a rapid decrease in ΔT. Because TRNSYS-type158 is a constant volume storage tank, the hot fluid at the inlet displaces the volume inside the tank and as a consequence, a colder volume at the bottom is displaced to the outlet. Thus, the bottom node increases its temperature with the node above. From this data can be concluded that a higher number of nodes results in a higher degree of stratification.

This higher degree of stratification has an influence on the inlet energy, as can be seen in Figure C.8. As a consequence, a high degree of stratification has a long period of maximum inlet energy that rapidly decreases to a limited inlet energy. For a constant mass flow and inlet temperature, such as in this example, will not result in deviation between energy storage (only in the storage profile). However, the CV- system is dependent on highly dynamic behavior, which could result in deviation of energy storage. Additionally, the TDV in the CV-system is dependent on the inlet temperature to the storage tank, thus a higher degree of stratification will result in a more realistic representation.

$$T_{n,t} = T_{n,t-1} + \left[\frac{\dot{m}c_p(T_{n-1,t-1} - T_{n,t-1})}{V_n \rho c_p} - \frac{U(A_{top} + A_{bot} + A_{edg})_n (T_{n,t-1} - T_a)}{V_n \rho c_p}\right] dt \qquad \text{C.13}$$

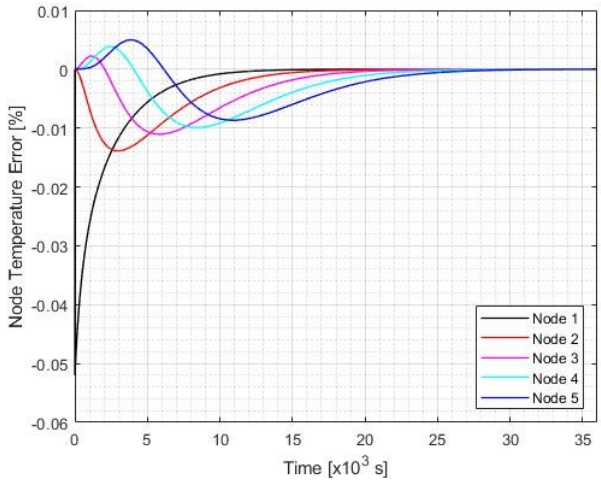

Figure C.5 — Error in outlet temperature of simulation compared to theoretical model, using $T_{in,st}$ = 60 °C, ṁ = 300 kg hr^{-1} and $T_{n,0}$ = 20 °C.

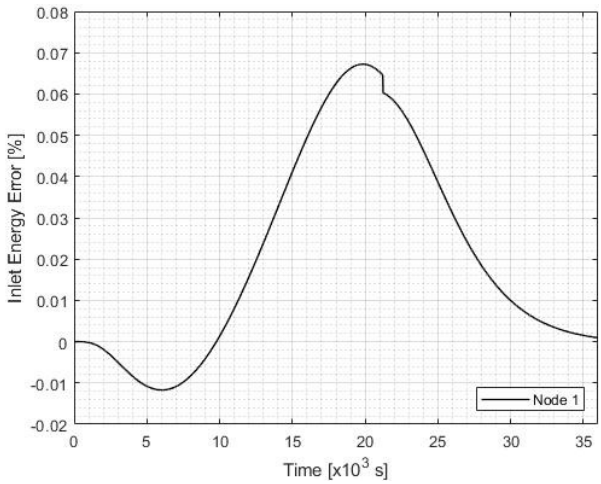

Figure C.6 — Error in inlet energy of simulation compared to theoretical model, using $T_{in,st}$ = 60 °C, ṁ = 300 kg hr^{-1} and $T_{n,0}$ = 20 °C

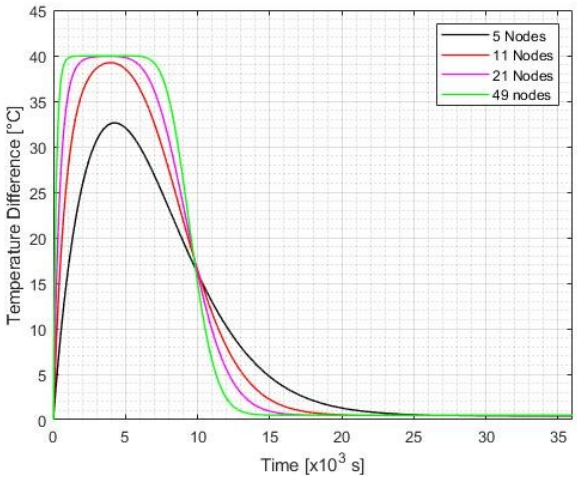

Figure C.7 — Temperature difference between top and bottom of storage tank for different number of nodes, using $T_{in,st}$ = 60 °C, $\dot{m}$ = 300 kg hr^{-1} and $T_{n,0}$ = 20 °C.

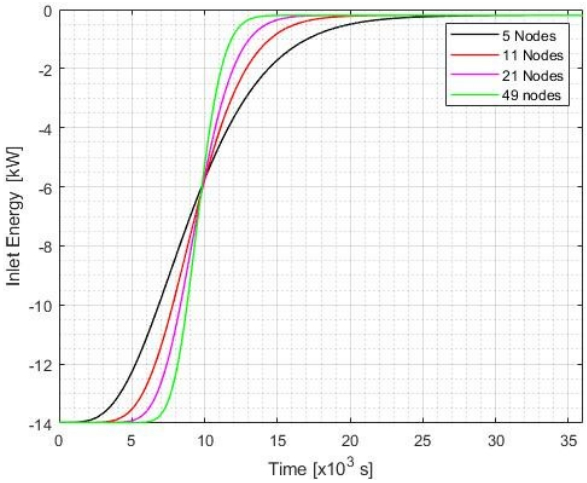

Figure C.8 — Inlet energy profile for different number of nodes, using $T_{in,st}$ = 60 °C, $\dot{m}$ = 300 kg hr^{-1} and $T_{n,0}$ = 20 °C.